UNIVERSITY OF MINNESOTA

CENTER FOR TRANSPORTATION STUDIES

RESEARCH REPORT

TH 241 Column-Supported Embankment

Gregory Wachman
Joseph F. Labuz

CTS # 08-11

Technical Report Documentation Page

1. Report No.	2.	3. Recipients Accession No.	
CTS 08-11			
4. Title and Subtitle		5. Report Date	
TH 241 Column-Supported Embankment		June 2008	
		6.	
7. Author(s)		8. Performing Organization Report No.	
Gregory Wachman, Joseph F. Labuz			
9. Performing Organization Name and Address		10. Project/Task/Work Unit No.	
Department of Civil Engineering University of Minnesota 500 Pillsbury Dr. SE Minneapolis, Minnesota 55455		CTS project # 2006054	
		11. Contract (C) or Grant (G) No.	
		(c) 81655 (wo) 226	
12. Sponsoring Organization Name and Address		13. Type of Report and Period Covered	
Minnesota Department of Transportation 395 John Ireland Boulevard Mail Stop 330 St. Paul, Minnesota 55155		Final Report	
		14. Sponsoring Agency Code	
15. Supplementary Notes			
http://www.cts.umn.edu/Publications/ResearchReports/			

16. Abstract (Limit: 200 words)

A pile-supported embankment constructed on TH 241 near St. Michael, MN was instrumented with 48 sensors, including strain gages on the piles and on the geogrid, as well as earth pressure cells and settlement systems near the base of the embankment. Pile supported embankments are relatively novel structures employed largely at bridge approaches and highway expansions where soft soils would otherwise lead to unacceptably large differential settlements. The structure typically consists of a number of capped piles, well-compacted gravel, and one or more layers of geogrid reinforcement above the piles. Analyses of the data suggest that the redistribution of the embankment load to the piles occurs within and above the so-called load transfer platform, a 1 m layer of geogrid-reinforced gravel. Arching seemed to take place within the embankment, such that the stress at the top of the platform was concentrated above the piles.

17. Document Analysis/Descriptors	18. Availability Statement		
pile-supported embankment, load transfer platform, earth pressure, soil arching, field instrumentation	No restrictions. Document available from: National Technical Information Services, Springfield, Virginia 22161		
19. Security Class (this report)	20. Security Class (this page)	21. No. of Pages	22. Price
Unclassified	Unclassified	111	

TH 241 Column-Supported Embankment

Final Report

Prepared by:

Gregory Wachman
Joseph F. Labuz

Department of Civil Engineering
University of Minnesota

June 2008

Prepared for:

Minnesota Department of Transportation
Foundations Group
1400 Gervais Avenue
Maplewood, Minnesota 55109

Acknowledgements

Partial support was provided by the Minnesota Department of Transportation. Special thanks are extended to the Technical Advisory Panel, especially Richard Lamb, Derrick Dasenbrock, Gary Person, and Glenn Engstrom. Prof. Luigi Biolzi, from the Politecnico di Milano, performed the finite element analysis. This report represents the results of research conducted by the authors and does not necessarily represent the views or policies of the Minnesota Department of Transportation and/or the Center for Transportation Studies.

Table of Contents

List of Tables

List of Figures

Executive Summary

A pile-supported embankment constructed on TH 241 near St. Michael, MN, was instrumented with 48 sensors, including strain gages on the piles and on the geogrid, as well as earth pressure cells and settlement systems near the base of the embankment. Pile supported embankments are novel structures employed largely at bridge approaches and highway expansions where soft soils would otherwise lead to unacceptably large differential settlements. The structure typically consists of a number of capped piles, well-compacted gravel, and one or more layers of geogrid reinforcement above the piles. Analyses of the data suggest that the redistribution of the embankment load to the piles occurs within and above the so-called load transfer platform, a 1 m layer of geogrid-reinforced gravel. Arching seemed to take place within the embankment, such that the stress at the top of the platform was concentrated above the piles.

Chapter 1
Introduction

1.1 Motivation

Increasing urban and suburban development has led to a rise in the construction and expansion of highways and other structures on land that was previously considered unsuitable. Soils in these areas are often comprised of thick layers of soft, organic clays and peats. Large loads due to the construction of embankments or other structures can cause substantial and often unacceptable settlement in these soils.

A number of techniques have been developed in order to deal with anticipated settlements in soft soils below embankments. One method is to apply a large vertical load in the form of a soil surcharge over the soft soil prior to construction, increasing pore water pressure, and therefore speeding up drainage and consolidation. Settlement due to the surcharge is monitored over time, and construction proceeds once it is judged that nearly all settlement has taken place. Prefabricated vertical wick drains can be installed to decrease the distance water must travel through the soil in order for drainage to occur, quickening the consolidation process. Furthermore, the addition of one or more layers of geosynthetic reinforcement at the base of the embankment can improve the stability of the embankment.

Another option is to build the embankment on a grid of piles or columns that are driven or constructed to a more competent underlying layer, such as bedrock. Assuming the embankment load is transferred almost entirely to the piles, and thus the competent layer, the problems associated with the soft soils can be avoided. The mechanism that allows that load transfer is soil arching. It has been found that the addition of one or more geogrid layers at the base of the embankment, just above the piles, facilitates the transfer of the embankment load to the piles, and allows for greater pile spacing.

Lack of a standard design has led to the development of many design theories and methods. Additionally, the interaction between the embankment, geogrid, and piles/columns is complex, and much remains unknown about the precise mechanism by which the load transfer occurs. This has motivated investigations of these structures, including analytical, numerical, and experimental, as well as field instrumentation studies.

1.2 Overview

The objective of this research was to evaluate the performance of a pile supported embankment utilizing a load transfer platform (LTP), which consists of several layers of geogrid separated by layers of highly frictional fill. Of particular interest were the following quantities:

1. The portion of embankment load carried by the piles
2. The earth pressure between the piles at the base of the LTP

3. Settlement between the piles at the base of the LTP
4. Strain in the upper-most and lower-most geogrid layers within the LTP
5. Earth pressure at the top of the LTP, directly above and between piles
6. Settlement at the top of the LTP, directly above and between piles

In order to investigate those quantities, a field monitoring program was designed and carried out at a site near St. Michael, MN on Trunk Highway (TH) 241, consisting of 48 sensors including strain gages, earth pressure cells, and settlement systems.

Chapter 2
Background

2.1 Case histories

Pile-supported embankments fist came to be used extensively in Scandinavia in the 1960s. Rathmayer (1975) reported on three test embankments constructed in Finland, which were instrumented with earth pressure cells and load cells in order to investigate (1) transfer of the embankment load to the piles, (2) vertical stress distribution over a pile cap, and (3) the effect of pile cap shape on loading over the pile cap. It is notable that the paper mentions nothing about geosythetic reinforcement being used above the pile caps. The earth pressure distribution above the pile cap was found to be highly non-uniform, concentrated largely on the outer ring of the cap. It was also found that 75% of the load from the tributary area was carried by the pile. Pile cap coverage, or the portion of the base of the embankment covered by piles, varied from 30% to 50%. Finally, it was concluded that circular pile caps are more efficient than rectangular caps at bearing load, registering 10% more load for the same area under identical conditions.

Reid and Buchanan (1984) detailed the use of pile-supported embankments for bridge approaches in Scotland. It was noted that in these embankments a membrane layer was placed directly above the pile caps in order to minimize settlement in the areas between pile caps and to encourage arching. The inclusion of reinforcement allowed for the use of smaller pile caps, making the formation of bending moments at the top of the piles a secondary design concern. Instrumentation at two separate sites included an array of earth pressure cells above pile caps, piezometers, inclinometer tubes, settlement profile tubes, and pile load cells. Their findings on the earth pressure distribution above the pile cap concurred with those of Rathmayer, as the maximum stress was found to occur at the pile cap edge. In this case, pile coverage was about 11% and it was found that 82% of the load from the tributary area was taken by the pile.

Fluet et al. (1986) reported on a test embankment spanning two supports that was constructed to investigate the effects of a geogrid layer placed at the base of the embankment. The foundation soil between the supports was modeled using inflatable air bags in which the pressure could be controlled. While the paper does not directly deal with the scenario of an embankment supported by a system of piles, the problem is analogous to the zone spanning two piles, and the results describing the interaction between the geogrid and arching action within the embankment fill have been cited extensively in literature focused on column-supported embankments. Specifically, the authors found that the addition of a geogrid layer at the base of the embankment promoted arching action in the above fill, whereas in the case in which no geogrid was used, no observable arching took place.

Gartung et al. (1996) reported on a railway embankment reinforced with three layers of geogrid supported by a rectangular grid of piles. Strain on geogrid was measured to be between 0.3% and 1%, with the greatest value taking place at the central location between four piles. Design strain for the grid was 3%. Settlement at the base of the embankment, as well as the vertical displacement and tilt of the pile caps, was measured with a system of 11 vertically-oriented rod

extensometers. It was found that the caps displaced around 10 mm, while maximum settlement was found to occur between the piles, and was about 50 mm.

Maddison et al. (1996) described the design and performance of an embankment supporting a new toll plaza in South Wales, UK. Vibro concrete columns were constructed in a triangular grid pattern to support a load transfer platform containing two layers of biaxial geogrid. The load transfer platform was overlain by a layer of embankment rock fill. Construction monitoring was performed utilizing a series of hydraulic pressure cells and settlement markers. Settlement between columns was found to be between 40-50 mm. Stresses directly above the columns at the top of the platform increased over the course of construction to levels consistent with the design analyses predictions, while stresses at the base of the platform were comparably small, indicating the formation of arching. Long-term monitoring of the site after the completion of the toll plaza construction was conducted with a number of surveys, which indicated no movements of the embankment after 12 months.

Stewart et al. (2004) evaluated the performance of a test embankment at the interchange between I-95 and US route 1 in Virginia. Dry deep mixing was used to produce 59 columns, which gave vertical support to a test embankment laterally supported by a geosynthetic-reinforced MSE wall on one side and a 2H:1V slope on the other. Field measurements of vertical stress directly above columns and between the columns were taken and used to calibrate a numerical analysis performed with the Finite Layer Analysis of Consolidation (FLAC) method. Lateral displacements measured using vertical inclinometers were then compared to the calibrated FLAC model.

Vega-Meyer and Shao (2005) outlined a case history of a column-supported embankment supported laterally by MSE walls in Colón City of the Republic of Panama. Four layers of uniaxial geogrid alternating in transverse and longitudinal orientation with respect to the embankment were installed within the load transfer platform. A 2D numerical was first used to predict maximum total and differential settlements of the embankment design. Settlement readings, starting 132 days following construction due to sensor problems, showed similar values of displacement for sensors located between piles, both above and below the LTP, while settlement above the pile at the top of the LTP was negligible. Strain gages on the geogrid registered up to 1% strain. Vertical stress was measured above the pile cap and between piles at the base of the platform, and it was found that the stress registered between the piles was about 18% that above the pile.

Plomteux et al. (2004) described an embankment east of London, England supported by 2193 controlled modulus columns. The preliminary design was checked with several numerical analyses examining settlements, tensile stresses in the geotextile layers, and soil stability. Settlement values obtained from settlement plates and settlement pegs averaged at 10 mm, one third of the value calculated from the design analysis.

2.2 Model studies

A few authors have designed model experiments simulating column-supported embankments, either to gain an understanding for a design or to compare with numerical analyses. A few key studies are summarized here.

Hewlett and Randolph (1988) experimented with dry and moist sand in both plane strain and 3D pile grid geometries, and they used the finding as a basis for design analyses in both geometries. Soft soils were simulated with foam rubber chips, and sand layers of alternating color were placed horizontally such that displacements in the embankment could be measured through a glass wall. Pile spacing was varied and the load on the piles, represented by wooden blocks, was measured with load cells. Displacement measurements indicated that shear displacement was most significant in fan-shape areas radiating out from the pile cap, and that settlement was nearly uniform both well above the piles and between the piles at the base of the sand layer. This last finding was taken to suggest that the vertical stress at the base of the sand layer is uniform. Some tests were done with moist soils in which the box was filled with soil and then lifted up, releasing some sand between piles and revealing the bottom of the region of arched soil. This shape was found to be approximately hemispherical.

The authors used their experimental findings to guide them in developing an analysis to determine the stresses throughout the embankment for both plane strain and 3D cases. The main results are expressions for pile support efficacy, or the proportion of the embankment load carried by piles. These are explained in more detail in section 2.5.

Low et al. (1994) performed model tests and an analysis of a pile-supported embankment with geotextile reinforcement, but with the addition of cap beams spanning the piles in the direction perpendicular to the longitudinal axis of the embankment. The cap beam was proposed as an additional means of reducing differential settlements at the top of the embankment. Experiments were conducted both with and without reinforcement. Foundation soil was modeled with soft rubber foam, while dry sand was used for fill material. The pile-cap beam combination was modeled as a plane structure with wooden blocks. Load cells measured the total load between blocks at the base of the tank, as well as the load on sections of the cap beams. Design parameters of efficacy, competency, and stress reduction ratio were calculated given the embankment height and beam spacing. Competency was defined as “the ratio of the load on the cap beam to the weight of a column of soil having the same width as the cap beam”, while the stress-reduction ratio was defined as the ratio of the actual average vertical stress on the soft ground to the anticipated vertical stress due to the embankment weight if uniformly distributed. Mathematical definitions of the design parameters can be found in section 2.5. The main findings were:

1. the efficacy calculated in the reinforced case was 1.3-1.5 times that of the unreinforced case, and
2. the vertical stress on the soft ground decreased with smaller pile spacing.

The authors carried out a plane strain analysis of the case with no geosynthetic reinforcement similar to that of Hewlett and Randolph (1988), but with several refinements. Experimental

values for efficacy compared well with the calculated values. The reinforced case was also analyzed, and stress reduction ratios for the experimental and theoretical cases were compared for different values of pile spacing. A favorable comparison was obtained for wider spacing, while results for smaller spacing compared poorly. The analyses also revealed that the location of critical stability is at the crown of the arch, rather than immediately above the cap beams.

A model study by Van Eekelen et al. (2003) used saturated foam cushions for the foundation material in order to represent possible effects of the consolidation of moist soft soils. The experiments were apparently designed so that arching would take place in an incomplete fashion, and significant differential settlements would be observed at the top of the model embankment. Reinforcement was not considered. Earth pressure cells measured vertical stress at ten locations throughout the test setup, both between and directly above the piles, and deformation was observed and measured through glass walls. The measured vertical stress above piles was compared to several 2D design predictions, including a modified Rogbeck/Carlsson method (also called the Swedish method) and the McKelvey method. It was found that measurements best matched stresses predicted by Rogbeck/Carlsson. A brief description of the various designs is given in section 2.4.

2.3 Numerical studies

Jones et al. (1990) were among the first to quantitatively consider the effects of geotextile reinforcement. They first presented a simplified design analysis based on Marston's formula for positive projecting subsurface conduits. Marston's formula is used to predict the proportion of the embankment load carried by the piles. The remaining embankment load is distributed uniformly across a single layer of reinforcement and is used along with the reinforcement strain (specified as part of the design) to calculate the tensile load in the reinforcement. This simplified analysis was used as the basis for BS 8006, the British Standard design method.

A finite element study in plane strain was carried out in order to obtain a more accurate prediction of tensile forces in the reinforcement. Parameters that were studied were material properties (friction, cohesion, unit weight, Poisson's ratio and modular stiffness) associated with the fill as well as the foundation material, embankment height, pile spacing and pile cap diameter (combined to provide roughly 10% areal coverage by pile caps). Settlement and minimum embankment height for stability were calculated for both the pile-supported, reinforced case and the unsupported, unreinforced case. It was concluded from the finite element study that support from the subsoil, which is not considered in the simplified analysis, can have a significant impact on the tensile load developed in the reinforcement. This confirmed the conservative nature of the simplified analysis.

Han and Gabr (2002) used FLAC to analyze the case of a square pile layout, studying total and differential settlements, vertical stresses above and below the geosynthetic, soil arching between piles, stress concentration above piles, and tension in a geosynthetic layer. A nonlinear hyperbolic elastic model was employed for the soil. Results of the cases of reinforced and unreinforced embankments showed the effectiveness of geogrid in minimizing total and

differential settlements. It was found that maximum tension in the geosynthetic occurred at the edge of the pile cap, though the same result showed no tension at the midpoint between piles.

2.4 Calculation of tributary load

Pile loads determined with strain measurements can be compared to the tributary load W_{tr}, the weight of the material in the pile's tributary area A_{tr}, as discussed in Chapter 2. The tributary area is the geometric region "belonging" to each pile within a uniform pile grid. In a triangular grid the tributary area is hexagonal in shape (Fig 2.1). The weight is calculated with the following equation from Chapter 2:

$$\begin{aligned} W_{tr} &= A_{tr}\left(\gamma H + w_s\right) \\ &= \frac{\sqrt{3}}{2}s^2\left(\gamma H + w_s\right) \end{aligned} \tag{2.1}$$

where s is the center-to-center pile spacing, γ is the unit weight of the embankment fill, H is the embankment height, and w_s is a possible surcharge above the embankment fill.

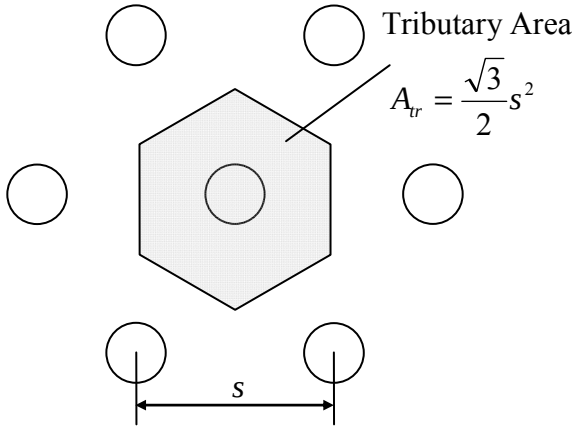

Figure 2.1. Plan view diagram showing the tributary area for a triangular pile grid.

2.5 Design parameters

Various authors have introduced parameters for describing the performance of pile-supported embankments. Efficacy E_f, which was originally introduced by Hewlett and Randolph (1988), is the ratio of the measured pile load (as determined from strain gages or other techniques) to the tributary weight:

$$E_f = \frac{F_{tot}}{W_{tr}} \tag{2.1}$$

In theory, the upper limit of E_f is one, assuming the maximum load available to the pile is W_{tr}. The lower the efficacy, the less effective the pile-supported embankment is at transferring the embankment load to the piles.

Competency C_m, as described first by Low et al. (1994), is the ratio of the measured pile load and the weight of fill directly above the pile cap:

$$C_m = \frac{F_{tot}}{a\gamma H} \tag{2.2}$$

where a is the pile cap area. It is a measure of load concentration at the pile, comparing the actual load to what the load would be under uniform vertical earth pressure. Assuming the upper limit of F_{tot} is W_{tr} (E_f = 1), the theoretical upper limit of competency would then be

$$\begin{aligned} (C_m)_{\max} &= \frac{A_{tr}\gamma H}{a\gamma H} \\ &= \frac{A_{tr}}{a} \end{aligned} \tag{2.3}$$

the ratio of the tributary area to the pile cap area.

The final measure of performance is the stress reduction ratio S_{3D}, which is probably the most widely used parameter in the literature. The stress reduction ratio is defined as

$$S_{3D} = \frac{S_L}{(A_{tr} - a)\gamma H} \tag{2.4}$$

where S_L is the total vertical load at the base of the embankment between piles. If it is assumed that vertical stress s_L represents the average vertical stress of the total load S_L over the geogrid, S_{3D} simplifies to

$$S_{3D} = \frac{s_L}{\gamma H} \tag{2.5}$$

The stress reduction ratio is a measure of the actual load between piles and the theoretical load under the vertical stress due to the embankment fill. It is frequently used for the design of the geogrid reinforcement at the base of the embankment, since s_L represents the vertical stress on the geogrid layer. Design methods vary in the assumptions used to calculate s_L, as is discussed in

section 2.6. Therefore there is no single theoretical value of S_{3D}. Rather, it depends on the assumption made in the design that determines the volume of loose soil not included in the arching action.

2.6 Summary of design methods

Although several methods of designing column-supported embankments have been developed and refined over the years, there is still no single standard method. The assumptions regarding soil arching and behavior of the reinforcement vary. The Collin Method was used to design the pile-supported embankment instrumented for this study, and as such will be described in detail. Other methods will also be summarized, highlighting differing assumptions among methods.

2.6.1 The Collin method

The Collin method is a refinement of the adapted Guido method, which is based on the work of Guido et al. (1987). The authors of that study conducted plate loading tests on geogrid-reinforced soil masses in order to study the bearing capacity. Tests showed that unreinforced sand exhibited a local shear failure mode, in which the shear surface extends to the surface such that some heaving is observed. Following failure, the load remained roughly constant as displacement increased. On the other hand, reinforced sand seemed to follow a punch failure mode, in which no surface heaving is observed and the failure surface extends directly below the edge of the plate, indicated by a visible deflection of the geogrid at that location. Furthermore, the investigation found that the optimal number of geogrid layers for increasing bearing capacity was three, with additional layers providing little or no benefit.

Bell et al. (1994) proposed that one result of the work of Guido et al. is that in a reinforced soil mass the angle of load spread above a pile can be conservatively estimated to be 45 degrees as long as the angle of internal friction of the material is at least that value.

Jenner et al. (1998) applied the work of Guido et al. and Bell et al. to the inverted problem of a soil mass resting above a pile. The possible effects of a reversed sense of gravity on the problem are not considered, as pointed out by Russell and Pierpoint (1997). The authors cite several case histories in which this "enhanced arching" design approach was used successfully, including Maddison et al. (1996) and Topolnicki (1996).

The Collin Method follows in concept the approach described by Jenner et al. Several layers (typically three) of vertically spaced geogrid are placed within well-compacted select fill, forming what is called a load transfer platform (LTP). The primary purpose of the geogrid is to give lateral confinement to the fill, making the transfer of the embankment load to the piles more efficient. Supporting the loose soil below the arched region is the secondary function of the geogrid. The design assumes the following (Collin 2004):

- Soil arching occurs above a region defined by an angle of 45 degrees from the pile cap edge.

- The loose soil to be supported by the geogrid forms a pyramid-shaped region between each group of three piles.
- The entire embankment load above the LTP is transferred to the piles.

The basic guidelines of the design are as follows:

- The thickness of the LTP is equal to or greater than the clear span between piles, or the shortest distance between the edges of adjacent pile caps.
- A minimum of three layers of geogrid is used to form the LTP.
- The initial strain in the geogrid should be limited to 5%.

The following steps outline the Collin method (Collin 2004), which was implemented in the design of the embankment. Quantities used in this project are provided in brackets.

Design of pile grid

1) The pile grid shape, center to center pile spacing s, and the pile cap shape and size (diameter d for circular caps) are estimated based on previous experience. In general, capacity of the pile and height of the embankment will limit the pile spacing [equilateral triangular grid with s = 7 ft (2.13 m), d = 2 ft (0.61 m)].
2) The piles are assumed to carry the entire embankment load. Assuming a uniform distribution of the embankment load over the pile grid, each pile supports a tributary load W_{tr}. As discussed in section 2.4, W_{tr} for triangular spacing is

$$W_{tr} = \frac{\sqrt{3}}{2} s^2 \left(\gamma H + w_s\right) \qquad (2.6)$$

An appropriate pile type is chosen based on the design load, and spacing can be reduced if the pile load is excessive.

Design of load transfer platform

The platform design is considered separately from the pile design, although it depends on the pile grid shape and spacing, as well as the shape and size of the pile caps. The main component of the LTP design is calculating the tensile load in the geogrid.

1. It is assumed that the arched region within the LTP is located above a boundary described by α = 45 degrees from horizontal at the edge of the pile cap. A simplified 2D illustration of this is shown in Fig 2.2. It is then assumed that the loose (non-arching) soil forms a three or four-sided pyramid, depending on the pile layout. Fig 2.2 shows in plan view a three-sided pyramid, as is the case in the present project.

   The height h_a of the apex of the pyramid described in the previous step, is calculated, based on the pile spacing, as follows:

$$h_a = \frac{(s-d)}{2} \tan \alpha \qquad (2.7)$$

   where s is the center-to-center spacing of the piles and d is the pile cap diameter. The LTP thickness h should be greater than or equal to h_a [h_a = 2.5 ft (0.76 m), h = 3 ft (0.91 m)].

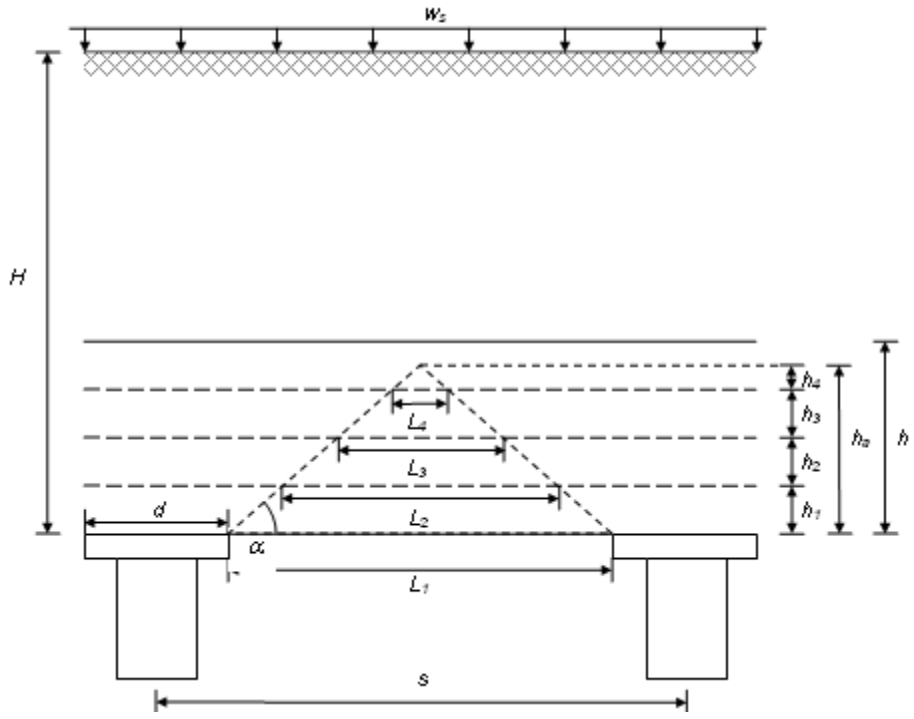

Figure 2.2. A section view of the 2D problem illustration the various quantities involved in the design calculations.

2. The spacing of the geogrid layers is specified. (Note: in the design considerations Collin states that the minimum spacing should be 8 in. (20 cm), but this design does not follow this specification) [h_1 = 6 in.(15 cm), h_2 = 9 in.(23 cm), h_3 = 12 in. (30 cm), h_4 = 3 in. (8 cm)]
3. The strength of the geogrid is chosen as the lower of two values: i) the allowable strength given the safety factor, and ii) the allowable creep limited strength at maximum strain (5%)
4. The uniform vertical stress w_n on geogrid layer n within the pyramid is calculated as the weight of fill material between layer n and the layer $n+1$ directly above it divided by the area of layer n:

$$w_n = \gamma h_n \frac{L_n^2 + L_{n+1}^2}{L_n^2} \tag{2.8}$$

where L_n is the length of the side of the equilateral triangle formed by the intersection of the pyramid and geogrid layer n (Fig. 2.3).

5. Tensile load per unit length T_n is calculated for geogrid layer n based on 2D tension membrane theory:

$$T_n = w_n \frac{D_n}{2} \Omega \tag{2.9}$$

where Ω is a dimensionless factor determined from strain level [Ω = 0.97 for 5% strain], and D_n is design span (Fig. 2.3), calculated for triangular spacing as

$$D_n = L_n \sin(60°) = \frac{\sqrt{3}}{2} L_n \tag{2.10}$$

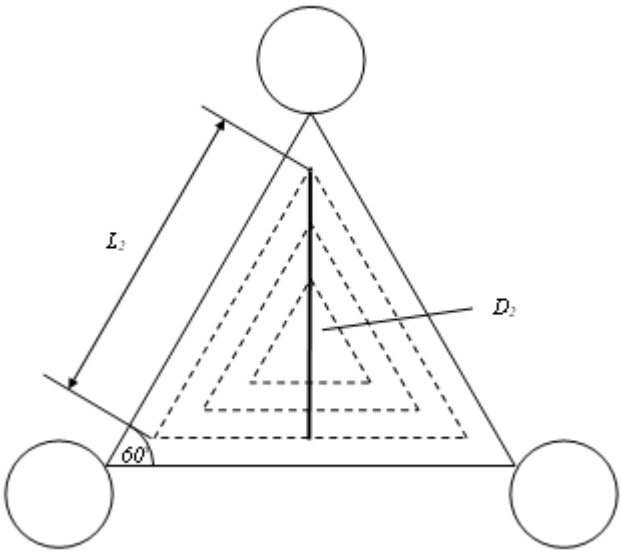

Figure 2.3. A plan view of the pyramid used for the LTP design calculations. Dotted lines represent where the geogrid layers intersect the pyramid.

Comments on design

It was noted in the review of the literature that there are a few inconsistencies in the determination of the volume used to calculate the load on the geogrid. In particular, the assumed shape of a pyramid is not consistent with the assumption that arching occurs at a given angle from the horizontal at the pile cap edge. Furthermore, if a pyramid is used to approximate the true shape, the length chosen for the base of the pyramid should correspond with the pile spacing.

The precise shape of the volume of soil that the geogrid must support in triangular spacing cannot be extrapolated from a 2D section view diagram such as Fig. 2.2, which strictly represents a 2D problem. To determine this shape, one must start with the assumption regarding α, the angle at which arching occurs. In the case of a single circular pile cap α must be rotated around the edge of each cap, creating a semi-conical region above the pile cap, which is assumed to be supported by the pile. For a triangular group of piles, the semi-conical surfaces between the piles for each pile intersect within the triangular area, and the shape below the surfaces is the region of loose material. The shape would have six sides apart from the base; three sides are simply vertically-oriented triangles between adjacent pile caps, while the other three are sections of the semi-conical surfaces extending from the pile caps. Figure 2.4 shows a computer-generated image of the shape, which is more complex than a pyramid, and as such may be impractical for use in design calculations.

For design purposes, it may be appropriate to approximate the shape of the loose material with a pyramid. However, care must be taken in determining the size of the pyramid. In Collin's design procedure, the length of the pyramid base edges was calculated as *s*-*d*, the span between two pile caps. In the 2D problem this is correct for determining the base width of the triangular prism (Fig. 2.2), but in the 3D case that value underestimates the area of the pyramid base, as seen in Fig 2.5. More importantly, due the nature of the shape of the pyramid, this underestimation is much more significant in the calculation of the volume of the pyramid. For example, a pyramid with a base edge length of 7 ft results in a volume over 270% that of a pyramid with base edge length of 5 ft.

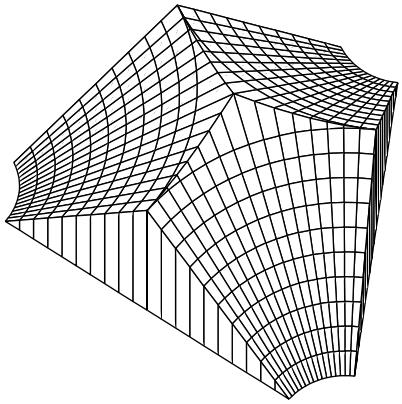

Figure 2.4. A perspective view of the shape described above. The quantities used to generate the image are consistent with the TH241 LTP (*s*=7 ft, *d*=2 ft, α=45°).

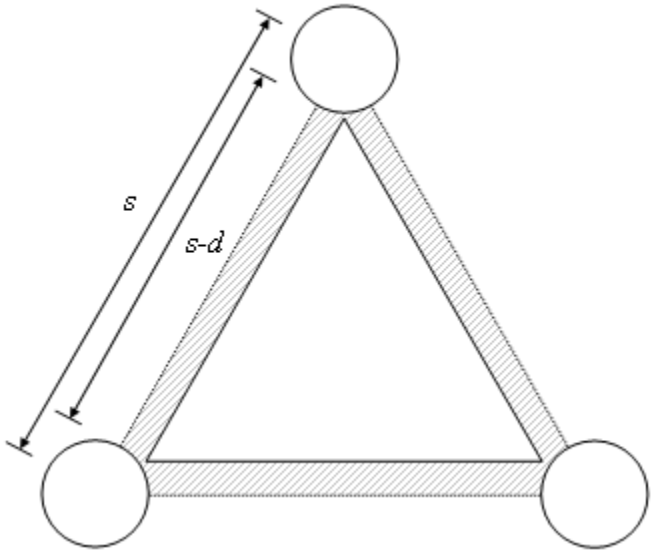

Figure 2.5. The shaded area represents area missing from the triangle with edge length *s*-*d*.

2.6.2 Other methods

Several other pile-supported embankment design methods exist. This section describes the basic features of these designs, highlighting ways in which they are different from the Collin Method. More detailed comparisons can be found in Collin (2004), Stewart and Filz (2005), Love and Milligan (2003), and Russell and Pierpoint (1997).

One convenient way to compare the various design theories is with the stress reduction ratio (S_{3D}), introduced in section 2.5. Reviewing the definition, S_{3D} is a ratio of the average vertical stress on the reinforcement between the piles s_L to the average vertical stress at the base of the embankment ($\sigma_v = \gamma H$):

$$S_{3D} = \frac{s_L}{\gamma H} \tag{2.11}$$

The designs differ, then, in the way that s_L is calculated.

The stress reduction ratios found in the literature all correspond with square pile spacing s with square pile caps of width d. It should be expected that S_{3D} is different for triangular spacing, as different pile grid geometries affect the geometry of the load transfer. However, the formulas that follow provide a means of comparison without re-deriving the expressions for a different geometry.

Expressions have also been derived by Russell and Pierpoint (1997) for the vertical load per unit length on the geogrid W_T and the corresponding tensile load per unit length in the geogrid in terms of S_{3D} .

$$W_T = \frac{S_{3D}\gamma H\left(s^2 - d^2\right)}{2\left(s - d\right)} \tag{2.12}$$

$$T_{RP} = \frac{S_{3D}\gamma H\left(s^2 - d^2\right)}{4d}\sqrt{1 + \frac{1}{6\varepsilon}} \tag{2.13}$$

where ε is the reinforcement strain. Jones et al. (1990) recommend that a design upper limit of 5-6% be placed on ε.

British Standard BS 8006

The BS8006 suggests that the pile spacing be selected on the basis of the following relation:

$$H \geq 1.4\left(s - d\right) \tag{2.14}$$

The calculation of the vertical load on the geosynthetic is derived from arching analyses related to buried conduits, performed by Marston and Anderson (1913). The expression for S_{3D} is adapted from Russell and Pierpoint (1997).

$$S_{3D} = \frac{2.8s}{\left(s + d\right)^2 H}\left[s^2 - a^2\left(\frac{s_L}{\gamma H}\right)\right] \tag{2.15}$$

$$\frac{p_c}{\gamma H} = \left(C_c \frac{d}{H}\right)^2 \tag{2.16}$$

and C_c is an arching coefficient depending on the type of pile (Stewart and Filz (2005)):

$C_c = 1.95\frac{H}{d} - 0.18$ for end-bearing piles driven to an incompressible stratum

$C_c = 1.70\frac{H}{d} - 0.12$ for steel or concrete friction piles, or timber piles

$C_c = 1.50\frac{H}{d} - 0.07$ for stone columns, lime columns, and sand compaction columns

Hewlett and Randolph

As described in section 2.2, Hewlett and Randolph (1988) carried out a limit equilibrium analysis of vaulted arches guided by model tests. The main difference between the Hewlett and Randolph method and the Collin method is the theoretical and experimental bases used to develop them. The Hewlett and Randolph method has a strong theoretical foundation, while the work of Guido et al. was empirical. Another difference is that while Collin assumes that arching occurs at a constant angle, Hewlett and Randolph assume a hemispherical vaulted arch shape.

Russell and Pierpoint (1997) organized the results of Hewlett and Randolph into expressions for S_{3D}. They indicated there were two possible critical locations, at the top of the arch crown for low values of *H/s* and at the pile cap for high values of *H/s*. The greater of the two values for S_{3D} should be used in the design.

$$S_{3D} = \left(1 - \frac{d}{s}\right)^{2(K_p - 1)} \left(1 - \frac{s}{\sqrt{2}H}\frac{2(K_p - 1)}{(2K_p - 3)}\right) + \frac{(s-d)}{\sqrt{2}H}\frac{2(K_p - 1)}{(3K_p - 1)} \text{ (At crown)} \qquad (2.17)$$

$$S_{3D} = \left\{\frac{2K_p}{K_p + 1}\left[\left(1 - \frac{d}{s}\right)^{1-K_p} - \left(1 - \frac{d}{s}\right)\left(1 + \frac{d}{s}K_p\right)\right] + \left(1 - \frac{d^2}{s^2}\right)\right\}^{-1} \text{ (At pile cap)} \qquad (2.18)$$

where K_p is the passive earth pressure coefficient:

$$K_p = \frac{1 + \sin\phi'}{1 - \sin\phi'} \qquad (2.19)$$

Swedish method

The Swedish method, also known as the Carlsson method, is similar to the Collin method in that it assumes that arching at a constant angle α from the pile cap creates a wedge of material that must be supported by the geosynthetic reinforcement. The difference between the two methods is the assumed value of α, which is 75 degrees for the Swedish method. The lower value of 45 degrees used by Collin is a result of assuming that the LTP enhances arching. Stewart and Filz (2005) derived the expression for S_{3D}:

$$S_{3D} = \frac{(2s + d)(s - d)}{6(s + d)H\tan 15^\circ} \qquad (2.20)$$

Chapter 3
Field Instrumentation

3.1 Site location

The site is located on Trunk Highway (TH) 241 near St. Michael, Minnesota, about 2000 ft (610 m) southwest of I-94/TH 241 interchange (Fig. 3.1). The section of TH 241 for which the pile-supported embankment was chosen was located between stations 167+50 and 171+00.

The section of highway is bordered on the northwest by a small pond, and on the southeast by marshy terrain. The load transfer platform (LTP) was the foundation method selected for the westbound side of the highway, alongside the pond (Fig. 3.2). A boring taken at station 169+65.74 represents the soils on the west bank of the highway. Directly below the surface were 30 ft (9.1 m) of highly organic silt loams and peats underlain by about 20 ft (6.1 m) of silty organic soils. Below that were 12 ft (3.7 m) of loamy sand, underlain by about 35 ft (10.7 m) of gravelly sand. The boring terminated at a well-cemented sandstone 100 ft (30.5 m) below the surface.

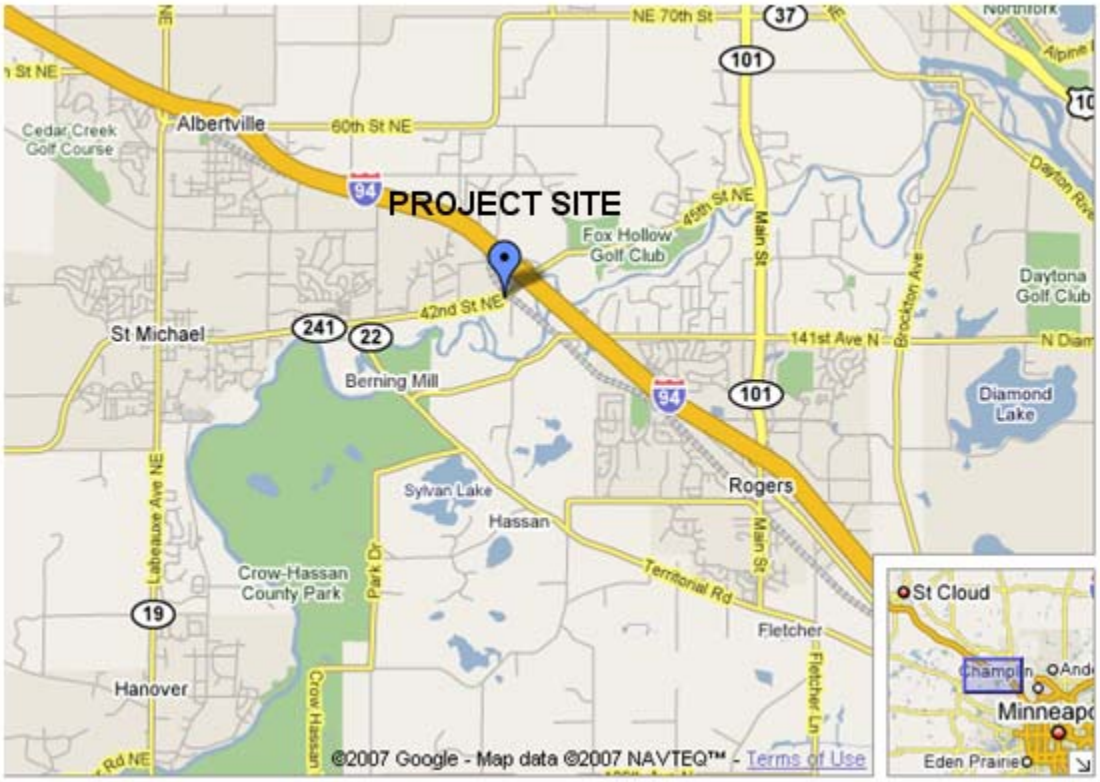

Figure 3.1. Map showing project site in relation to St. Michael, I-94 and the Twin Cities (see inset).

Figure 3.2. Plan view of site prior to highway expansion. Note the close proximity of the BNSF railroad to the pile-supported area.

3.2 Overall design

The original two-lane TH 241 was built in 1938 and overhauled in 1955/6 and 1973, with several bituminous resurfacings since the original construction. No measures were taken to deal with the deep soft soils encountered at the project site prior to the expansion. Evidence of consolidation due to the initial embankment load could be seen prior to the 2006 expansion; a dip in the road was visible across the 350 ft (107 m) section.

In recent years, increased development in the St. Michael area has led to a significant increase in residential, commercial, and industrial traffic on the highway. The area is expected to continue to grow, and it has been predicted that there will be a nearly 90% increase in traffic along TH 241 between 2005 and 2025. These factors led MnDOT to plan an expansion of the highway from two to four lanes.

Since consolidation had taken place below the original embankment, but not on the edges where the expansion would be located, differential settlement between the two regions was a significant concern. Several options were considered as potential solutions, including a land bridge and

realignment of the highway. Ultimately, however, a composite foundation system including a pile-supported section of the embankment was chosen. Soft soils on the southeast side of the expansion were found to be shallower than those on the northeast side, and it was decided by MnDOT that a more conventional shallow foundation could be constructed. The soft soils were to be partially excavated and then loaded with a surcharge to accelerate consolidation. Following the surcharge, the southeast expansion would incorporate geofoam lightweight fill in order to reduce the load on the subsoils. The geofoam also extends across the entire base of the roadway to the edge of the column supported section. Figure 3.3 shows a cross-section of the expansion according to the design.

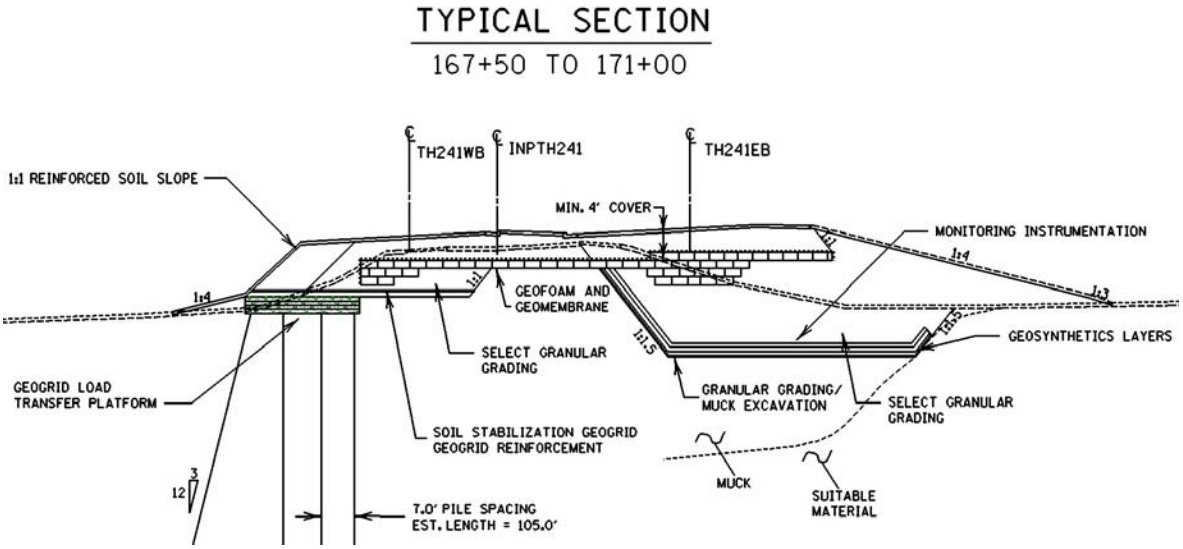

Figure 3.3. The cross-section (MnDOT) shows the various components of the foundation system selected, including the pile supported LTP and embankment (left), geofoam, and several areas with reinforcement. Surcharge was placed over the east bank of the highway near centerline TH241EB (right).

3.3 Instrument types, locations, and installation

The area of the pile-supported embankment chosen for instrumentation was in the southwest end, between stations 168+00 and 168+50 (Fig. 3.2). This region was selected because it allowed for a good distance from potential vibrations caused by the BNSF railroad that could have affected measurements, and also because the embankment was thickest in that section, providing the largest load such that measurement errors would be minimized.

In cross-section view, the instrumented area is located beneath the shoulder/highway section of the embankment, rather than beneath the reinforced slope. It was hoped that by placing the group of sensors under a region of uniform fill height, vertical stresses and strains due to the above fill could be better predicted.

Instrumentation was divided between two nearby "unit cells", each defined by a group of six piles. Unit cell 1 is comprised of the semi-hexagonal area enclosed by piles 7029, 7030, 7032, 7033, 7036, and 7037, while unit cell 2 consists of the semi-hexagonal area enclosed by piles

7043, 7044, 7046, 7047, 7050, and 7051 (Fig 3.4). In general, the separate unit cell design was chosen to achieve some redundancy of measurements. The sensor locations relative to the piles forming the unit cells were largely identical between the unit cells, allowing a comparison of measurements between the cells. Additionally, they served as a means to organize sensors with different sensing elements. For example, vibrating wire earth pressure cells were used in unit cell 1 while semiconductor-based earth pressure cells were used in unit cell 2.

A total of 48 sensors were installed throughout the LTP and on the supporting piles, including 12 EPCs, 6 settlement systems, 20 strain gages on the geogrid, 2 strain gages embedded in the piles, and 8 strain gages on the pile walls. Details about the sensor type and the method used for its installation are presented in this section according to the sensor location. The four locations of instrumentation are (1) the piles (2) the base of the LTP, (3) the top of the LTP, and (4) geogrid layers 1 and 3.

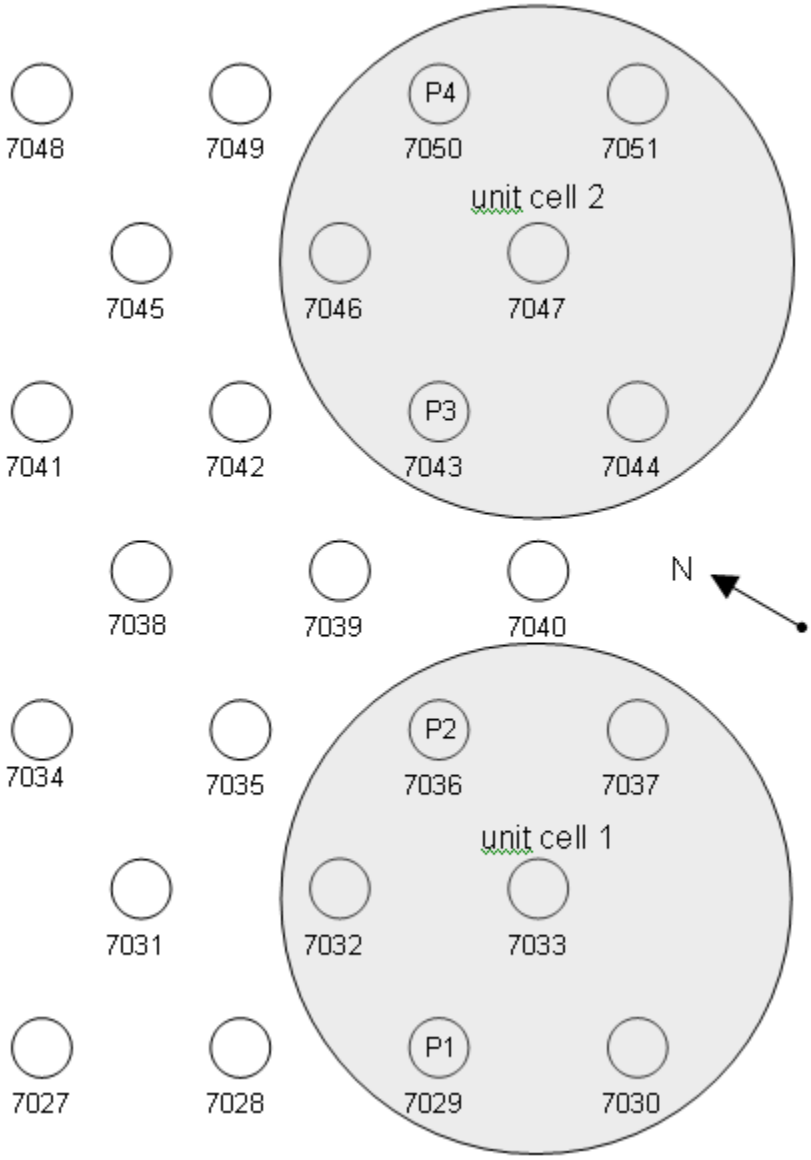

Figure 3.4. A plan view of the instrumented region of the LTP. The pile numbers, used as a reference for the instrumentation project, were originally assigned by MnDOT for the pile installation. Unit cell 1 contained mostly vibrating wire sensors, while unit cell 2 contained primarily semiconductor and resistance-based sensors. Piles labeled P1-P4 were those piles instrumented with strain gages.

3.3.1 Instrumentation on piles

A total of four piles, labeled P1-P4 (points 7029, 7036, 7043, and 7050, as shown in Fig. 3.4) were instrumented with axially-oriented strain gages. The instrumented piles lie in the same row in the pile grid, parallel to the highway centerline.

Three types of strain gages were installed in or on the piles. Concrete embedment gages (model VCE-4200) with the vibrating wire operating principle were purchased from Geokon, Inc. Figure 3.5 shows the various components of the gage. The coil housing, which is attached to the cable, is separate from the gage and is attached in the final stages of installation.

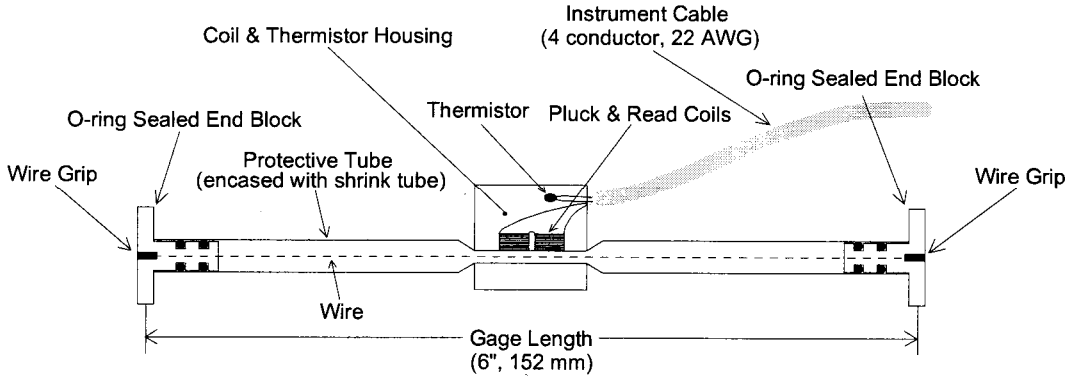

Figure 3.5. Diagram showing components of vibrating wire concrete embedment strain gage. The basic components are the wire, which is held in tension by the end blocks, and the coil housing, which is separate from the gage and attached during installation. (Geokon 2005).

Two concrete embedment strain gages (Geokon 4200A-2) were installed, one in each of two piles, P2 and P4, and were correspondingly labeled P2C and P4C. Two steel rods fixed to the pile wall held the gages in position prior to the pouring and curing of the concrete. The rods were installed horizontally through the pile, one six inches above the other, so that the gage end blocks could be secured to the rods with wires (Figures 3.6 and 3.7). First, holes corresponding with the locations of the steel rods were drilled in the pile wall. Then, the pipes were filled with concrete up to two or three feet below the top of the pile. The rods were then installed inside the pile and bolted to the pile walls. The gage was oriented in the center of the pile, leveled, and then the end blocks were tied to the rods with wires. A hole was drilled nearby to feed the cable through to the exterior, and the coil housing was attached to the gage. The remaining concrete was shoveled into the pile by hand, taking care to protect the gage.

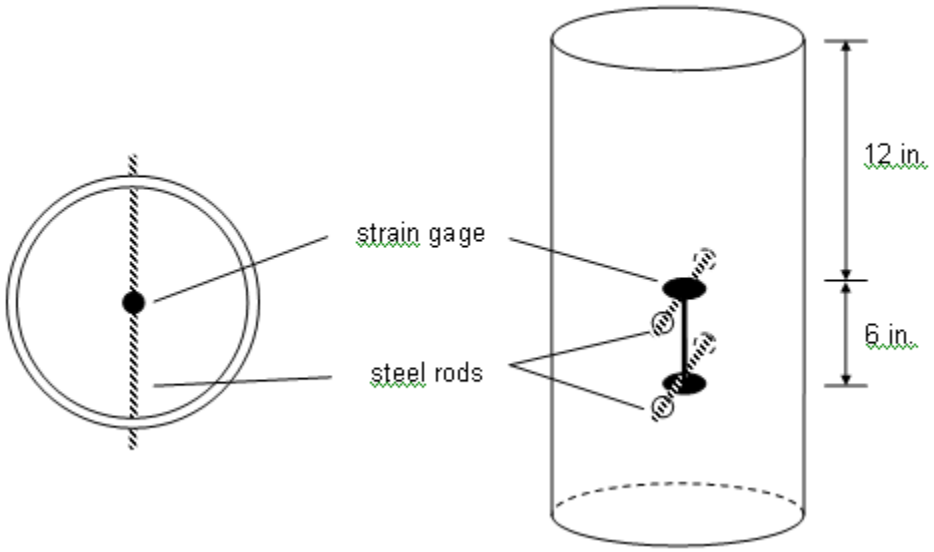

Figure 3.6. Schematic of concrete embedment gage installation, showing plan view (left) and perspective view (right).

Figure 3.7. Photograph of embedment strain gage prior to attaching the coil assembly and filling the remainder of the pile with concrete.

Piles P1-P4 were each instrumented with two strain gages on the outer pile wall, 12 in. (30.5 cm) below the top of the pile. The gage locations were diametrically opposed in a line parallel to the highway centerline. Two types of strain gages were installed on the pile walls; Piles P1 and P2 were instrumented with the Geokon 4100A-2 vibrating wire strain gage, while Piles P3 and P4 were instrumented with Micromeasurements EA-06-250BF-350 (option LE) foil (resistive) strain gages (Fig. 3.8).

Prior to the installation of the gages dirt and corrosion were removed from the surrounding area on the pile with a grinder. For the foil gages, a variety of adhesives and protectants were used. A cyanoacrylate adhesive (Micromeasurements M-200) was used to attach the gage to the pile wall. A waterproofing kit (Micromeasurements M-Coat F) provided butyl and neoprene rubber sheets, as well as a foil tape and a liquid air-drying nitrile rubber coating to seal the gage and wiring from moisture. Figure 3.9 shows the final installation.

A spot-welder was used to attach the vibrating wire gages. The mounting tabs were spot-welded as directed by the manual. Immediately afterwards a layer of cyanoacrylate adhesive was applied to the surface of the tabs for corrosion protection. The coil assembly (Fig. 3.10), which rests directly on top of the strain gage, was held in place with mounting strips that were also spot welded directly to the pile wall. A caulk designed for use with steel was applied to the edges of the assembly before and after the strips were spot-welded in order to seal the interior of the gage assembly. To protect all of the pile gages from being accidentally detached, the cable was wrapped around the pile and secured to the wall in order to provide a frictional resisting force to accidental pulling. Finally, all cables were passed through a flexible conduit that led to the data collection box.

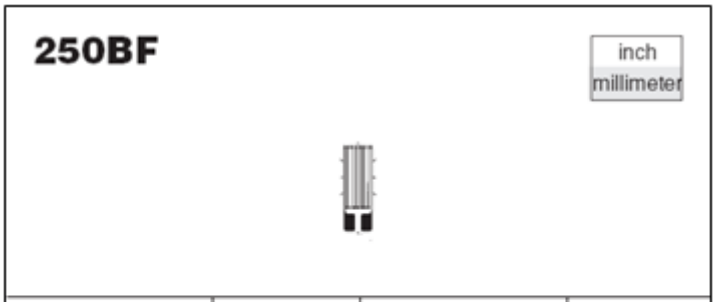

GAGE LENGTH	OVERALL LENGTH	GRID WIDTH	OVERALL WIDTH
0.250	0.375	0.125	0.125
6.35	9.53	3.18	3.18
MATRIX SIZE	0.52L x 0.22W		13.2L x 5.6W

Figure 3.8. Chart showing dimensions of 250BF series gages (http://www.vishay.com/strain-gages/gages-sensors/).

Figure 3.9. Foil gage with waterproofing on pile wall.

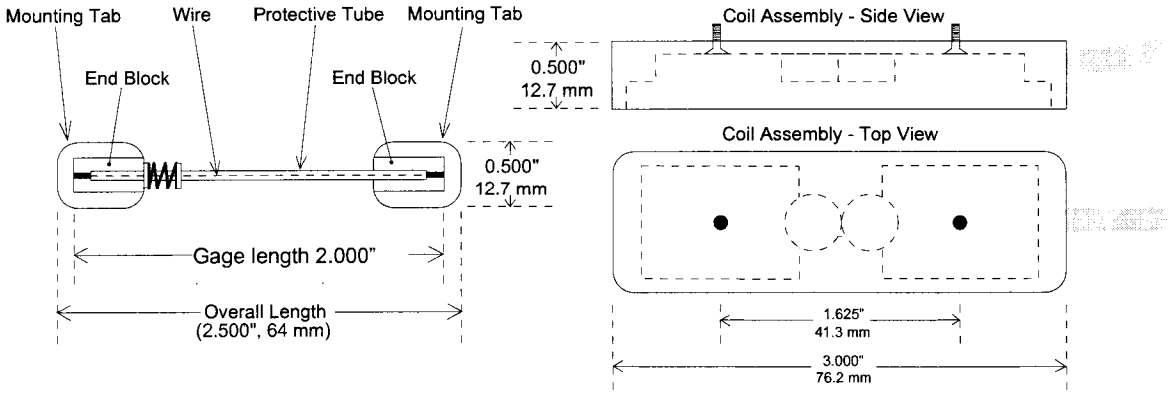

Figure 3.10. Diagram showing components of the vibrating wire spot weldable gage. The diagram on the left is the gage itself, which is a small structure housing a tensioned wire between the two end blocks that are fixed to the surface being measured. The coil assembly contains the mechanism that plucks the wire and provides the gage with physical protection. (Geokon 2005).

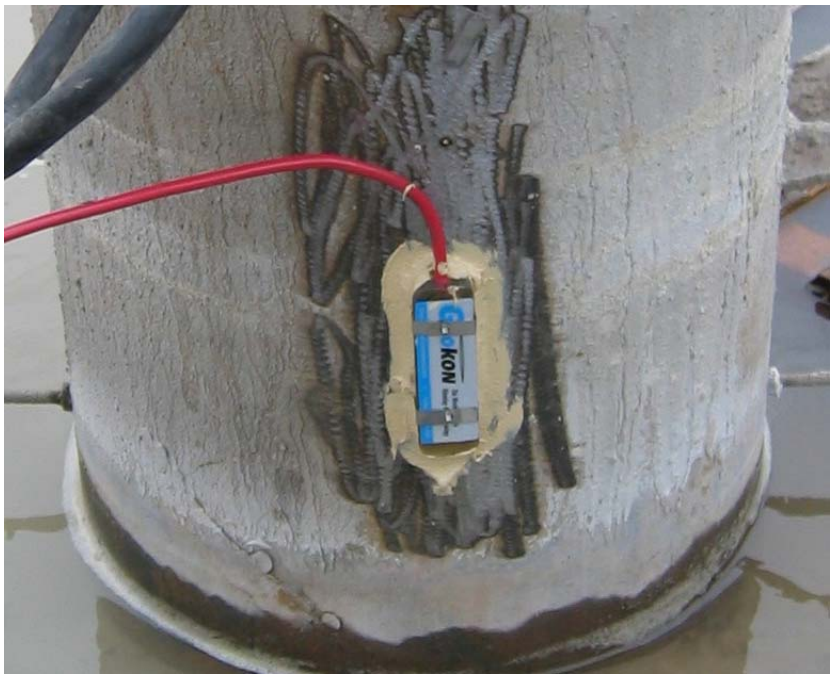

Figure 3.11. Spot-weldable vibrating wire strain gage installation on pile wall.

3.3.2 Instrumentation at the base of LTP

Twelve (12) sensors, including eight earth pressure cells and four settlement systems, were installed at the base of the LTP, or at the same elevation as the pile cap. All sensors were installed prior to the placement of the separator fabric, and as such are located beneath the LTP.

Earth pressure cells

The earth pressure cells used in this project are of the hydraulic variety. Two thin circular plates are welded together at the periphery leaving a narrow disc-shaped void that is filled with fluid and connected to a pressure transducer via a short stem (Fig. 3.12). The cell contains a relatively incompressible fluid. Pressure develops in the fluid in response to the loading on the outer surface of the plates. The pressure measured by the transducer is assumed to approximate the earth pressure at the face of the cell.

Because the stresses being measured in the soil were expected to show significant special variation, a sensor with a relatively small face was desired. Therefore, EPCs with face diameter of about 4.6 in. (11.7 cm), rather than the more common 9 in. (22.9 cm) face, were ordered from Geokon.

Additionally, because redundancy was a theme in the instrumentation plan, EPCs with two different sensing elements were used. Half of the EPCs utilized vibrating wire pressure transducers (Geokon model # 4800-1X-170KPA), while the other half contained semiconductor-based pressure transducer (Geokon model # 3500-1X-160KPA).

Although factory sensitivities were supplied with the EPCs, the sensors were calibrated in a laboratory for soil conditions. Details on the calibrations can be found in Appendices A and B.

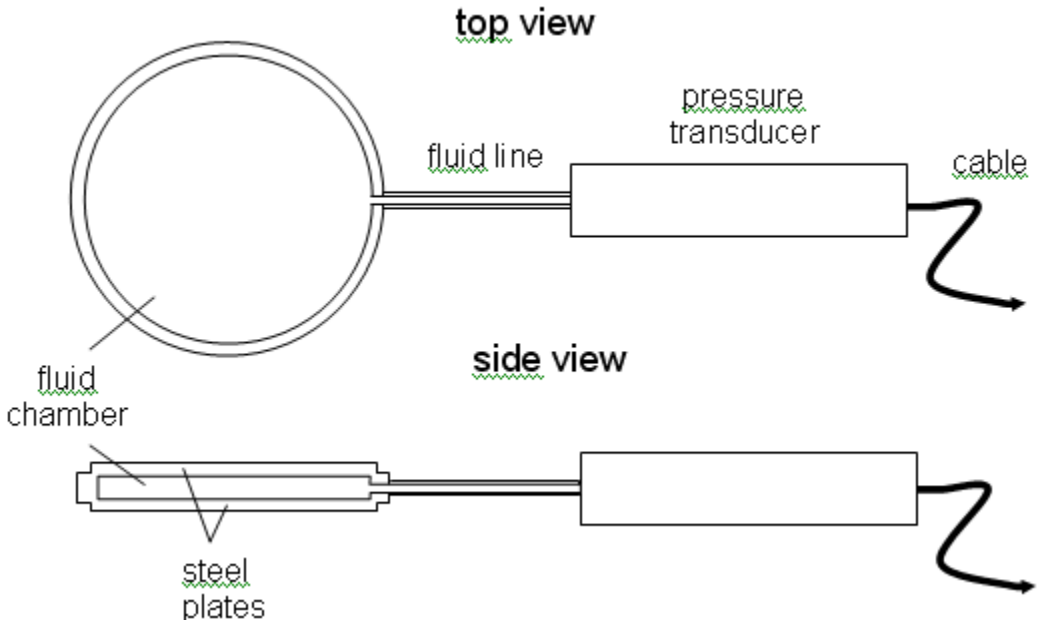

Figure 3.12. Diagram showing basic components of an earth pressure cell.

Earth pressure cells were installed in four locations in each unit cell. Two EPCs were installed in locations that can be described as the centroids of the surrounding triangular pile group. The remaining two EPCs were located near the midpoint between two adjacent piles. These locations between the piles were chosen as a check for soil arching. In the occurrence of arching, the values of stress in these locations should be significantly less than the load available from the overburden, since the load would be transferred to the piles. Care was taken in the instrumentation plan to ensure that there was sufficient distance between the sensors to minimize local stress effects that they might have on one another. Again, the locations were duplicated so as to provide measurement redundancy.

The installation of the EPCs involved several steps. First, a small pit was excavated. Several inches of sand identical to that used in the EPC soil calibration were placed and compacted in the same manner as in the calibration. The sensor was placed and leveled, then covered with an additional sand layer, which was also compacted. Initial readings were taken on all sensors. Cables were run through a flexible conduit to the data collection box.

Vibrating-wire EPCs were used in unit cell 1, while semiconductor-based EPCs were used in unit cell 2. Both types of sensors were of identical geometry [4 ½ in. (11.4 cm) diameter] and nearly identical capacities [about 25 psi (170 kPa) and 23 psi (160 kPa), respectively].

EPCs were not installed on top of the piles, mainly because previous studies (Rathmayer 1975, Reid and Buchanan 1984) have indicated that the vertical stress distribution above the pile cap is strongly non-uniform, with lower than average stresses measured near the center of the pile cap

and higher than average stresses measured at the edge of the pile cap. It was expected that the load due to the stress above the pile cap would be equal to the load on the piles, which would be calculated from pile strain readings.

Settlement systems

Settlement systems consist of a pressure transducer clamped to a square steel plate. The pressure transducer is connected via a fluid line to a fluid reservoir, which is installed in an enclosure, preferably near the data acquisition system (Figs. 3.13 and 3.14). The fluid line and reservoir contain a specific mixture of anti-freeze and water, such that the transducer measures pressure of the fluid above it. Assuming the reservoir elevation remains constant, the pressure change at the transducer resulting from a change in the vertical position of the settlement plate can be converted to distance with a calibration factor. The particular type of settlement system used in the present study (Geokon model # 4650-1-70KPA) was designed to measure up to 10 psi (70 kPa) of pressure, or a 21 ft (7 m) difference in elevation between the reservoir and the settlement plate. Calibration factors were provided by the manufacturer. A small laboratory test was performed to measure the sensitivity and accuracy, and is described separately in Appendix A.

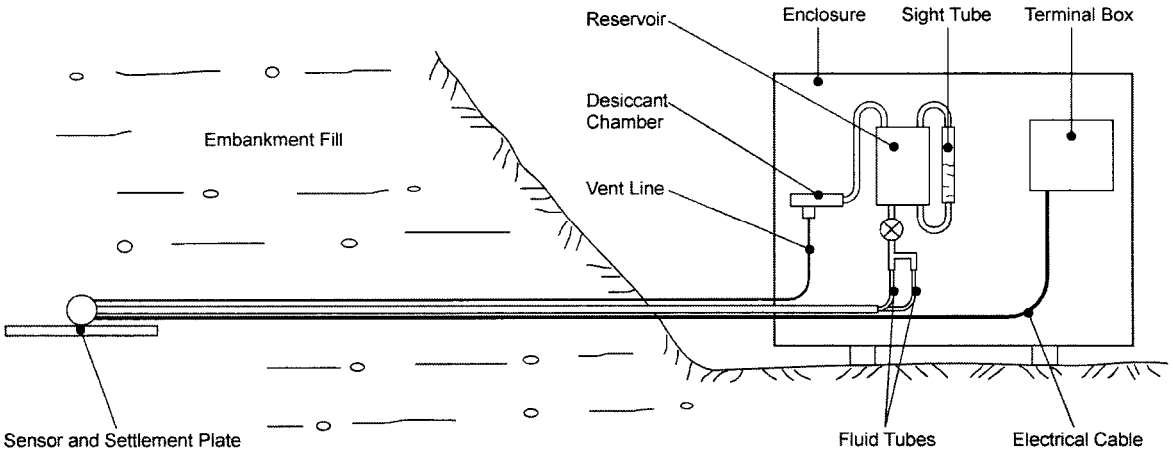

Figure 3.13. Diagram showing components of the settlement system. (Geokon 2005).

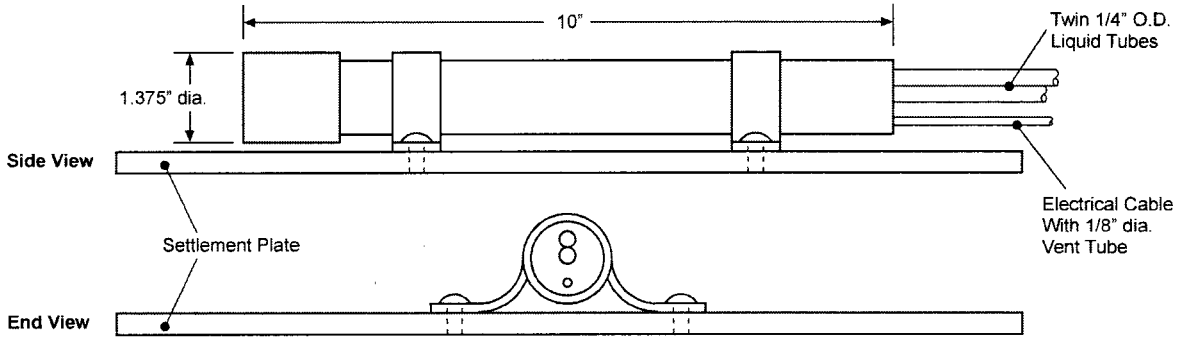

Figure 3.14. Diagram showing a close-up of the settlement plate with mounted pressure transducer. (Geokon 2005).

Settlement systems were installed at the same locations as the earth pressure cells in unit cell 1. It was assumed that settlement would be greatest at these points. Both sensors were offset slightly from the "point of interest" in order to minimize inclusion effects on the surrounding stress field of the EPC. No settlement systems were installed directly above the pile caps, as it was assumed that any settlement would be due solely to elastic deformation of the piles, and that quantity would be negligible.

The installation procedure followed was identical to the EPC installation, except that sand was not necessary, and fluid lines needed to be connected to the reservoirs once ready. A large quantity of excess cable remained, as it was initially anticipated that the enclosure used for data collection would be located further away from the instrumented region. However, splicing of the fluid lines was considered to be prohibitive and risky, so the excess cable was buried adjacent to the enclosure.

Figure 3.15. Installation of EPC (left) and settlement system (right) at the base of the LTP.

3.3.3 Top of platform

Six (6) sensors were installed at the top of the LTP. Two EPCs were installed in each unit cell: one above a pile, and another at the centroid of a triangular pile group. The purpose of this layout was to investigate whether load transfer or arching was occurring above the LTP. It was anticipated that if arching was taking place within the LTP, vertical stresses above the LTP would be relatively uniform.

Two settlement systems were installed at the top of the LTP in unit cell 1, in the same locations as the EPCs. Both types of sensors were offset slightly from the "point of interest" in order to minimize inclusion effects that the settlement system might have on the stress field around the EPC.

3.3.4 Geogrid

Foil strain gages were used to measure strain in the geogrid.

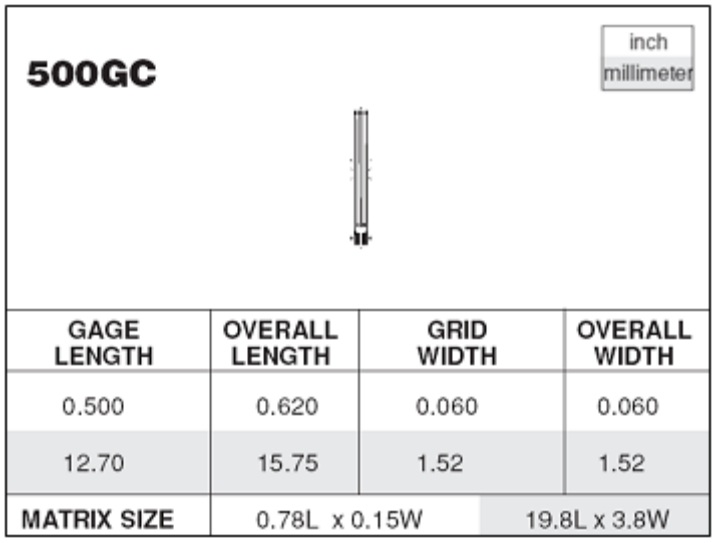

GAGE LENGTH	OVERALL LENGTH	GRID WIDTH	OVERALL WIDTH
0.500	0.620	0.060	0.060
12.70	15.75	1.52	1.52
MATRIX SIZE	0.78L x 0.15W		19.8L x 3.8W

Figure 3.16. Chart showing dimensions of 500GC series gages (http://www.vishay.com/strain-gages/gages-sensors/).

Geogrid layers 1 and 3 were instrumented identically with strain gages (Micromeasurements EP-08-500GC-350). A roll of the grid was obtained from the field site and brought back to the laboratory for the installation of the gages. An array of 10 gages at 5 locations oriented parallel to the highway centerline, centered over pile P2 (point 7036 on plans). Two gages were installed at each location, one oriented parallel to the highway (labeled "L" for longitudinal) and the other oriented perpendicular (labeled "T" for transverse). The idea of this layout was to get a "profile" of the strain from the pile to the pile group centroid, and determine where the greatest strain was occurring. Centering the array over P2 allowed for some redundancy of measurements.

The method used to install strain gages on the geogrid was adapted from a study of various installation methods that measured gage survivability (Warren et al. 2005). The geogrid was first cleaned and then slightly abraded, as the surface of the particular grid was very rough (see Figs. 3.17 and 3.18). A thin strip of silicone adhesive (Dow Corning 3145) was applied to the surface of the geogrid prior to the placement of the gage. A padded weight was placed over the gage for several of hours as the silicone set. After the adhesive had set, the same silicone adhesive was used to waterproof the gage and wire. Additional coatings of M-Coat B were applied before wrapping the instrumented area with electrical tape. A final coat of M-Coat B was applied to the exterior of the electrical tape.

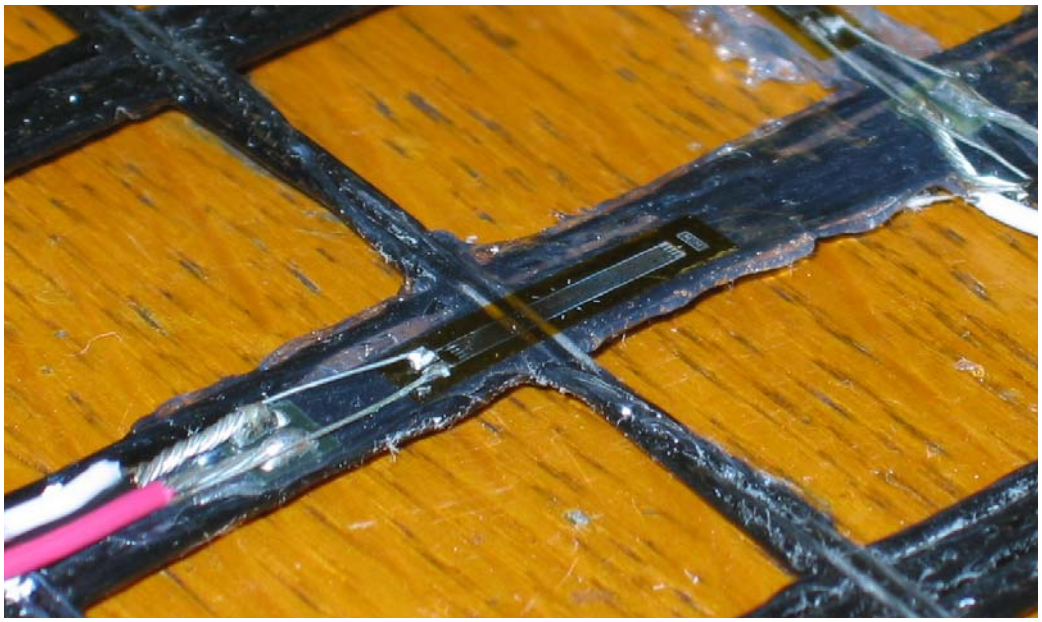

Figure 3.17. Installation of strain gage on geogrid prior to application of waterproofing and protection.

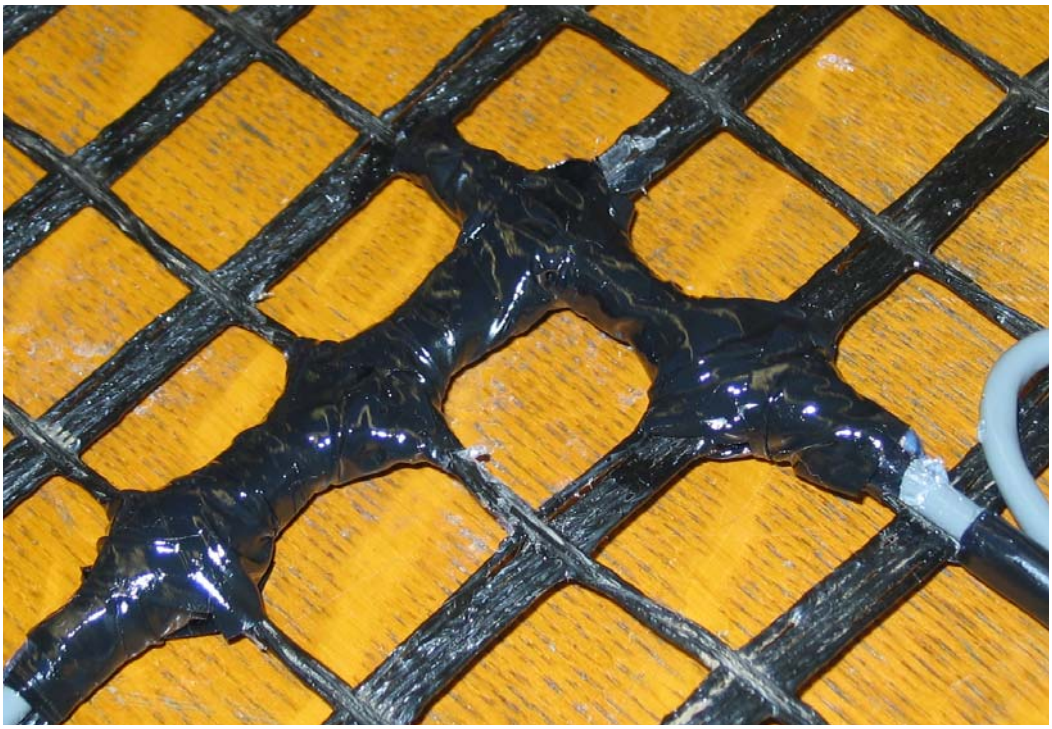

Figure 3.18. Installation of strain gage on geogrid following application of waterproofing and protection.

3.3.5 Data collection system

The data collection system consisted of one datalogger (Campbell Scientific CR10X and five multiplexers (Campbell Scientific AM16/32), one Vibrating Wire interface (Campbell Scientific AVW1), one 16MB storage Module (Campbell Scientific SM16M-ST). The datalogger was powered by a 12V marine-style battery, which was recharged by a regulated solar panel (Campbell Scientific SP-2R) installed on top of the enclosure.

The data collection system was housed in a large enclosure installed at the toe of the embankment slope. The enclosure also contained the reservoirs for the settlement systems. Because the reservoirs are supposed to provide a benchmark for the sensors, so that the only change in head measured by the pressure transducer is due to the movement of the sensor, it was important that the enclosure move as little as possible during and following construction. The substantial weight of the enclosure and its location in the thick organic soils at the edge of the pond presented the possibility of settlement due to consolidation. In order to mitigate any settlement of the enclosure, it was supported at each corner by 12 ft (3.7 m) long 4 in. x 4 in. (10 cm x 10 cm) wooden posts pushed into the ground.

3.4 Difficulties with installation

A number of unforeseen difficulties and setbacks were encountered in the course of installing the instrumentation and data acquisition system. Some had a fairly substantial impact on the project while others were minor. Some were preventable, while others could not have been predicted.

3.4.1 Loss of sensor readings

Perhaps the most serious setback encountered was that readings from a number of sensors were lost following installation.

- Pile gages: All four foil strain gages installed on the piles were lost. Initial readings were obtained on some of the gages, but were sporadic and appeared to be unreliable. One of the four vibrating wire strain gages on the pile wall was lost, and one of the two embedment gages was lost.
- Strain gages: Of the 20 strain gages that were installed on the geogrid, two did not survive the initial laboratory installation, and another 10, mostly on geogrid layer 1, did not survive the field installation. The reason for the losses is unknown, though the fact that the losses were concentrated on layer 1 suggests that survival was not random.
- Settlement Systems: Readings from one of the six settlement systems were lost following installation.

3.4.2 Late installation of enclosure

Another setback encountered was that the enclosure was not installed prior to the installation of the first sensors, the strain gages on the piles. This was a result of a combination of factors,

including a lack of coordination and communication with the contractor, pressure to adhere to the construction schedule, and unexpected weather. Although in principle this would have only affected the pile gages, the fast construction pace required that most of the attention be focused on the critical task of installing the sensors, which left little to no time to set up the data collection system. While a few manual readings were taken prior to the installation of the automated datalogger, the first regular readings began following the construction of the LTP. The result was a lack of initial readings for the foil strain gages, both on the pile and on the geogrid, as well as a lack of readings for all sensors during the construction of the LTP. Fortunately, readings were obtained from most sensors during the placement of the remaining embankment fill.

3.4.3 Initial faulty readings

Another problem encountered dealt with readings of the semiconductor-based EPCs. Initially, the same battery used to supply power to the datalogger was used to provide excitation to the semi-conductor EPCs. However, readings taken from the data logger were erratic and did not match manual readings. After about two weeks of trying to resolve the issue, it was finally decided to use excitation from the datalogger, which provided less voltage that was desired but was ultimately successful. Unfortunately, because of this delay, readings from the initial phase of embankment fill were lost.

Chapter 4
Measurements

4.1 Pile gages

Locations of the pile gages were discussed in Chapter 3. Figure 4.1 shows locations of the functioning gages.

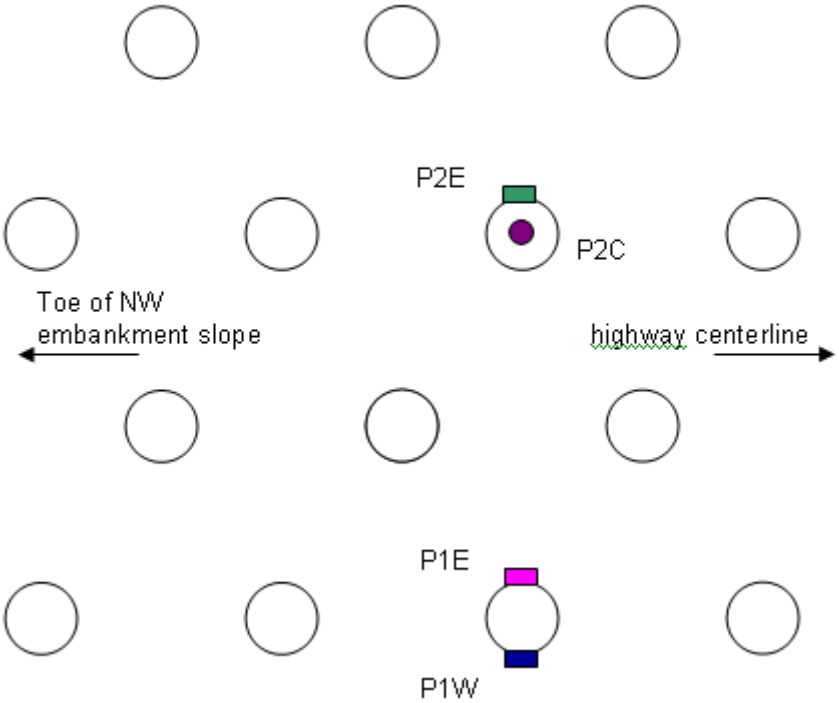

Figure 4.1. Plan view diagram showing locations of functioning pile strain gages in unit cell 1.

4.1.1 Gages in concrete

As was stated in Chapter 3, one of the two embedment gages (P4C) malfunctioned following installation and did not provide readings. The other embedment gage (P2C) gave readings, although they were somewhat erratic. The data showed several wave-like layers of data as shown in Fig.4.2. The best-defined of these "layers," the lowermost, was chosen and the remaining data was filtered out. It should be emphasized, however, that the data from P2C are not considered to be very reliable, as it appears that the gage malfunctioned.

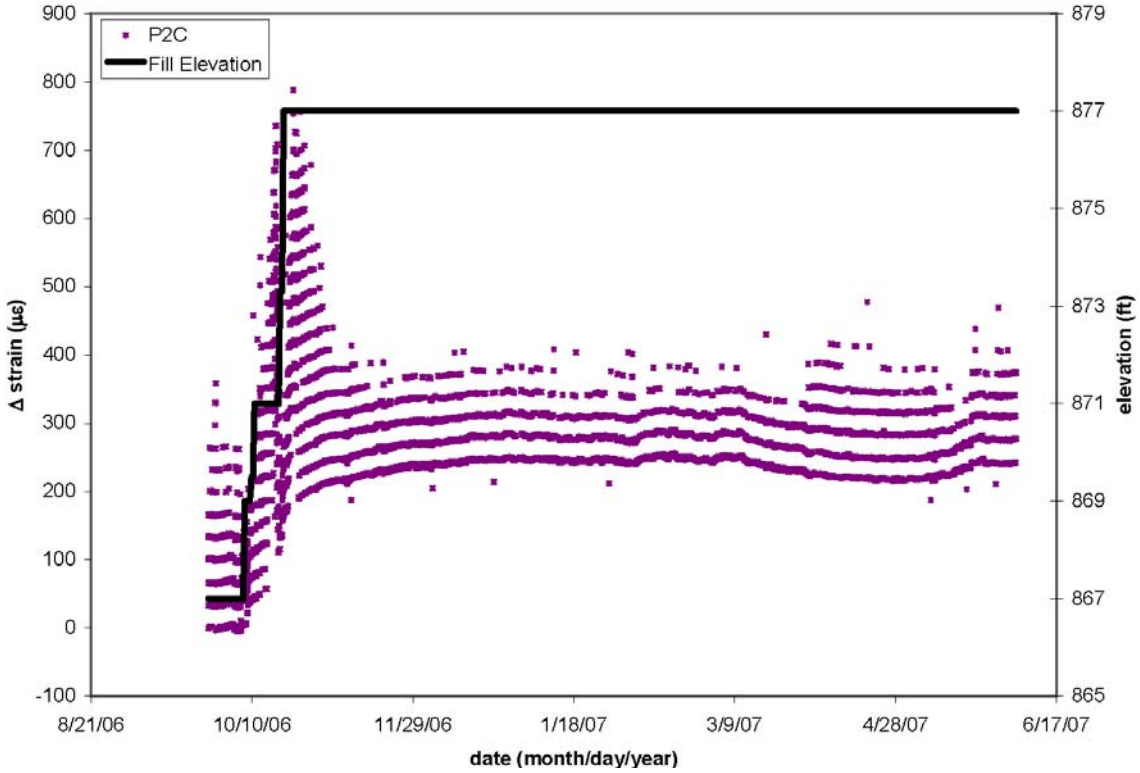

Figure 4.2. Strain measurements on piles. Fill elevation is plotted on the secondary y-axis for comparison.

4.1.2 Gages on steel pile wall

Data from the functioning gages on the pile wall (P1E, P1W and P2E) follow a nearly identical trend, but exhibit varying absolute values. Figure 4.3 shows a plot of the pile gage readings, including P2C, over time. Figure 4.4 shows the same plot over the period of backfilling. Note that the increase in strain due to added backfill is not instantaneous, but rather is time dependent. The completion of backfilling occurred on October 10, 2006, yet readings continue to increase until reaching a plateau near the end of December 2006.

As mentioned previously, the pile gages yielded varying values of strain. The difference is especially significant for readings on pile 1. Strain readings from June 4, 2007, when the most recent data was collected were as follows: $\varepsilon_{P1W} = 327\ \mu s$, $\varepsilon_{P1E} = 538\ \mu s$, $\varepsilon_{P2E} = 460\ \mu s$. That is, strain in P1E was 65% greater than that of P1W on the same pile. Strain in P2E was 41% greater than the strain in P1W.

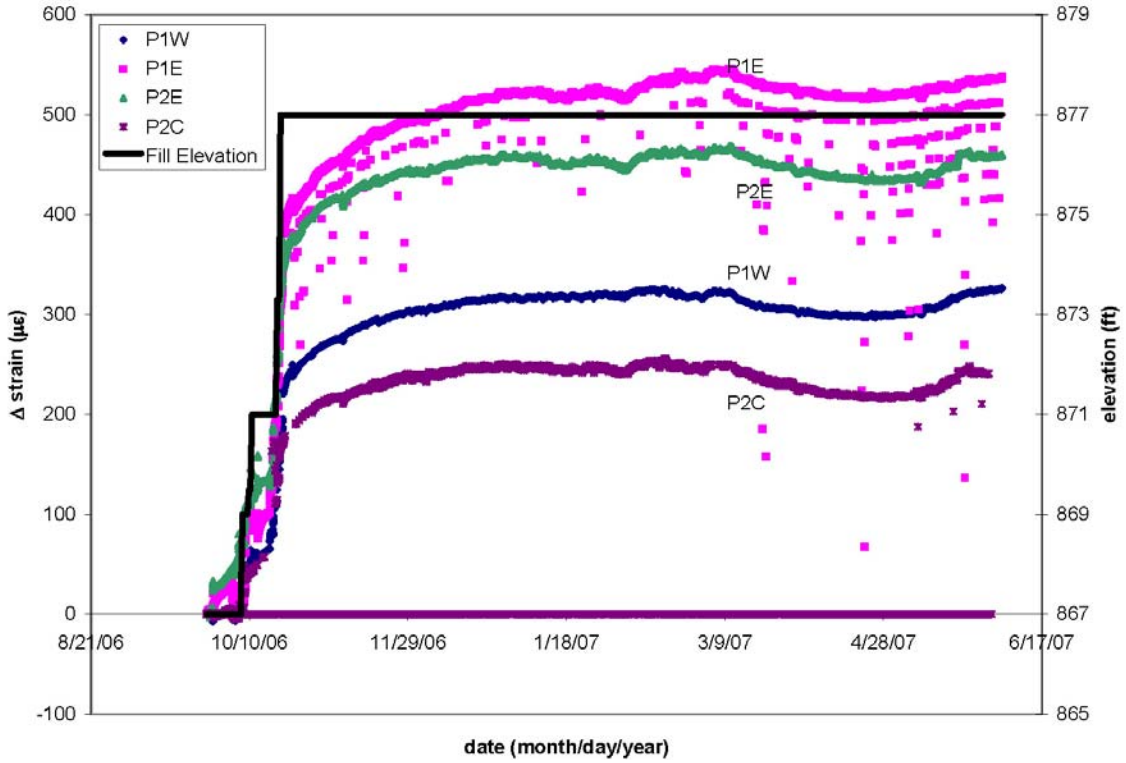

Figure 4.3. Strain measurements on piles. Fill elevation is plotted on the right y-axis for comparison.

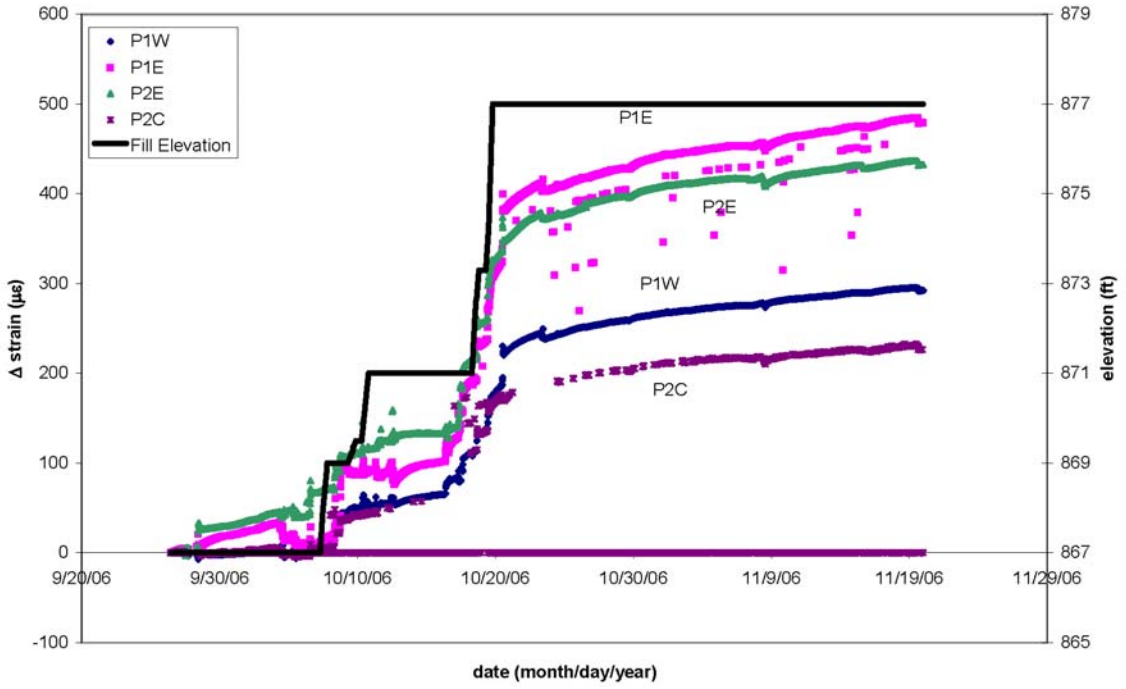

Figure 4.4. Strain measurements on piles during backfilling. Fill elevation is plotted on the right y-axis for comparison.

Assuming a displacement boundary condition and known properties of the pile, the load can be calculated (details are presented in Appendix D). The corresponding average load that was estimated to be representative of the system is 119.5 kips (530 kN), which exceeds the design load of 90 kips (400 kN). There are a couple possible explanations for the greater load.

One possible explanation has to do with the vibrating wire strain gages. The sensitivity of these gages is typically given in a batch calibration factor, in which a small sample of a production batch is calibrated, and the average sensitivity of that sample is used for the entire batch. For example, in order to calculate a measured load equivalent to the design load, the sensitivity would need to be 25% lower than the batch calibration factor. For the computed load to be equal to the estimated tributary load, the sensitivity would need to be 33% lower than the batch factor. Previous work in which laboratory calibrations were performed on similar gages has shown that the sensitivity can vary by 30% of the batch sensitivity. This could also account for the variation in strain among the gages, since it was anticipated that they would measure about the same strain.

Another potential explanation of the high calculated load is that the piles from which the measurements were taken are supporting a load from outside their tributary area, or the hexagonal area surrounding each pile. The FEM study of the embankment showed that piles in the row that was instrumented in fact support a greater load than piles in other rows, although the magnitude of the result does not match measurements. Unfortunately, since measurements from other pile rows were not made, this explanation cannot be verified.

4.2 Earth pressure cells

Earth pressure was measured at the base of the LTP between the piles, and at the top of the LTP directly above piles and between piles. It was anticipated that EPCs at the base of the platform would register very little earth pressure, due to the transfer of embankment load. Earth pressure cells at the top of the LTP, it was expected, would register roughly the vertical stress due to the overburden, regardless of their location relative to piles. This expectation was based on the assumption that load transfer via arching was to occur entirely within the LTP.

It should be noted that all EPC readings were found to be affected by the sensor temperature at magnitudes beyond the factory specifications. A correction factor was applied in order to minimize the effect, and is explained more thoroughly in Appendix C, where the original data is provided. The readings including the temperature correction were determined to be more meaningful, and were therefore chosen to be presented in this section.

4.2.1 EPCs at the base of the LTP

Figures 4.5 and 4.6 show the locations of the vibrating wire EPCs and the semiconductor EPCs at the base of the LTP in unit cells 1 and 2, respectively. Recall that the sensors were installed in two different locations relative to the triangular group. Half of the EPCs at the base of the

platform were installed at the centroid of a pile group (numbers 1, 4, 5 and 8), while the other half (numbers 2, 3, 6 and 7) were installed at the midpoint between two adjacent piles. Plots of EPC readings between piles at the base of the platform are shown in Figs. 4.7 through 4.9. Unfortunately, readings from the semi-conductor EPCs (unit cell 2) during backfilling were not obtained due to difficulties described in Chapter 3. However, all four vibrating wire EPCs functioned well during the backfilling (Fig. 4.8).

EPCs at the base of the LTP all showed very similar behavior. An increase in the readings is observed at the end of each period of fill placement, followed by a rapid decline in the reading. After the backfilling was completed on 10/20/06, readings decrease steadily until reading a steady value between -1 and 3 psi (-6.9 and 20.7 kPa). Recall that initial EPC readings were taken following the construction of the LTP and the placement of about 1ft (0.3 m) of fill, so readings from EPCs at the base of the LTP do not include the loading due to the fill placed prior to the initial reading. In other words, a negative reading does not imply a negative stress, but simply a lower stress than at the time of the initial readings. It is worth noting that among the semiconductor-based EPCs, the most recent readings show similar readings by location. That is, BP_EPC5 and BP_EPC8, at the centroid locations, have similar readings, while readings from BP_EPC6 and BP_EPC7, at midpoint locations, are also similar.

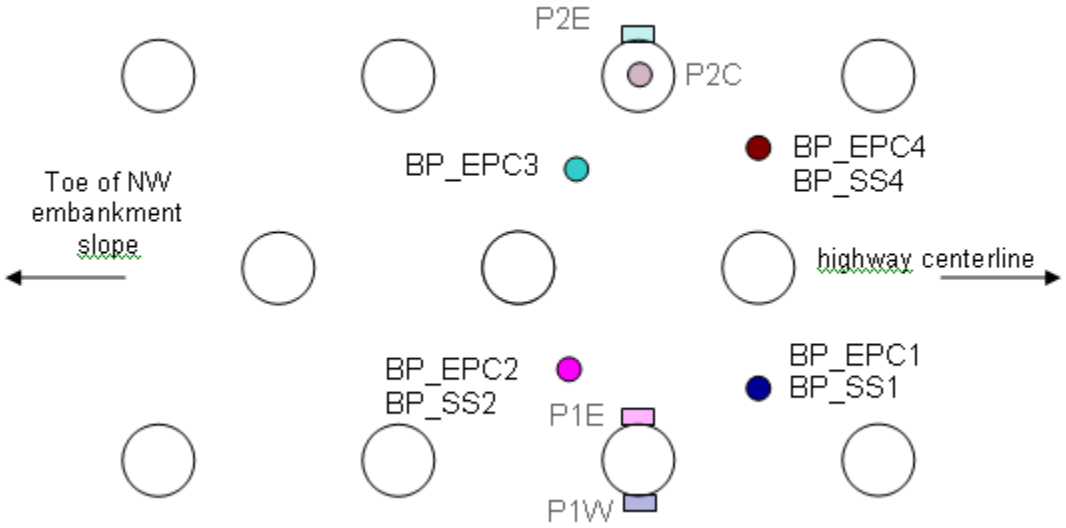

Figure 4.5. Plan view diagram showing locations of EPCs and settlement systems in unit cell 1. Locations of functioning pile gages are superimposed for reference.

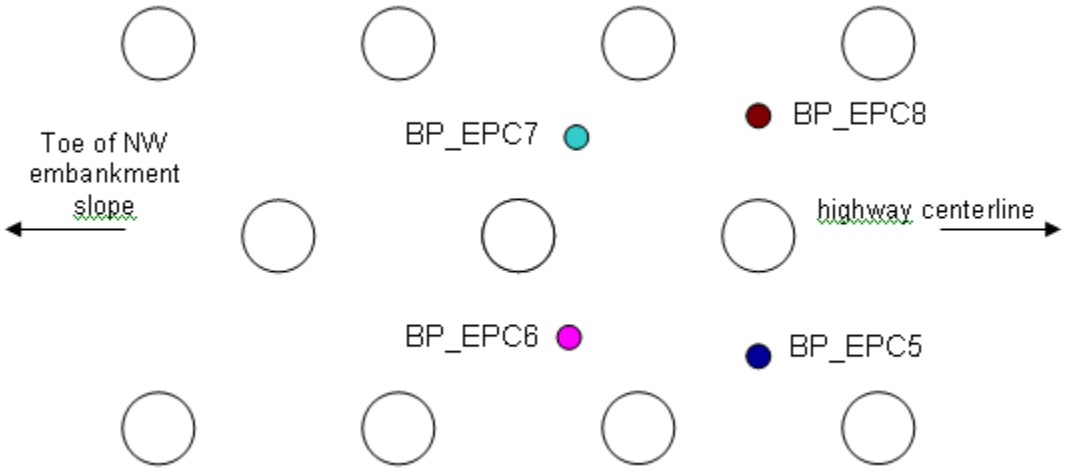

Figure 4.6. Plan view diagram showing locations of EPCs in unit cell 2.

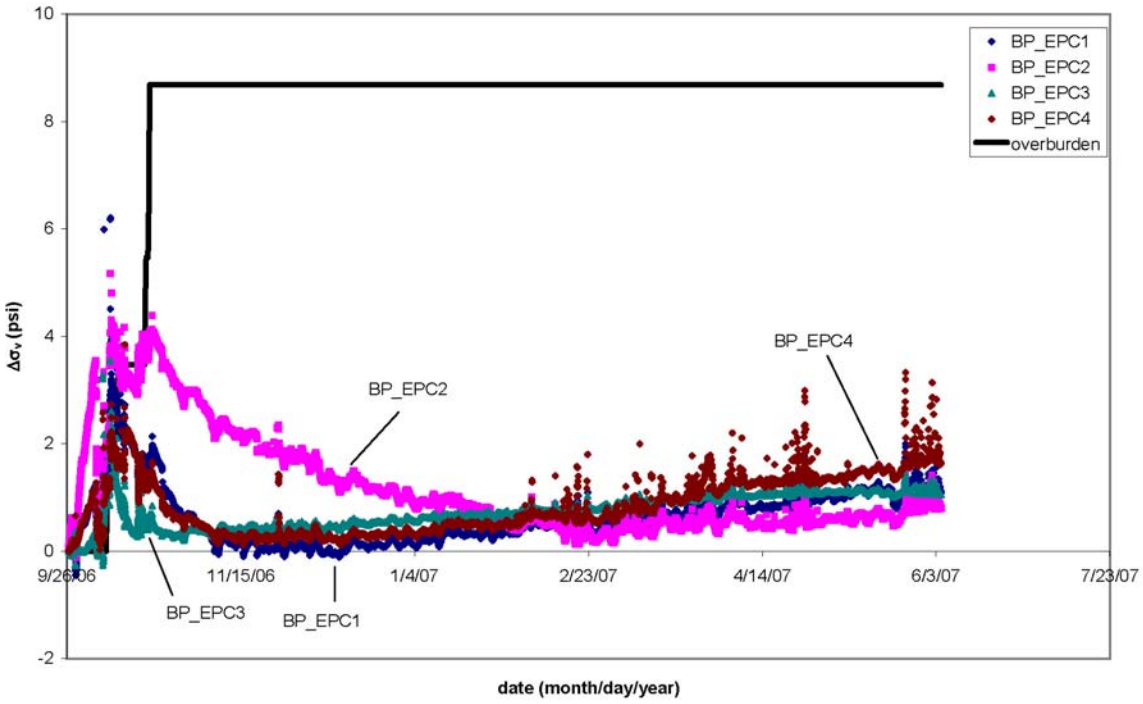

Figure 4.7. Vertical stress between piles at the base of the LTP in unit cell 1. Theoretical vertical earth pressure (γH) due to the embankment fill is plotted for comparison.

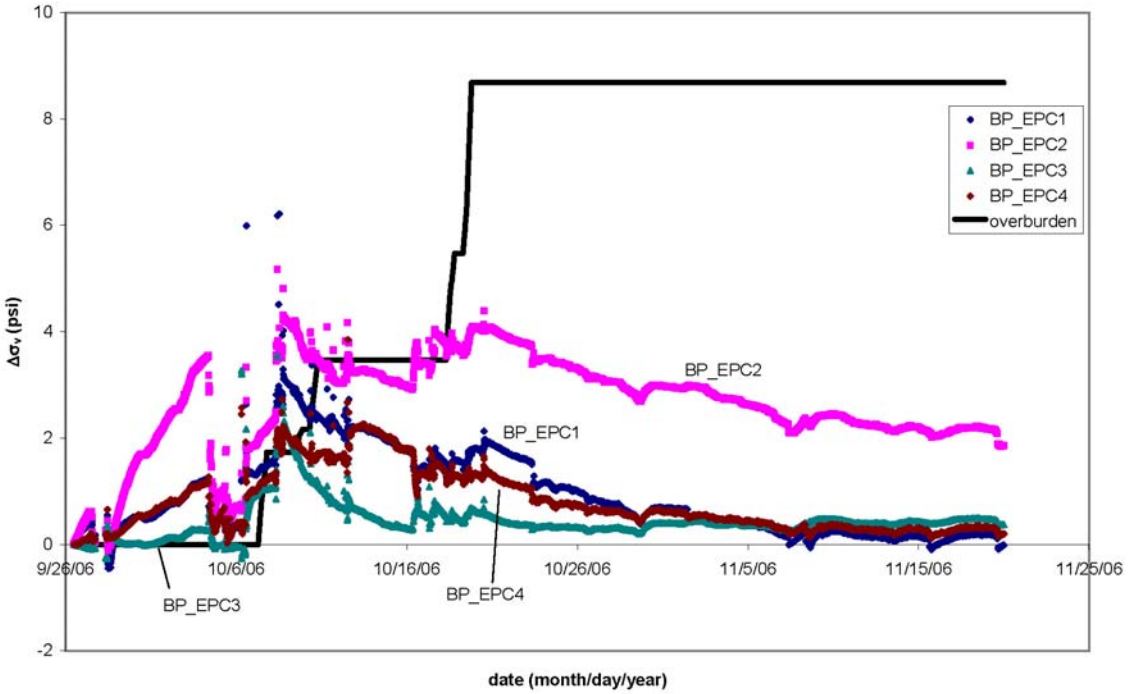

Figure 4.8. Vertical stress between piles at the base of the LTP in unit cell 1 during backfilling. Theoretical vertical earth pressure (γH) due to the embankment fill is plotted for comparison.

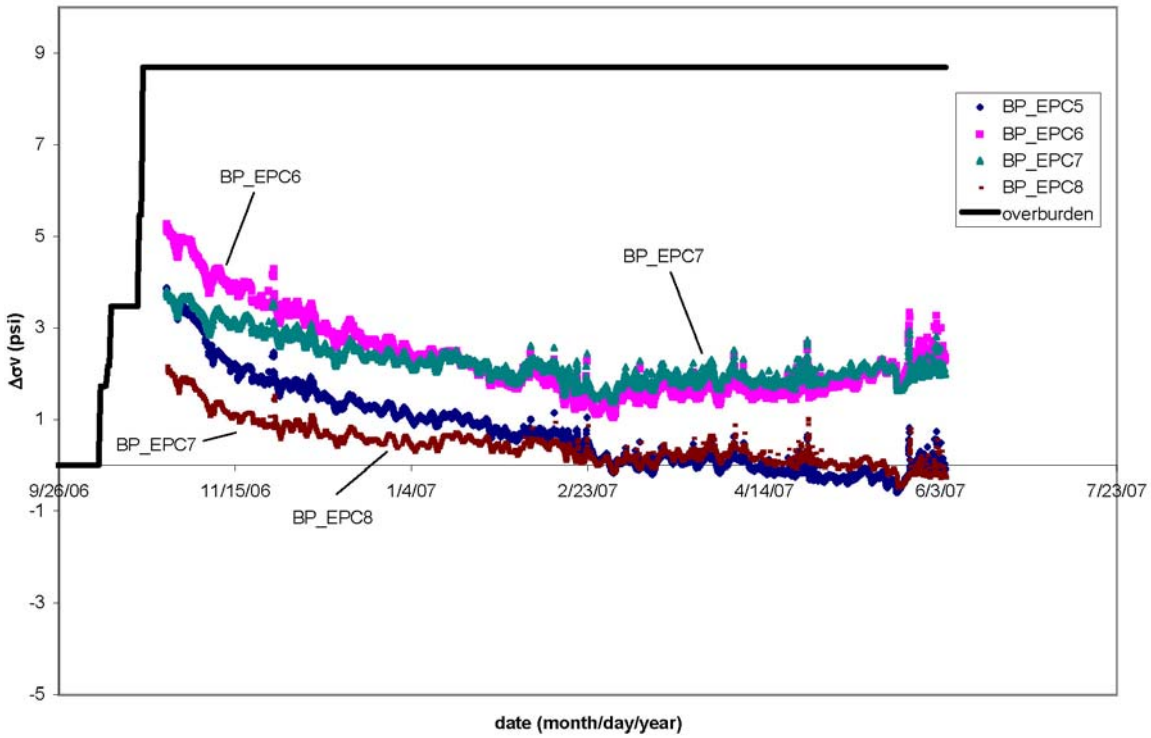

Figure 4.9. Vertical stress between piles at the base of the LTP in unit cell 2. Theoretical vertical earth pressure (γH) due to the embankment fill is plotted for comparison.

Earth pressure readings at the base correspond with what is expected based on the design. Loading develops above the EPCs initially until enough embankment fill is available to transfer the increasing embankment load to the stiffer regions of the platform surrounding the piles. As the soil settles, the regions of soil involved in arching stiffen in response to the load, relieving the areas between the piles of the load. Nearly all the embankment load appears to be transferred to the pile, either directly via arching or indirectly via the geogrid tension membrane effect.

4.2.2 EPCs at the top of the LTP

Recall that four EPCs were installed at the top of the platform, divided evenly between the two unit cells. One EPC per unit cell was installed above a pile, and the other was located at the centroid of the triangular pile group (Figs. 4.12 – 4.14).

The two EPCs at the centroid location showed behavior very similar to that of the EPCs at the base of the LTP. Readings rose during periods of backfilling to between and fell between those same periods. Finally, readings decreased and stabilized around zero.

The EPCs above the piles at the top of the LTP behaved differently. Figures 4.9 and 4.10 are plotted with estimated average vertical stress due to overburden, γH. Readings increased substantially during backfilling and reached a plateau of between 35 psi (240 kPa) and 65 psi (450 kPa). A temporary dip of around 5 – 10 psi (35 – 70 kPa) is then observed during mid-late April of 2007.

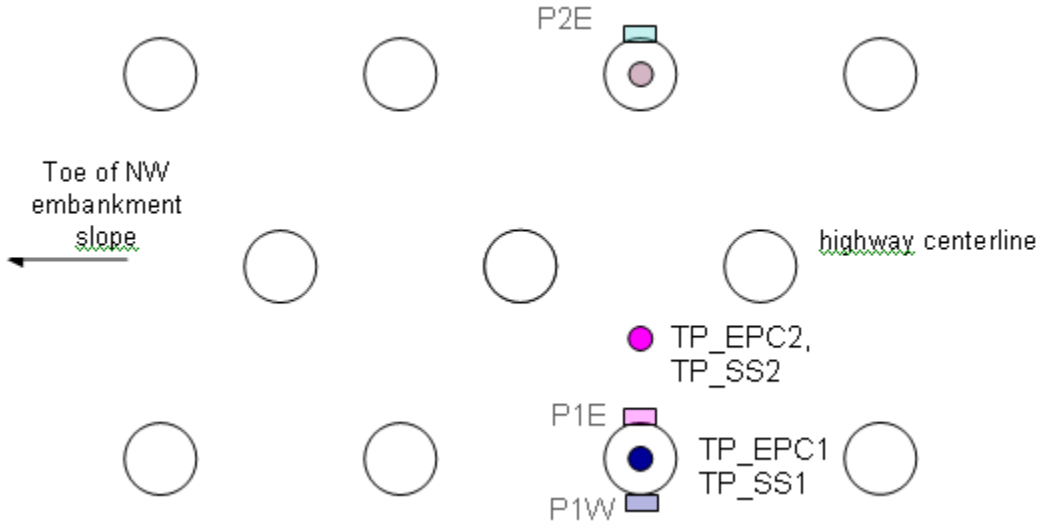

Figure 4.10. Plan view showing the locations of EPCs and settlement systems at the top of the LTP in unit cell 1. Locations of functioning pile gages are superimposed for reference.

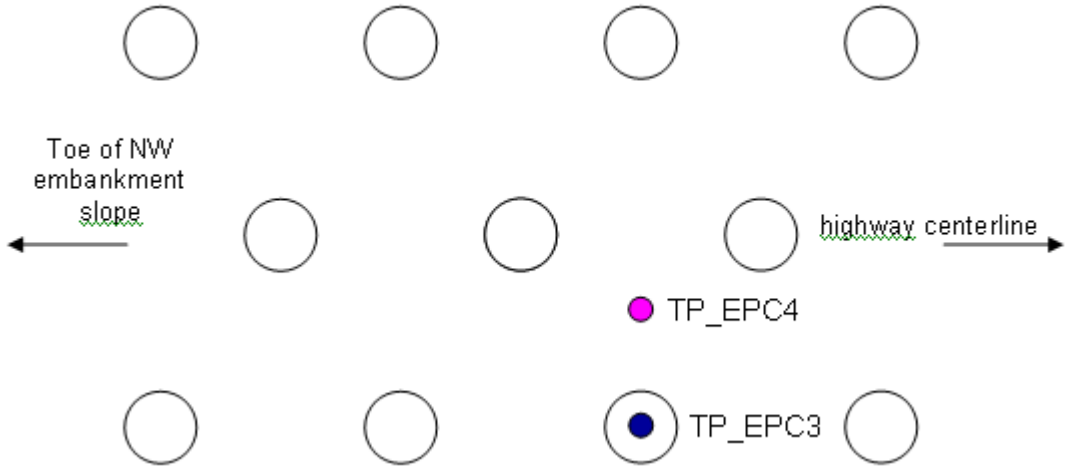

Figure 4.11. Plan view showing the locations of EPCs at the top of the LTP in unit cell 2.

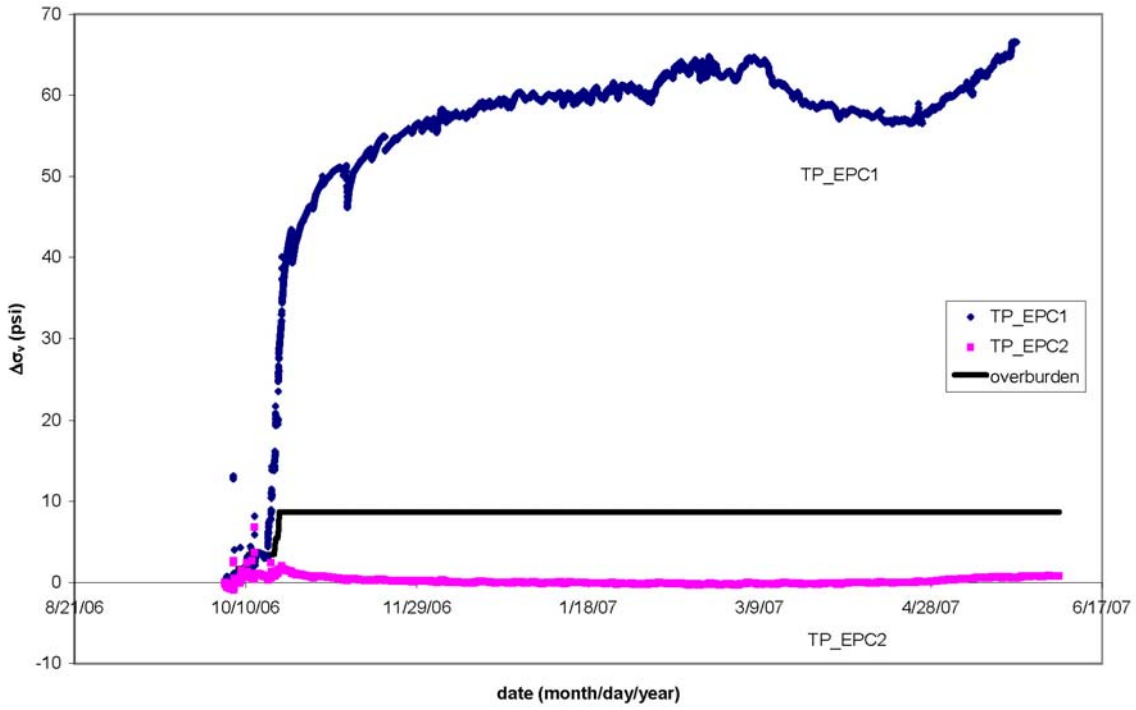

Figure 4.12. Vertical stress above (TP_EPC1) and between (TP_EPC2) piles at the top of the LTP in unit cell 1. Theoretical vertical earth pressure (γH) due to the embankment fill is plotted for comparison.

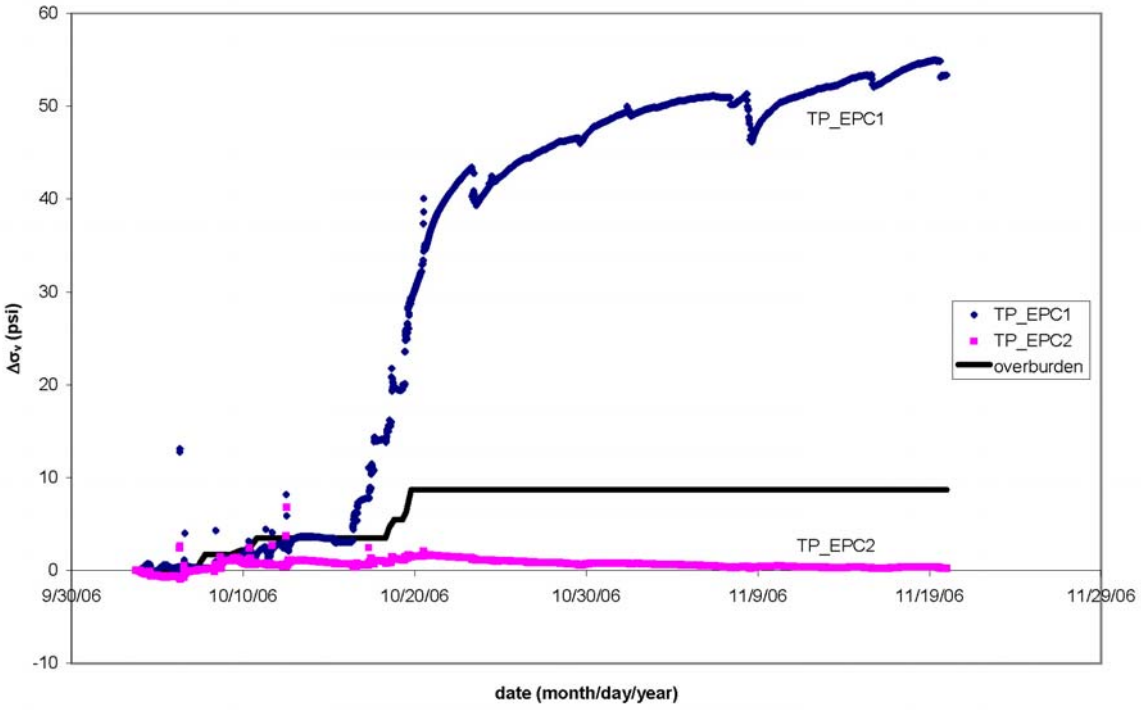

Figure 4.13. Vertical stress above (TP_EPC1) and between (TP_EPC2) piles at the top of the LTP in unit cell 1 during backfilling. Theoretical vertical earth pressure (γH) due to the embankment fill is plotted for comparison.

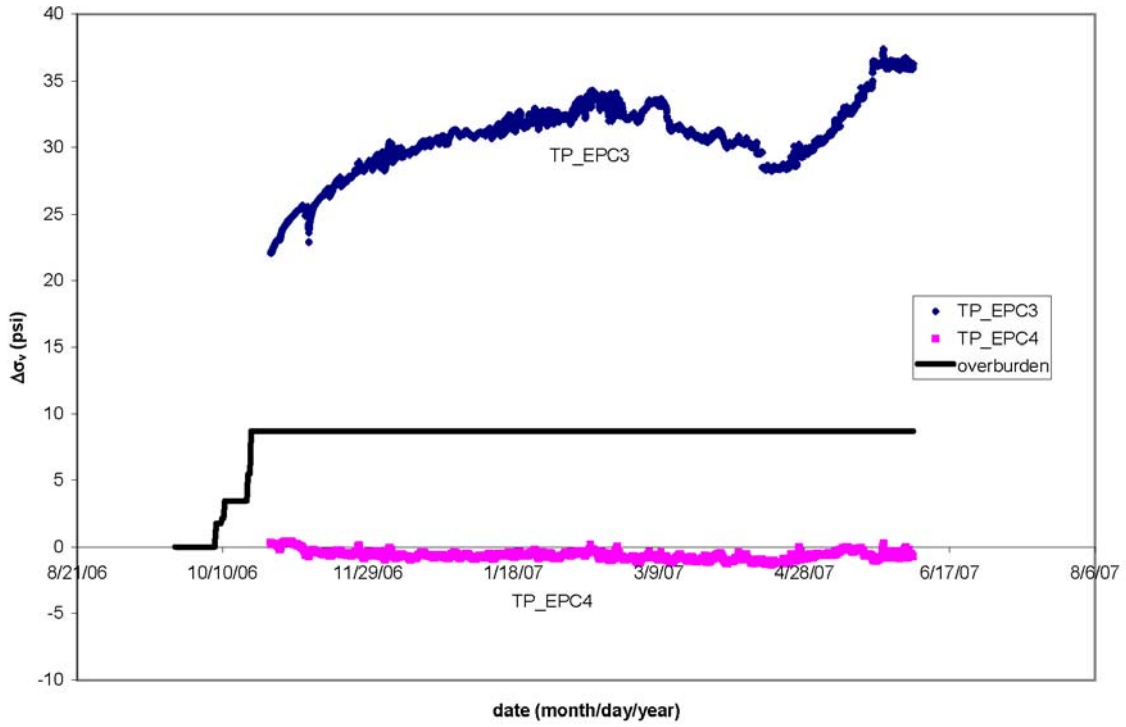

Figure 4.14. Vertical stress above (TP_EPC3) and between (TP_EPC4) piles at the top of the LTP in unit cell 2. Theoretical vertical earth pressure (γH) due to the embankment fill is plotted for comparison.

The results of the earth pressure readings at the top of the platform were unexpected. Earth pressure between piles was very low, while earth pressure directly above the piles was several times greater than the expected vertical earth pressure γH. These readings suggest that the vertical stress at the top of the platform is highly non-uniform, and that the load transfer is not confined to the LTP but rather takes place an unknown distance above the LTP also. That is, the embankment fill above the LTP plays a role in the transfer of the load.

4.3 Strain on geogrid

Strain measured on geogrid layer three (GL3) was found to be generally in the range of 1-2%, well below the design strain of 5% (Fig. 4.15). Most of the strain appears to occur during backfilling. Readings did not appear to depend on the location of the gage. No gages survived on geogrid layer one (GL1).

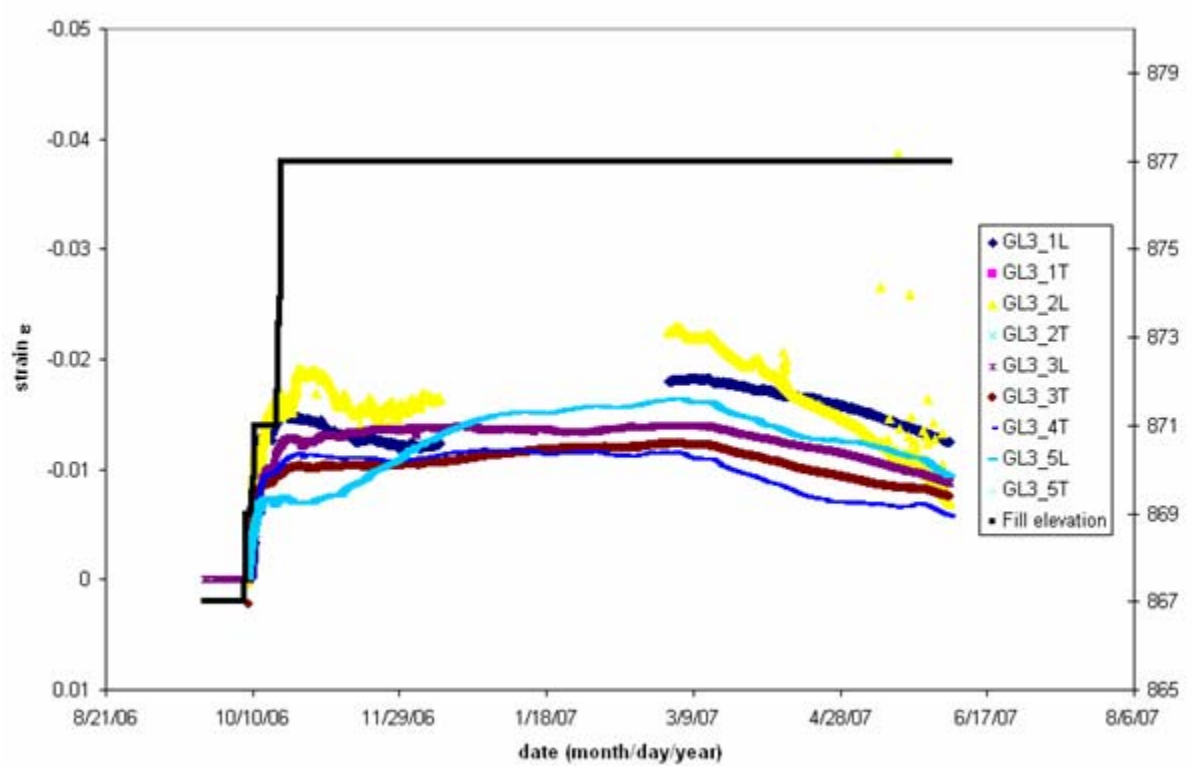

Figure 4.15. Strain on geogrid layer 3 (GL3). Fill elevation is plotted on the secondary y-axis for comparison.

4.4 Settlement systems

All settlement systems aside from BP_SS3 survived construction. A number of issues arose with the readings, however, raising doubts about their veracity. Settlement readings appeared to be influenced by outside factors. All readings display cycles that occur at a roughly daily frequency (Fig. 4.16), as well as a long-term trend similar to that exhibited by the EPC readings prior to the application of the temperature correction (Figs. 4.17 and 4.18). The cycles occurring on the scale of days appear to correlate well with air temperature measurements taken from the datalogger (shown in Fig. 4.16). The long term rise and fall of readings peaking in early to mid April correlates well with temperature measurements from the buried sensors (shown in Figs. 4.17 and 4.18).

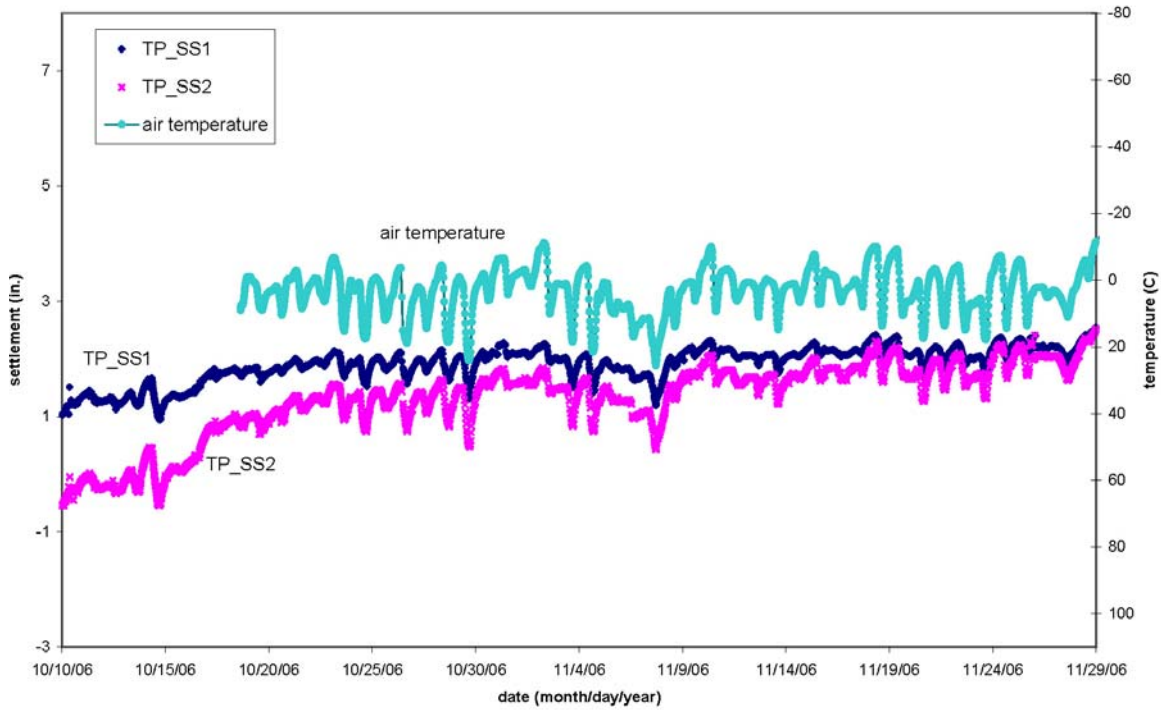

Figure 4.16. A selected portion of settlement measurements showing a correlation between readings (left y-axis) and air temperature taken from the datalogger (right y-axis).

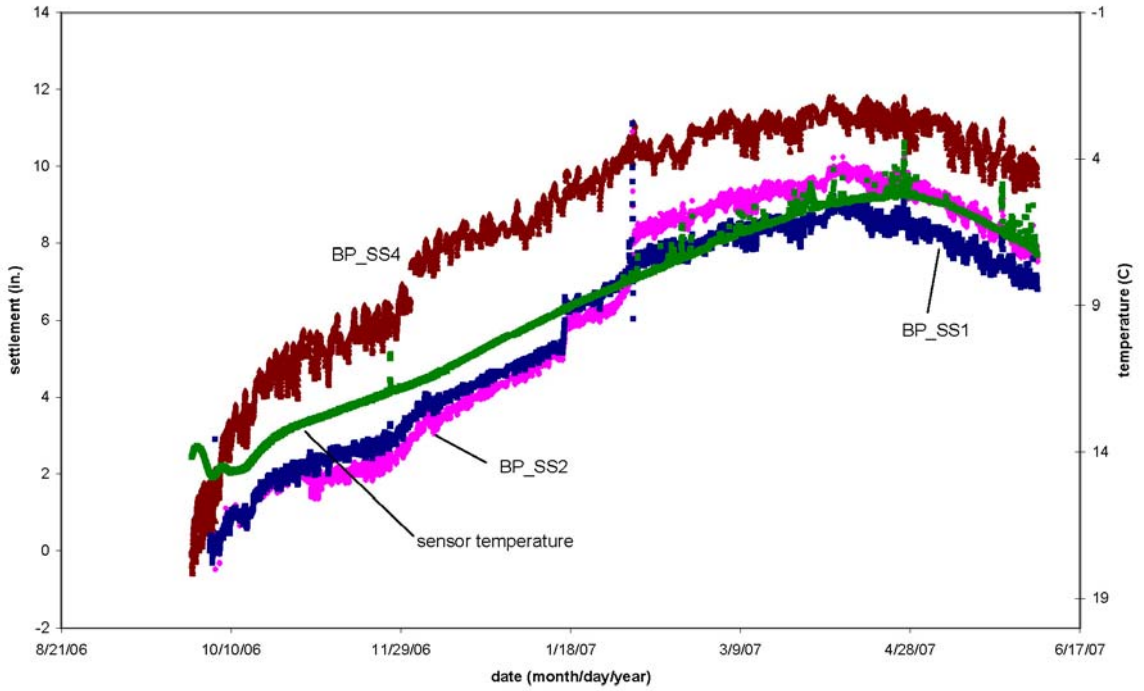

Figure 4.17. Settlement measurements at the base of the LTP showing a correlation between readings (left y-axis) and sensor temperature (right y-axis).

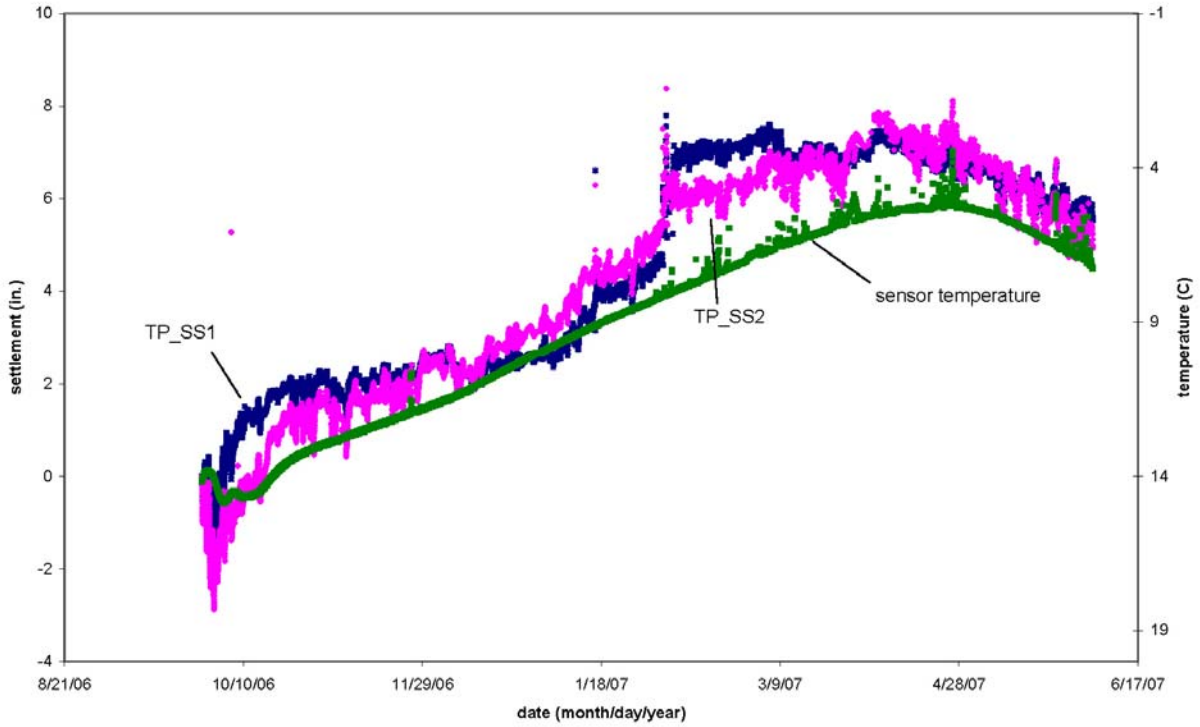

Figure 4.18. Settlement measurements at the top of the LTP showing a correlation between readings (left y-axis) and sensor temperature (right y-axis).

The data present other difficulties when compared to EPC measurements. Recall that at the top of the platform, settlement system TP_SS1 was installed at a position directly above a pile and TP_SS2 was installed at a centroidal location (refer to Fig. 4.7). Despite the vast difference in loading at those locations indicated by readings from TP_EPC1 and TP_EPC2 (Fig. 4.9), settlement measurements from TP_SS1 and TP_SS2 are essentially identical (see Fig. 4.14).

Readings from EPCs at the top of the LTP show that the embankment load quickly gravitated to the piles, so that all expected deformation should have occurred by the end of November, when EPC readings stabilized. Settlement measurements from that location, however, appear to be essentially independent of the loading, as they show major changes taking place after November.

Between the piles, where there is little foundation support and settlement is expected, EPC measurements show a small jump in readings during backfilling followed by a gradual decrease in load until, at the end of November, it is effectively zero. The decrease in the stress measurements suggests that the soil settled in response to loading and the initial load at that point was gradually transferred to the piles. Again, settlement readings are not consistent with this scenario, showing significant increases in settlement after November despite indications that the load at that location was effectively zero.

Furthermore, both settlement systems at the top of the LTP show measurements of up to 7 in. (17.8 cm). While settlement of that magnitude could be reasonable between piles, it is difficult to imagine a mechanism that would that amount of settlement within 3 ft (0.9 m) of well-

compacted fill above a nearly rigid pile. An estimate of the anticipated elastic deformation of the LTP can be obtained with a simple 1D calculation. Assuming a Young's modulus of 3000 psi (21 MPa) and a vertical stress such as that measured by TP_EPC1 (about 65 psi or 450 kPa), a strain of about 0.02 is computed. Within the 3 ft (0.9 m) thick LTP, that corresponds to 0.8 in. (2 cm) of deformation, an order of magnitude less than the measured settlement. It is worth noting also that previous studies in which settlement was measured (Gartung et al. 1996; Maddison et al. 1996) reported a maximum settlement of around 2 in. (5 cm) *between* piles, and much less above the piles.

The issues discussed above suggest that the settlement measurements do not provide a good representation of the actual response of the soil to the embankment loading. First, the readings do not match some very basic expectations of the response at the top of the platform. Furthermore, temperature effects, both long-term and short-term, appear to occur on a large magnitude relative to the readings themselves. Without knowing the precise nature of the temperature effects, it is impossible to accurately distinguish between changes in the readings due to settlement and changes due to temperature.

Chapter 5
Finite Element Modeling

5.1 Overview

Finite element (FE) simulations using linear elastic constitutive models were performed using STRAND7, Standard Version 2.3, a commercially available finite element software package. Quasi-static three dimensional analyses were used with eight-node isoparametric brick elements for the platform and the embankment, and four-node plate elements of negligible bending stiffness for the grid. The FE mesh was refined in order to have accurate numerical results verifying that the displacement and stress (strain) fields were significantly regular without any substantial gradients. The first numerical analysis considered the materials to be isotropic, defined by the engineering constants shown in Table 5.1.

Table 5.1. Mechanical properties of the system.

	Young's modulus (psi)	(MPa)	Poisson's ratio	Unit weight (pcf)	(kN/m^3)
Platform	14,500	100	0.3	130	20
Embankment	2,900	20	0.3	130	20
Grid	20	0.14	0.3	12	1.9

The second numerical analysis considered the platform a transversely isotropic material: in this case, five elastic constants are the Young's modulus E_p and Poisson's ratio ν_p in the x-z symmetry plane; the Young's modulus E_y and Poisson's ratio ν_{py} in the y-direction; and the shear modulus G_{zp} in the z-direction. It was assumed that the Young's modulus in the transverse direction (E_p = 1,450 psi or 10 MPa) was 10 times lower the Young's modulus in the vertical direction (E_y = 14,500 psi or 100 MPa).

The support provided by the piles was modelled as springs, with stiffness equal to the overall axial stiffness of the steel pile filled with concrete, assuming a modular ratio $n = E_s/E_c = 15$. Only the numerical results from the transversely isotropic platform will be presented because the numerical predictions were closer to the field data.

The FE mesh was composed of 38,719 nodes, 3,780 plate elements, and 37,800 bricks elements (Fig. 5.1), and this region captured the three-dimensional unit cell of the structure. The imposed boundary conditions were

(a) the vertical plane at the right boundary of the embankment was constrained by rollers that prevented horizontal displacements;
(b) the platform was supported by the piles with elastic deformability.

No constraints were placed on the slope and on the top of the embankment.
The vertical displacement (settlement) contours associated with self-weight loading is shown in Fig. 5.2. The maximum settlement of 0.8 in. (2.0 cm) developed on the crest of the embankment between the center of the crest and where the slope starts.

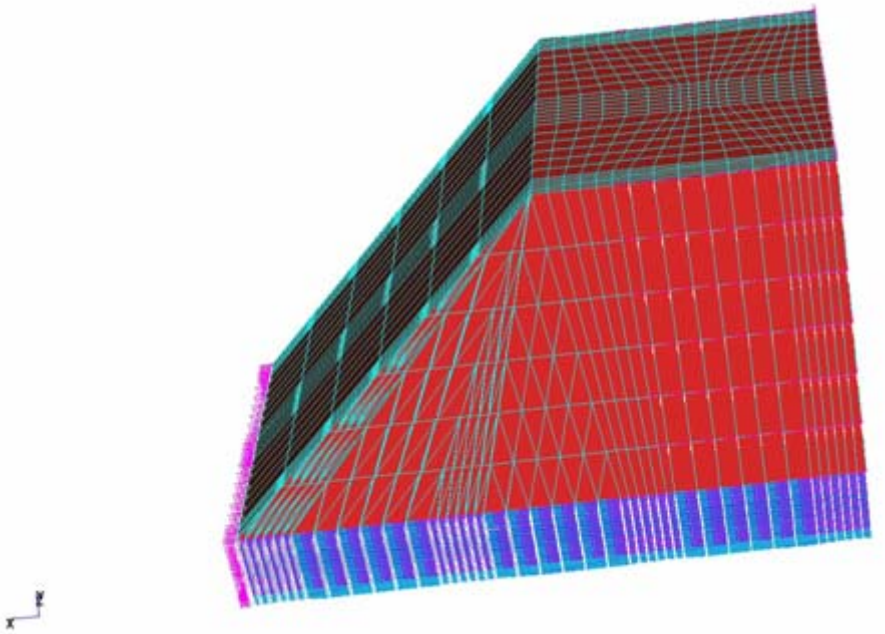

Figure 5.1. Finite element mesh capturing the three dimensional unit cell of the structure.

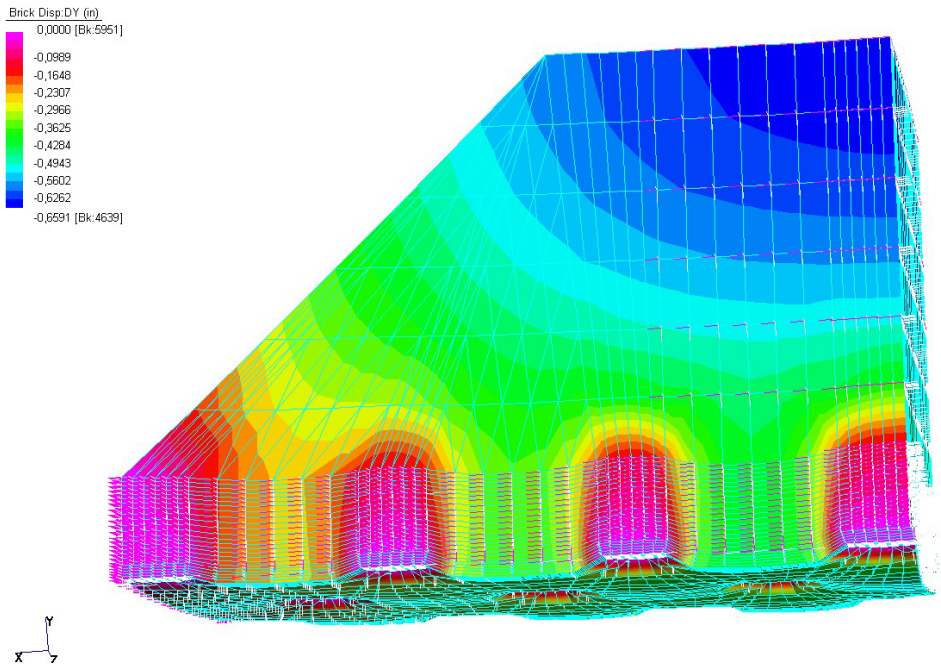

Figure 5.2. Vertical displacement contours.

5.2 Comparison with field data

The vertical displacements at the top of piles were negligible, enforcing the fundamental role of the piles in reducing the deformability of the embankment. The nodes at the bottom of platform between the piles have displacement of about 0.5 in. (1.3 cm). Enhanced displacement gradients can be noted close to the heads of the piles, suggesting critical situations in terms of strain (and stress) concentrations.

Axial loads on the piles are a basic comparison that can be made between the field data and the numerical modeling (Fig. 5.3). It is noted that the geometry and the three dimensionality of the structure produces a variation in pile loads. The maximum load on a pile was 81,500 lb (363 kN), about a 20% lower than the experimental result. Several factors should be considered. A variation of pile stiffness could account for one pile attracting load from its neighbors. In addition, a variation in strain gage sensitivity is within this 20% range.

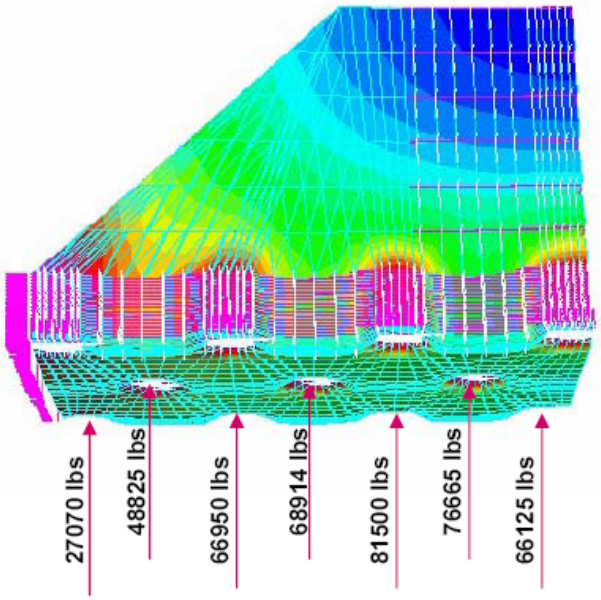

Figure 5.3. Axial loads on the piles.

The vertical stress distributions through the height of the platform along four different vertical positions are presented in Fig. 5.4. Three of the distributions (a, b, c) are above the pile and one (d) is between two piles where the pressure cells were positioned. The qualitative agreement between the modelling and the field measurements is good. At the elevation corresponding to the bottom of the platform (the top of the pile), the vertical stress above the pile is very large, and the distribution varies as a stiff footing on an elastic soil; the stress between the piles is zero. At the top the platform, the vertical stress above the pile is 10 – 20 times larger than between the piles; the measurements indicated a vertical stress above the piles of 30 – 50 times larger than

between the piles. The analysis shows that the vertical stresses in the piles are significantly less than their strengths, and the piles remain elastic under the embankment loads.

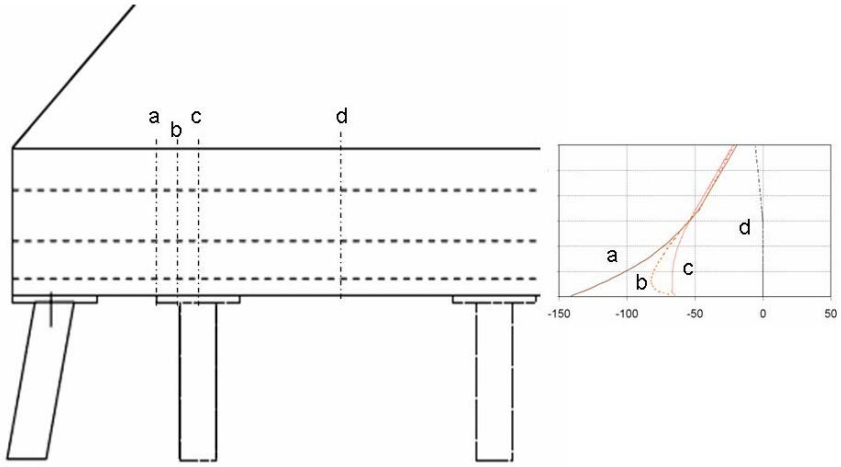

Figure 5.4. Vertical stress distributions at four positions within the structure.

Fig. 5.5 depicts the principal stresses in the model, with arrows in the mesh indicating the relative magnitude and direction of the stresses. The arching action in the embankment towards the piles is evident.

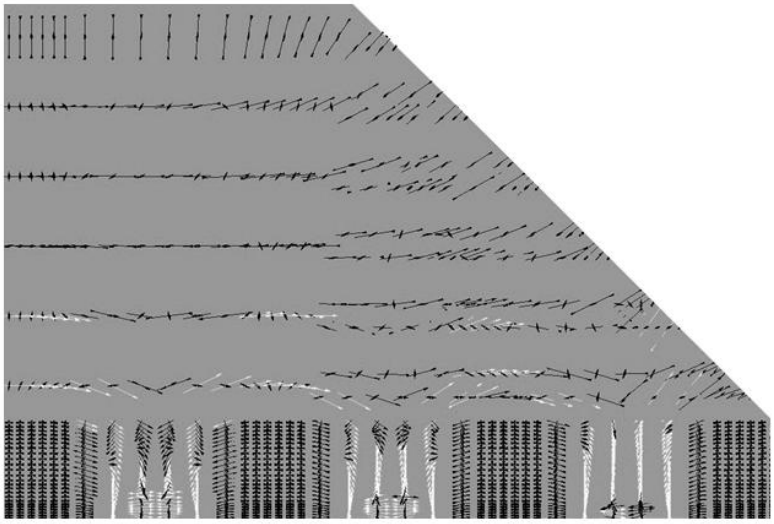

Figure 5.5. Principal stresses within a section of the structure.

The arching effect in the reinforced embankment was pronounced at the top of platform over the pile caps. Due to the significant axial stiffness of the piles in relation to the surrounding soil, it appeared that the pile extended through the platform and soil arching developed as a result of differential settlements between the stiff pile extensions and the soft soil. The mechanism of transferring the load is shown in Fig. 5.6. This was confirmed by both the numerical and

experimental results that indicate that the vertical stress was almost zero on the platform in internal regions not directly over piles. The arching effect identified "vaults" in the embankment with a very low rise, and not semi-circular as sometimes assumed.

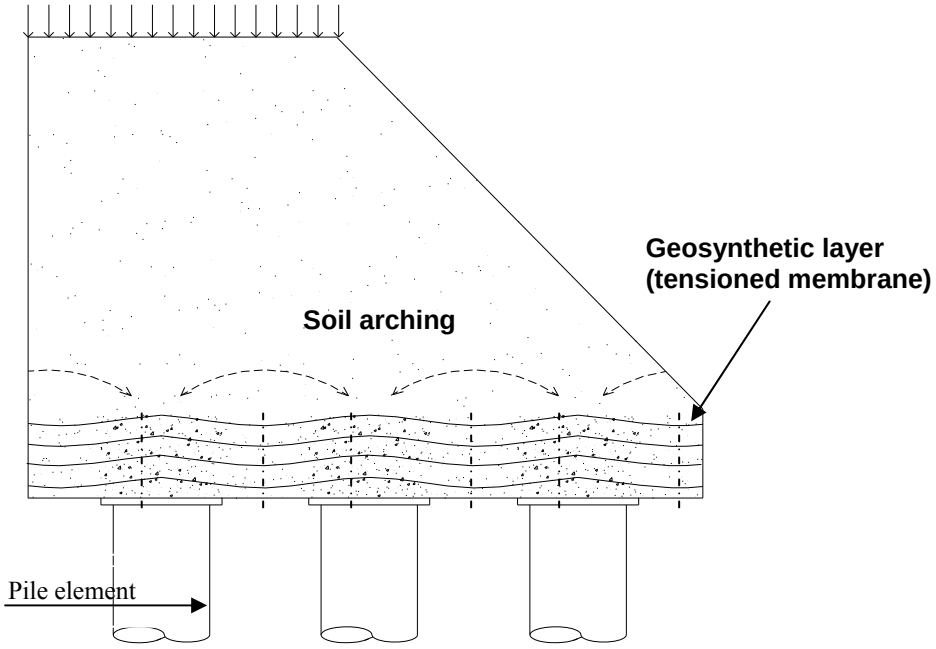

Figure 5.6. Schematic representation of the load transfer mechanism (not to scale).

A membrane effect of the geosynthetic reinforcement was clearly evident from the numerical results, but according to the model the design of the grid was more than sufficient. Indeed, the stresses and strains in the reinforcement were negligible within the model, especially those located at the lowest position in the platform. In particular, strains in the grid in the longitudinal direction of the embankment were almost zero, whereas in the transverse direction the numerical results gave maximum strains of about 10% of the strains experimentally observed (Fig. 5.7). It appears that geosynthetics in the bottom part of the embankment could reduce both problems at the base of slope, and make a significant contribution to the thrust associated with the arching effect.

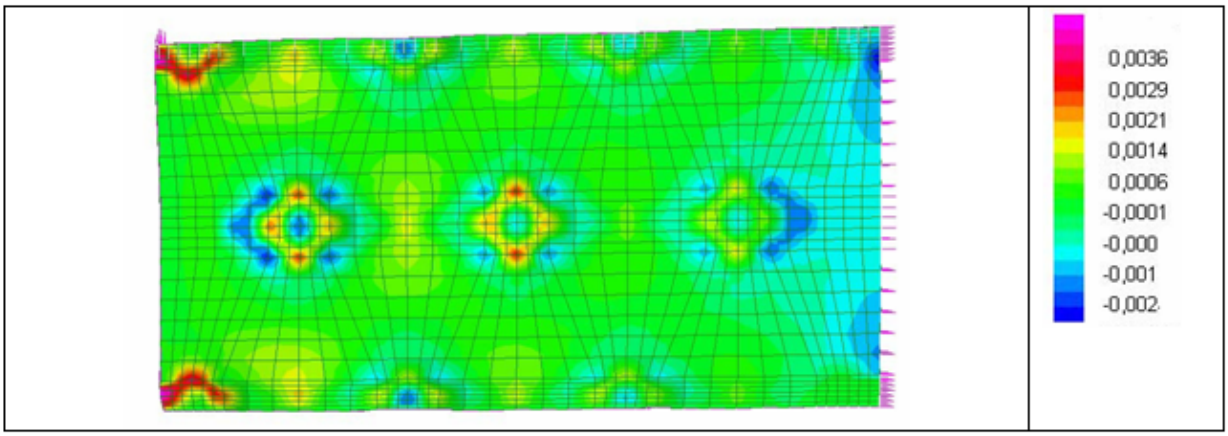

Figure 5.7. Strains in the transverse direction of the structure.

Chapter 6
Conclusions and Recommendations

Findings from the field instrumentation study and the finite element modeling (FEM) provide some insights into the behavior of the TH 241 pile-supported embankment, as well as pile-supported embankments in general. Some findings confirm design assumptions, while others suggest that different assumptions should be made about the embankment response. In general, however, the measurements indicate that the design is reasonable, confirmed by the absence of any observed differential settlement of the highway. In this chapter, major findings of the study are summarized, along with their implications for the design of future pile-supported embankments.

Piles

Axial strain measurements of the pipe piles and earth pressure cell (EPC) measurements at the base of the load transfer platform (LTP) indicate that the piles bear the entire embankment load, as assumed in the embankment design. However, it is important to note that one interpretation of the measurements is that that the load in the piles chosen for monitoring actually exceeds the load available from their tributary area. The FEM analysis also indicated that due to the geometry of the embankment, some piles bear a greater load than others.

Base of platform

Measurements from EPCs at the base of the LTP confirm that over the long term, there is little to no load in the areas between piles. However, readings during backfilling do indicate that the regions between piles register vertical stress of up to 5 psi (34.5 kPa) before gradually decreasing. The equivalent load from the 5 psi (34.5 kPa) stress exceeds the design assumptions for calculating the load supported by the geogrid. Because no strain readings were obtained from the lower geogrid layer (GL1), it is unknown how the loading during backfilling affected strain in the grid. The FEM analysis indicates that the lower layer plays a more important role in transferring the load, and therefore greater strain should be expected in GL1 than in the upper geogrid layer (GL3). Because of the ductility of the grid, the initial loading between piles before arching action develops and allows the embankment load to be transferred to the piles may not be critical.

Top of platform

Measurements of vertical stress at the top of the LTP showed that above the pile, stresses exceeded the theoretical vertical stress due to the overlying embankment fill, whereas between piles the long-term load was effectively zero. This finding was surprising, and indicates that the transfer of the embankment load is not confined to the LTP. Rather, it suggests that the embankment fill above the LTP plays a critical role in the load transfer, and is supported by results of the FEM study. For that reason, the assumption made in the design that arching occurs only within the LTP appears to be conservative for this embankment. The design could recognize

the importance of the embankment fill to the development of arching in the material above the LTP.

Strain in geogrid layer 3 (GL3), near the top of the LTP, appears to be within the limits of the design strain of 5%. EPC readings between piles at the top of the LTP indicate that the maximum vertical stress between piles reached during backfilling is lower compared to vertical stress at the base of the LTP, around 2 psi (14 kPa). Because strain readings were within design limits it is probably not necessary to account for loading during backfilling at the top of the LTP.

Other comments

A review of the design method indicated that the method used to calculate the volume of material supported by the geogrid is not consistent with the design assumptions. The actual shape associated with the design assumption that arching occurs at 45 degrees from the pile cap is not a pyramid, but a result of the intersection of three semi-conical sections radiating from the edge of the pile cap. Because the actual shape is too complex for simple design calculations, a pyramid may be an acceptable approximation. However, it is recommended that the center to center pile spacing *s* be used to calculate the length of the pyramid base rather than the distance between pile cap edges *s-d.*

References

Bell, A.L., Jenner, C., Maddison, J.D., and Vignoles, J. (1994). Embankment support using geogrids with Vibro Concrete Columns. *Proceedings, 5th International Conference on Geotextiles, Geomembranes, and Related Products,* Singapore, 335-338.

Collin, J.G. (2004). Column Supported Embankment Design Considerations. *Proceedings of the 52nd Annual Geotechnical Engineering Conference*, University of Minnesota, Minneapolis, MN, ed. J.F. Labuz and J.G. Bentler, 51-78.

Fluet, J.E., Christopher, B.R., and Slaters, A.R. (1986). Geosynthetic stress-strain response under embankment loading conditions. *Proceedings, 3rd International Conference on Geotextiles, Geomembranes, and Related Products*, Vienna, Austria, 175-180.

Gartung, E., Verspohl, J., and Alexiew, D. (1996). Performance of a Geogrid Reinforced Railway Embankment of Piles. *Proceedings, 14th International Conference on Soil Mechanics and Foundation Engineering,* Hamburg, Germany, Vol. 3, 1731-1736.

Guido, V.A., Knueppel, J.D., and Sweeny, M.A. (1987). Plate Loading Tests on Geogrid-Reinforced Earth Slabs. *Proceedings*, *87th Geosynthetic Conference*, New Orleans, LA, 216-225.

Han, J., and Gabr, M.A. (2002). Numerical Analysis of Geosynthetic-Reinfoced and Pile-Supported Earth Platforms over Soft Soil. *Journal of Geotechnical and Geoenvironmental Engineering*, Vol. 128, No. 1, 44-53.

Hewlett, W.J., and Randolph, M.F. (1988) Analysis of piled embankments. *Ground Engineering*, Vol. 21, No. 3, 12-18.

Jenner, C.G., Austin, R.A., and Buckland, D. (1998). Embankment support piling over piles using geogrids. *Proceeding, 6th International Conference on Geotextiles, Geomembranes, and Related Products,* Atlanta, GA, 763-766.

Jones, C.J.F.P., Lawson, C.R., and Ayres, D.J. (1990). Geotextile reinforced piled embankments. *Proceedings, 4th International Conference on Geotextiles, Geomembranes, and Related Products*, Balkema, Netherlands, 155-160.

Labuz, J.F., and Theroux, B. (2005). Laboratory Calibration of Earth Pressure Cells. *Geotechnical Testing Journal,* Vol. 28, No. 2, 188-196.

Love, J., and Milligan, G. (2003). Design methods for basally reinforced pile-supported embankments over soft ground. *Ground Engineering*, March, 39-43.

Low, B.K., Tang, S.K., and Choa, V. (1994). Arching in piled embankments. *Journal of Geotechnical Engineering*, Vol. 120, No. 11, 1917-1938.

Maddison, J.D., Jones, D.B., Bell A.L., and Jenner, C.G. (1996). Design and performance of an embankment supported using low strength geogrids and vibro concrete columns. *Proceedings, 1st European Geosynthetics Conference,* Maastricht, Netherlands, 325-332.

Marston, A., and Anderson, A.O. (1913). *The Theory of Loads on Pipes in Ditches and Test of Dement and Clay Drain Tile and Sewer Pipe*. Bulletin 31, Iowa Engineering Experiment Station, Ames, Iowa, U.S.A.

Plomteux, C.C., Porbaha, A. , and Spaulding,C. (2004). CMC foundation system for embankment support – A case history. *Proceedings, Geotechnical Geosupport Conference 2004,* Orlando, FL, No. 124, 980-992.

Rathmayer, H. (1975). Piled embankment supported by single pile caps. *Proceedings, Conference on Soil Mechanics and Foundation Engineering,* Istanbul, Turkey, Vol. 1, 283-290.

Reid, W.M., and Buchanan, N.W. (1984). Bridge approach support piling. *Piling and Ground Treatment*, Thomas Telford Ltd., London, England, 267-274.

Russell, D., and Pierpoint, N. (1997). An assessment of design methods for piled embankments. *Ground Engineering*, November, Vol. 30, No. 11, 39-44.

Stewart, M.E., Navin, M.P., and Filz,G.M.(2004). Analysis of a column-supported test embankment at the I-95/Route 1 interchange *Geotechnical engineering for transportation projects: Proceedings of Geo-Trans 2004,* Los Angeles, CA, 1337-1364.

Stewart, M.E., and Filz, G.M. (2005). Influence of Clay Compressibility on Geosynthetic Loads in Bridging Layers for Column-Supported Embankments. *Proceedings, Geo-Frontiers 2005 Conference,* Austin, TX.

Topolnicki, M. (1996). Case history of a geogrid-reinforced embankment supported on vibro concrete columns. *Proceedings, 1st European Geosynthetics Conference,* Maastricht, Netherlands, 333-342.

Warren, K.A., Brooks, J.A., and Howard, I.L. (2005). Survivability of Foil Strain Gages Mounted on Geosynthetics Under Full-Scale Construction Loads. *Proceedings, Geo-Frontiers Conference 2005,* Austin, TX, 4085-4090.

Vega-Meyer, R., and Shao, Y. (2005). Geogrid-reinforced and pile-supported roadway embankment. *Geotechnical Special Publication,* No. 131, 461-473.

Van Eekelen, S.J.M., Bezuijen, A., and Oung, O. (2003). Arching in piled embankments; experiments and design calculations. *Proceedings, Foundations: Innovations, observations, design and practice,* Dundee, Scotland, 885-894.

Appendix A

Earth Pressure Cell (EPC) Calibrations

A.1 Soil calibrations

The reasons for performing calibrations of EPCs in soil are described in detail in Labuz and Theroux (2005). In summary, while manufacturer sensitivities are provided with the sensor, they are performed with fluid pressure and do not take into account the fact that the normal stress distribution that develops on the face(s) of an EPC in a soil mass is typically non-uniform due to inclusion and/or arching effects. Such distributions can lead to over-registration or under-registration of earth pressure, depending on the type of EPC and the soil characteristics. A sensitivity obtained by relating the EPC output to known earth pressure in a controlled soil environment provides a more accurate prediction of how the EPC will perform in field conditions.

In the calibration, the EPC is placed in a layer of sand between two flat water bladders in a cylindrical drum. Layers of sand are placed below the lower bladder and above the upper bladder as a buffer. A load is applied to the setup via a series of platens above the top sand layer, and fluid pressures in the bladders as well as the EPC output are recorded. Figure A.1 shows a schematic of the calibration apparatus. The bladders are meant to provide a uniform vertical stress equal to the fluid pressure, which is then related to the EPC output to find the sensitivity.

In these test, the soil used was a coarsely-graded sand. The sand layer in which the EPC was placed consisted of 60 kg of sand, divided evenly above and below the sensor. Both halves of the layer were compacted by delivering about 15 blows to it via a platen, such that the sand reached a relative density of 65-85%.

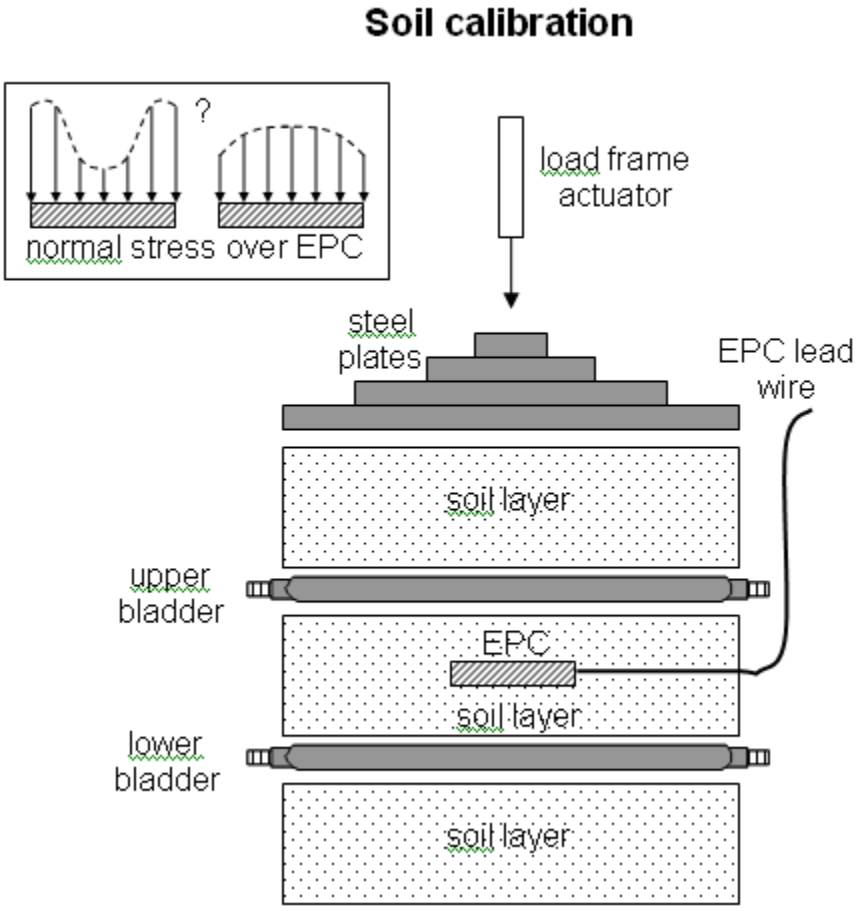

Figure A.1. Schematic showing the components of the calibration apparatus. The soil layers and bladders are contained by a steel drum.

The EPCs used in the study all had the same geometry, as described in section 3.3.2, and varied only by the type of sensing element measuring the internal fluid pressure. Half of the sensors utilized a vibrating wire (VW) pressure transducer, while the other half utilized a semiconductor-based transducer. As discussed above, arching and inclusion effects that lead to a different sensitivity for soil depend on the transducer structure and/or sensing mechanism, as well as the soil characteristics. The same soil was used for all calibrations and care was taken to ensure similar densities in each calibration, so possible differences in the soil characteristics among the calibrations were not expected. Therefore, it was anticipated that all EPCs would exhibit the same response to soil loading. In other words, it was expected that all EPCs would over- or under-register earth pressure by roughly the same magnitude. However, it was noted during the calibration of the vibrating wire EPCs that some of the sensors appeared to over-register earth pressure while others appeared to under-register earth pressure. The resulting sensitivities are shown in Table A.1. The magnitude of the resulting over- or under-registration was often significant (compare +15% for VW 4206 to -32% for VW 4209). These results raised doubts about the whether the use of the manufacturer-provided (MFR) sensitivities as fluid sensitivities for the EPC was appropriate.

Table A.1. A comparison of sensitivities provided by the manufacturer (MFR) and as determined with soil calibrations. The ratio of soil to MFR sensitivity should indicate earth pressure registration for the EPC and the particular soil in which it was calibrated.

sensor	MFR (digits/psi)	soil (mean) (digits/psi)	soil/ MFR	percent over/under-registration
VW 4203	-142.6	-149.7	1.050	5.0
VW 4204	-148.9	-168.9	1.134	13
VW 4206	-148.2	-170.2	1.149	15
VW 4208	-150.6	-162.5	1.079	7.0
VW 4209	-144.4	-98.5	0.682	- 32
VW 4210	-148.0	-131.0	0.886	-11

In order to check whether the MFR sensitivities accurately represented fluid sensitivities for the EPCs, a setup was arranged with the soil calibration apparatus that allowed the laboratory determination of fluid sensitivities. The EPCs were placed directly between the two bladders, as shown in Fig A.2, and the same loading procedure used in the soil calibration was followed. It was assumed that the direct contact between the EPC face and the bladders would provide a uniform vertical stress distribution across the face, thus eliminating any arching or inclusion effects. Resulting fluid sensitivities can be found in Table A.2. The soil sensitivities, when compared to the laboratory-determined fluid sensitivities, show a much more consistent result: all EPCs over-register earth pressure by about 19 percent. All calibration plots can be found in Appendix B.

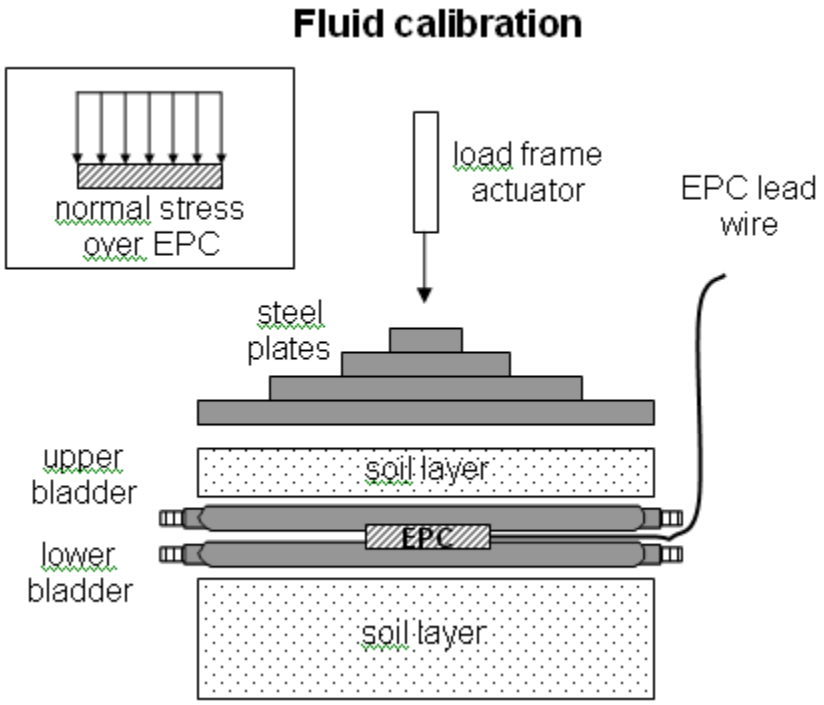

Figure A.2. Schematic showing the modified apparatus used to perform fluid calibrations. The bladders make direct contact with the EPC, providing a uniform normal stress distribution over the EPC.

Table A.2. Summary of laboratory-determined fluid sensitivities for vibrating wire EPCs, comparing them to soil sensitivities. The results show that the EPCs consistently over-register earth pressure by an average of 19 percent.

sensor	fluid (digits/psi)	soil (mean) (digits/psi)	soil / fluid	percent over/under-registration
VW 4203	-124.7	-149.8	1.20	20
VW 4204	-142.5	-168.9	1.19	19
VW 4206	-145.1	-170.3	1.17	17
VW 4208	-134.4	-162.5	1.21	21
VW 4209	-85.5	-98.5	1.15	15
VW 4210	-109.1	-131.1	1.20	20

Fluid calibrations were also performed for the semiconductor-based EPCs. In contrast with the vibrating wire EPCs, however, the resulting fluid sensitivities were nearly identical to the MFR sensitivities (Table A.3). Also, the soil sensitivities for these sensors were greater than the fluid sensitivities, again indicating an over-registration of earth pressure of slightly less that 20%.

(Note: There is no obvious explanation for the contrast in the MFR calibrations between the VW and semiconductor EPCs. It is possible that the MFR sensitivities were determined with solely the pressure transducer rather than the entire EPC device.)

Table A.3. Summary of manufacturer-provided (MFR) sensitivities and fluid and soil sensitivities as determined from laboratory calibrations for semi-conductor EPCs. In this case MFR sensitivities matched very well with laboratory-determined fluid sensitivities. This set of EPCs over-registers earth pressure by an average of 17 percent.

sensor	MFR (mV/psi)	fluid (mV/psi)	soil (mean) (mV/psi)	fluid/ MFR	soil / fluid	percent over/under-registration
SC 10052	4.31	4.27	4.93	0.991	1.15	15
SC 10053	4.31	4.30	5.06	0.998	1.18	18
SC 10054	4.31	4.34	5.11	1.007	1.18	18
SC 10055	4.31	4.29	5.05	0.995	1.18	18
SC 10056	4.31	4.27	5.00	0.991	1.17	17
SC 10057	4.31	4.31	5.01	1.000	1.16	16

A.2 Additional study on the effect of non-uniform loading of an EPC

Several experiments were carried out on the Geokon EPCs in order to investigate the effect of loading area and loading distribution on the EPC output. Recall that the EPC consists of two steel faces surrounding a fluid-filled chamber, which responds to external loading on the faces with an internal fluid pressure. Cutting the EPC sideways through the chamber and considering static equilibrium of a single face (Fig. A.3), there are three loads to be considered: (1) The load F_{ext} acting on the outside of the face (assumed to be uniformly distributed pressure p_{ext}), (2) the

load F_{int} due to the fluid pressure p_{int} acting on the inside of the face, and (3) the load at the edge F_{edge}, where the two faces are attached (shown in the diagram as line load f_{edge} distributed over the circumference of the EPC).

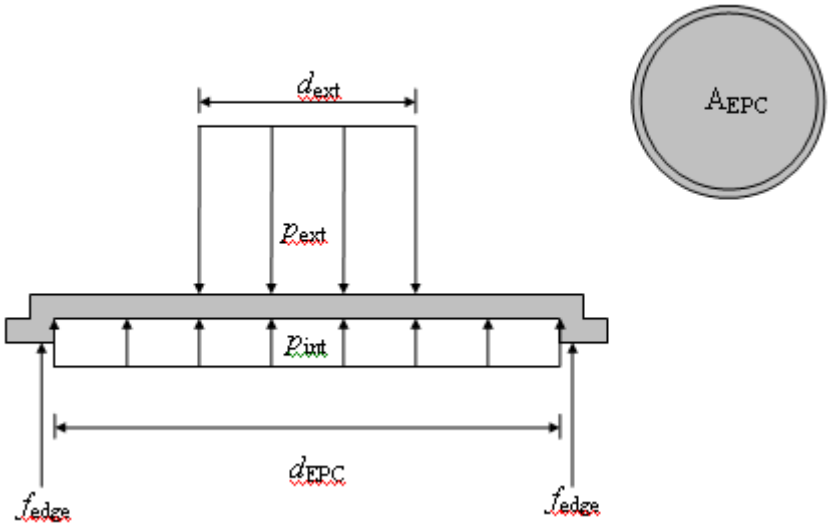

Figure A.3. A cross-section through the center of an EPC showing internal pressure p_{int}, external pressure p_{ext}, and line load f_{edge} distributed over the EPC edge.

One possible way of looking at the system is to consider the EPC face as a simply-supported membrane. Assuming no loading on the edge of the face, this requires that the edge load $F_{edge} = 0$, as a membrane provides no bending stiffness by which to transfer the load to the edge. Therefore, the internal load F_{int} due to the pressure generated in the chamber p_{int} must be equal to the external load on the EPC face F_{ext}, regardless of the load distribution and the area over which the load is applied. The result is that if F_{ext} is applied across the same area as the internal pressure p_{int} ($d_{ext} = d_{EPC}$), the internal pressure can be considered a measure of the average external pressure. This is the assumption typically made in the interpretation of EPC output.

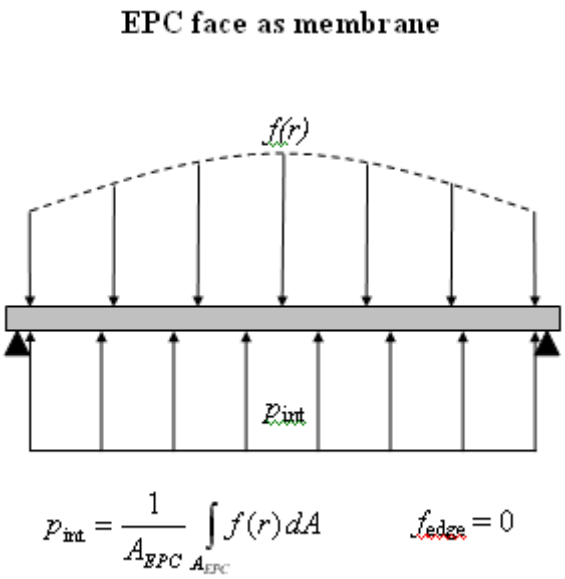

Figure A.4. Diagram showing how, assuming the EPC face acts as a membrane, a measurement of p_{int} gives an average of the non-uniformly distributed f(r).

The EPC face is in reality constructed of stainless steel, and thus modeling it as a membrane may not be appropriate. Considering the system as a circular plate with bending stiffness introduces the potential for the transfer of load to the edges. Various textbooks contain solutions for deflections of circular plates subjected to uniform loading. Assuming that the hydraulic fluid in the chamber is virtually incompressible, which is true at the relatively low pressures measured with EPCs, the volume in the chamber should remain constant. The internal pressure p_{int} required to satisfy this condition can be calculated by superposing the deflection due to loading on each side of a face, such that the volume displaced by loading on the outside of the face V_{ext} must be equal to the volume displaced by the loading on the inside V_{int}. Knowing the external load F_{ext}, the internal pressure p_{int} can be calculated by equating the expressions for V_{ext} and V_{int} and solving for p_{int}. The resulting expression for p_{int} is a function of elastic modulus, Poisson's ratio, plate diameter, and diameter of the area over which p_{ext} is applied. The support load can be found from equilibrium as the difference between F_{ext} and the internal load F_{int}.

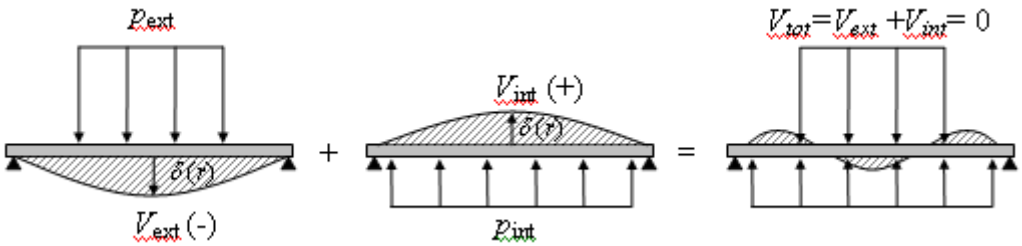

Figure A.5. Diagram showing how, knowing p_{ext} and assuming $V_{ext} + V_{int} = 0$, superposition can be used to determine p_{int}.

For the laboratory tests, a known load F_{ext} was applied to both EPC faces via platens of identical size. A rubber pad was placed between the platen and the EPC face to protect the steel face and so that the loading would be more uniform. Sensor output was recorded and converted to pressure p_{int}. The same procedure was carried out at F_{ext} for platens of varying size. Each load diameter has a distinct sensitivity. Figure A.7 shows a plot of EPC output versus the loading diameter for a particular load. Both plots show that greater internal pressure was measured when F_{ext} was applied over a smaller area. Figure A.7 also shows the solutions calculated using superposition as described above for fixed and simply supported edges. It indicates that the experimental data match the general trend of the solutions. The difference between the experimental and analytical results could be explained by the lack of a uniform distribution of F_{ext}. Ideally, the external load would be applied with a fluid to ensure uniformity. However, the development of such an apparatus was beyond the scope of this investigation. It is likely that the load distributed by the rubber pad was non-uniform and concentrated at the edge of the pad.

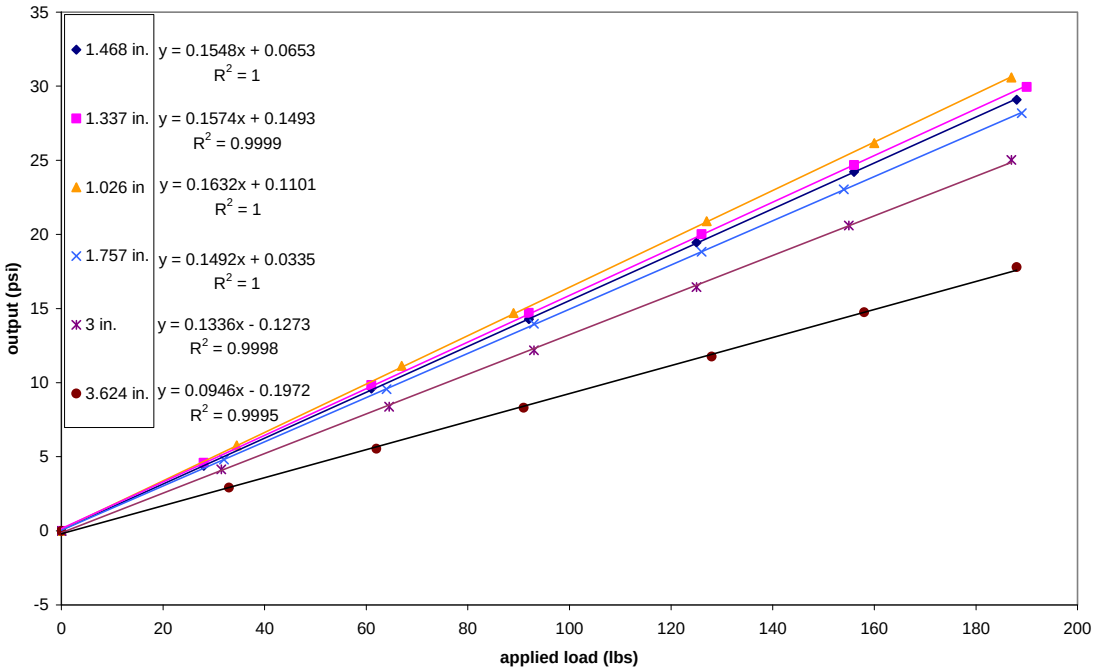

Figure A.6. A plot of test data for loading of an EPC with different sized platens.

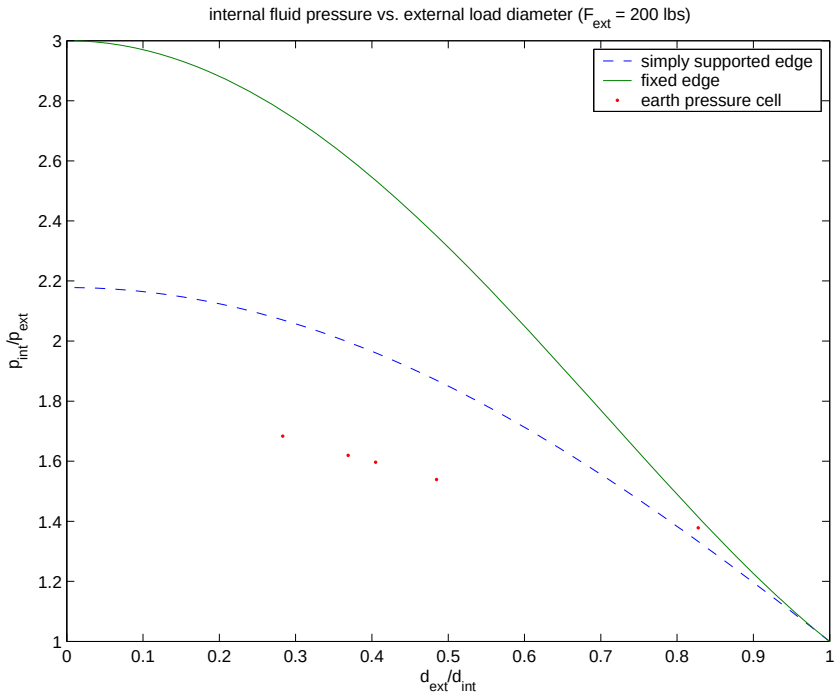

Figure A.7. A plot showing data from loading tests compared to solutions for circular plates. EPC data for the load chosen was extrapolated from the best fit lines.

A.3 Calibration of settlement system

A small test was performed in order to determine the sensitivity and resolution of the settlement systems. A reservoir was fixed to a countertop, about 3 ft (1 m) above the floor. The pressure transducer, attached to the settlement plate, was placed on an adjustable platform resting about 8 in. (20 cm) above the floor. The height of the settlement plate was increased in 1 or 2 mm increments. At each increment the vibrating wire output was recorded. The results are shown in Fig. A.9. The resulting sensitivity was 0.540 digits/mm, compared to the MFR sensitivity of 0.527 digits/mm, a difference of 2.3%. One major difference between the two calibrations is that the factory calibration was performed over a much larger range, about 6 ft (1.83 m). Since calibration data is typically best described as a curve, rather than a line, it is reasonable that the full-range sensitivity would vary from the sensitivity determined at the lower end of the transducer's range.

The settlement system demonstrated a very good resolution. With a range of about 23 ft (7.5 m), it was possible to measure 1 mm increments very accurately. Using the linear fit, the predicted height varies from the measured data no more than 0.25 mm. This is more than enough accuracy for geotechnical measurements. It is important to note, however, that the calibration did not take into account effects due to temperature or other factors.

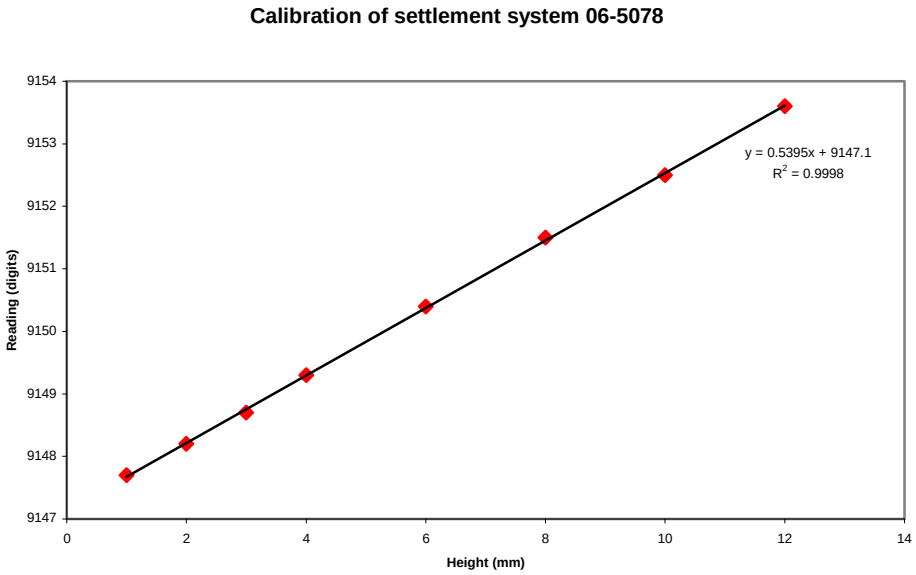

Figure A.8. Calibration of a settlement system.

Appendix B

Earth Pressure Cell (EPC) Calibration Results

Notes:

- Each calibration consists of two loading cycles. The best fit line is taken from the final unloading cycle.

- Two separate soil calibrations were performed for each EPC. That is, the soil and upper bladder were removed and replaced after the first calibration to account for variation in the soil characteristics resulting from the placement procedure. Correspondingly, there are two soil calibration plots for each EPC.

- Vibrating wire output is given in terms of the square of the resonant frequency of the wire. Note that output decreases with increasing pressure, as the pressure decreases the tension in the wire.

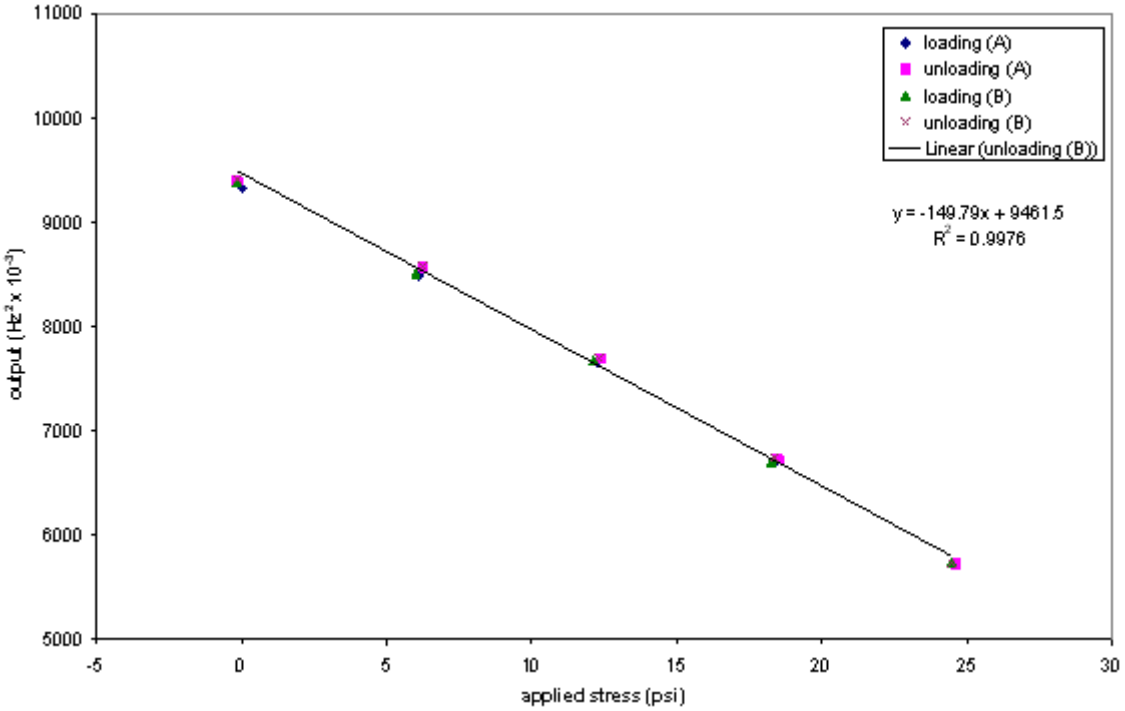

Figure B.1. Soil Calibration 1 for EPC 4203.

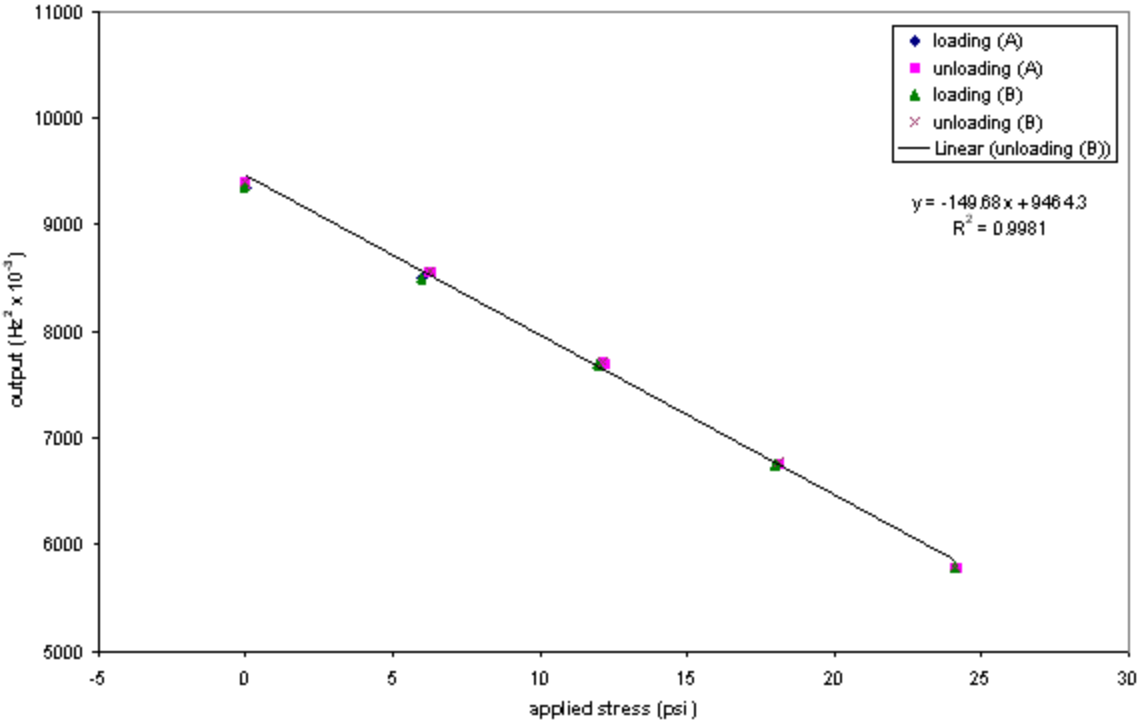

Figure B.2. Soil Calibration 2 for EPC 4203.

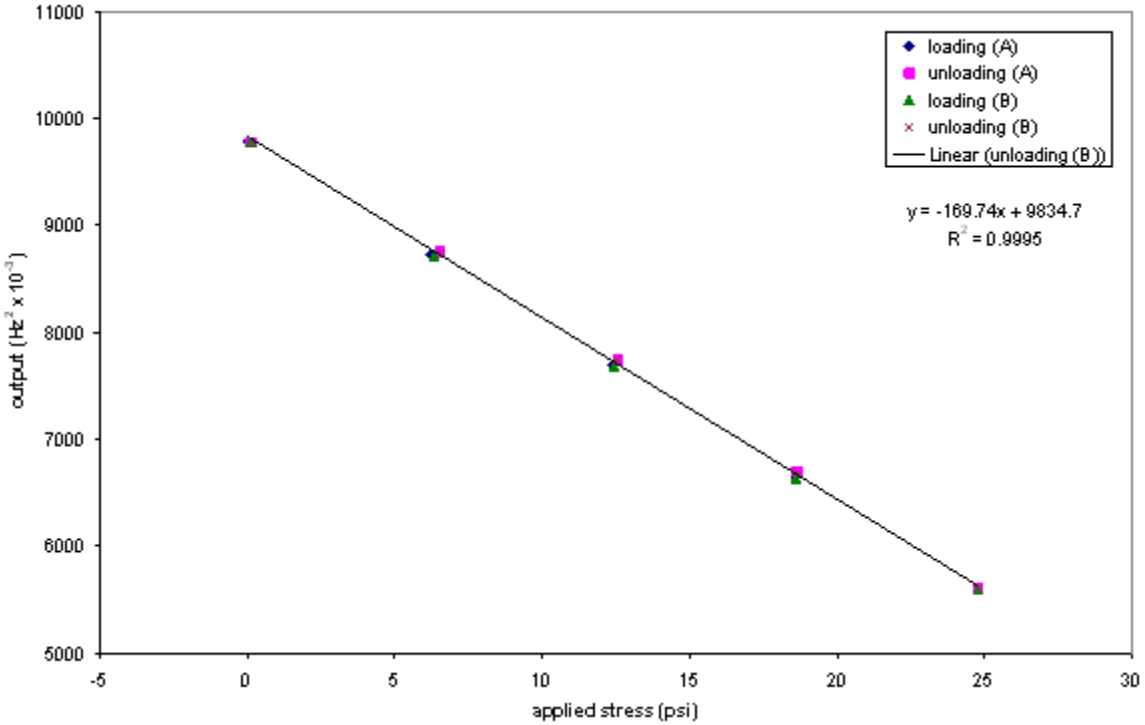

Figure B.3. Soil Calibration 1 for EPC 4204.

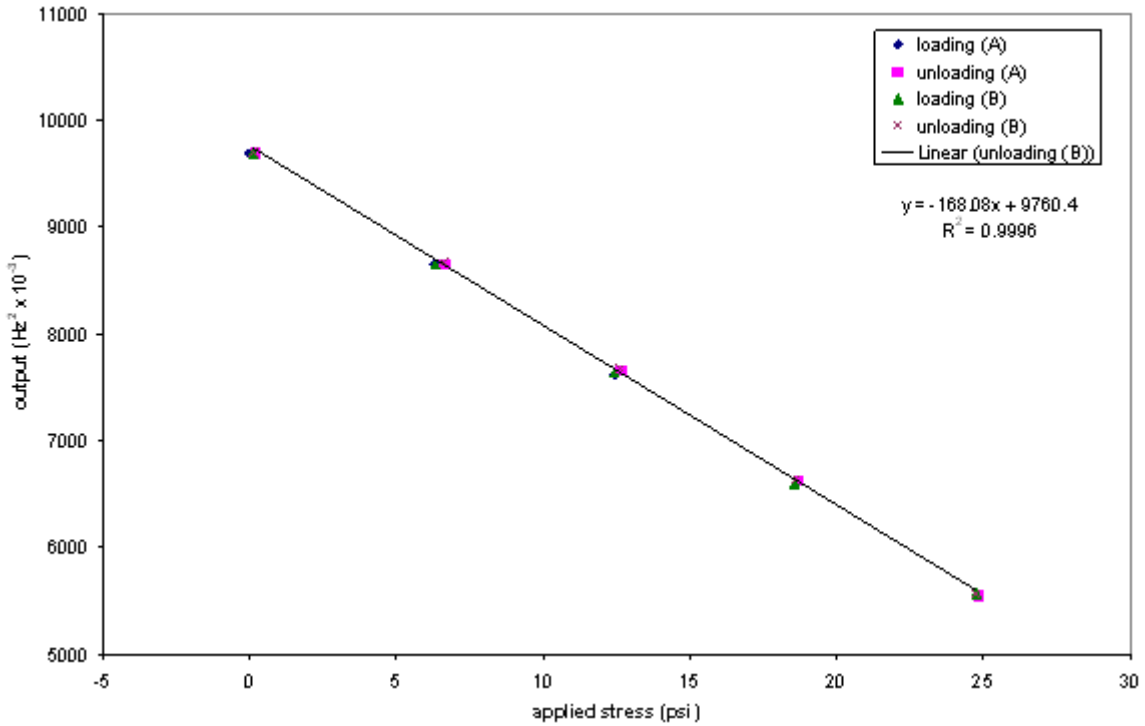

Figure B.4. Soil Calibration 2 for EPC 4204.

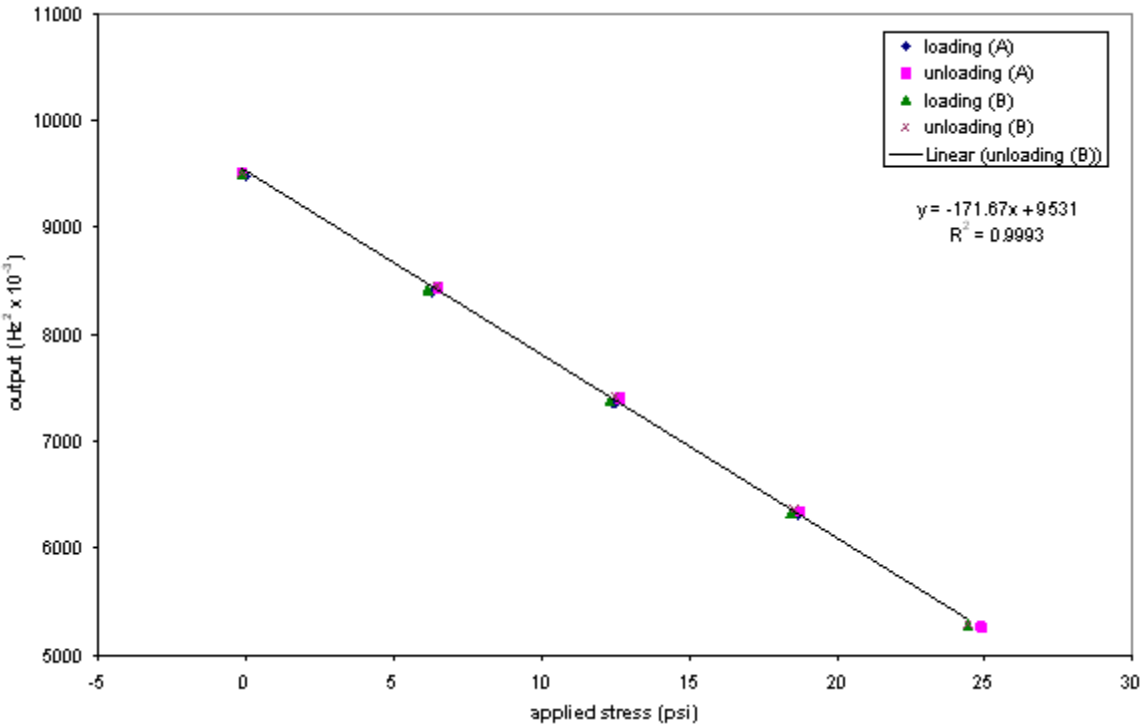

Figure B.5. Soil Calibration 1 for EPC 4206.

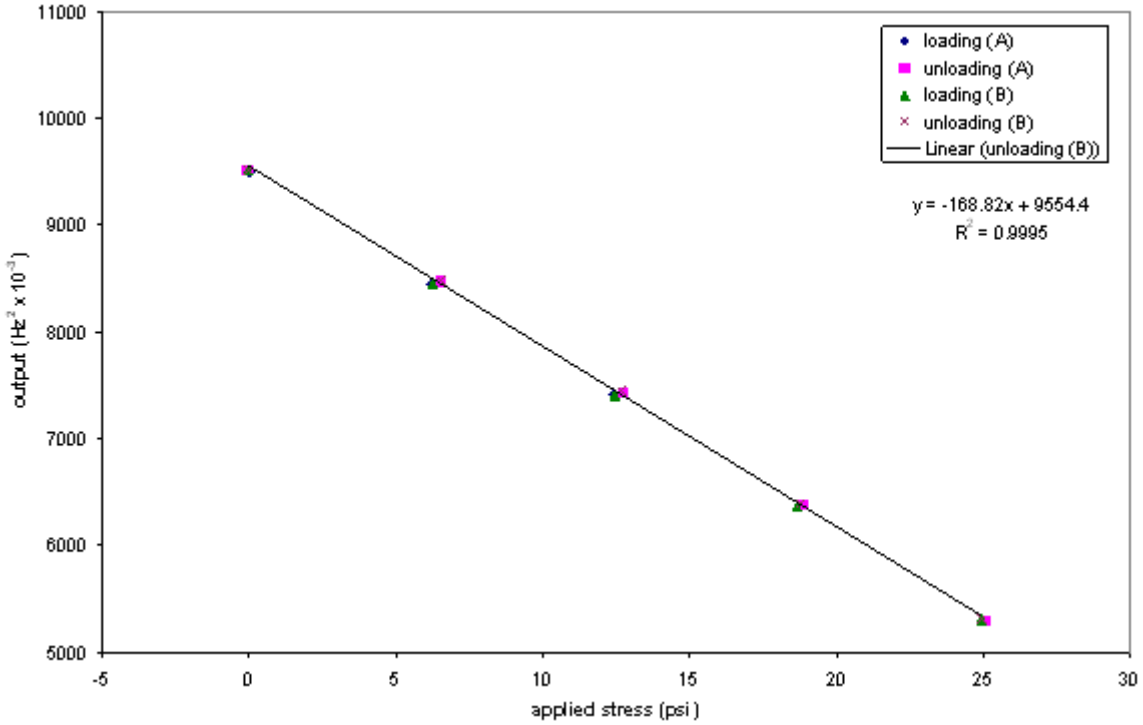

Figure B.6. Soil Calibration 2 for EPC 4206.

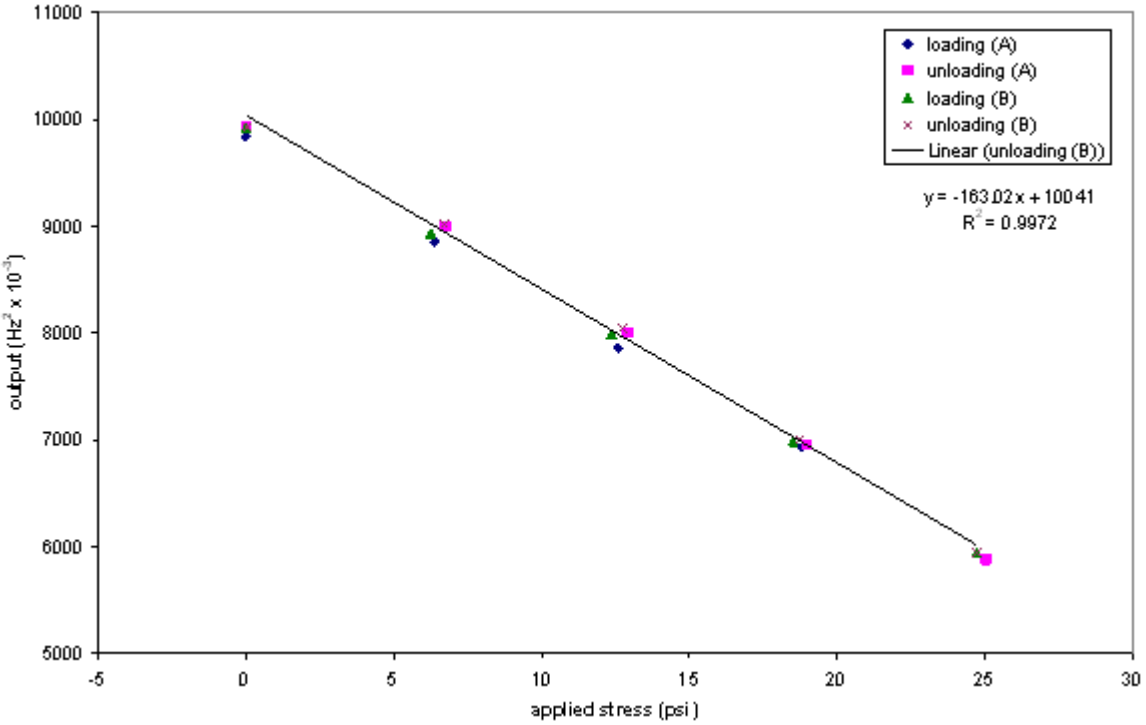

Figure B.7. Soil Calibration 1 for EPC 4208.

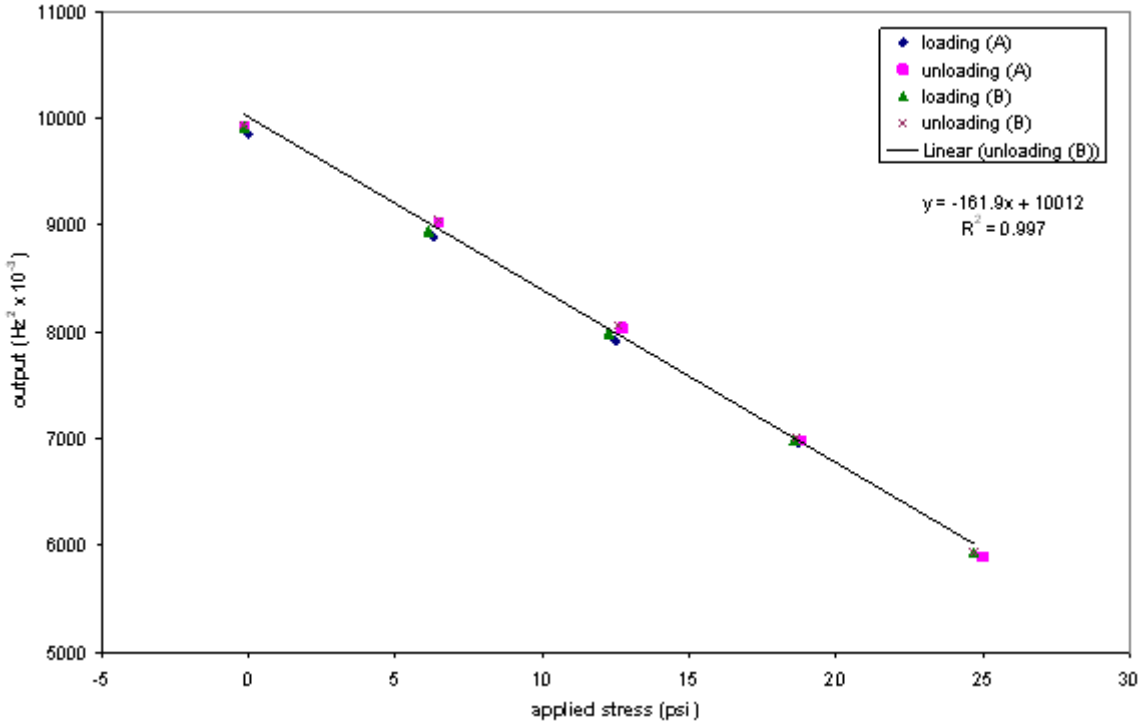

Figure B.8. Soil Calibration 2 for EPC 4208.

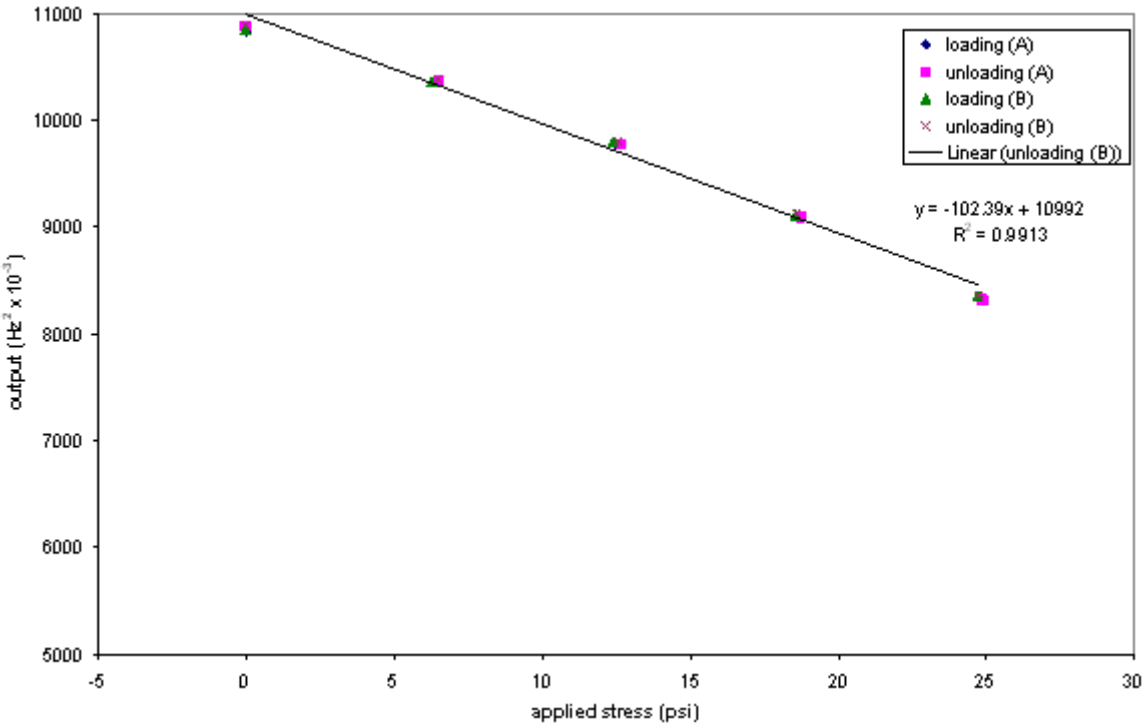

Figure B.9. Soil Calibration 1 for EPC 4209.

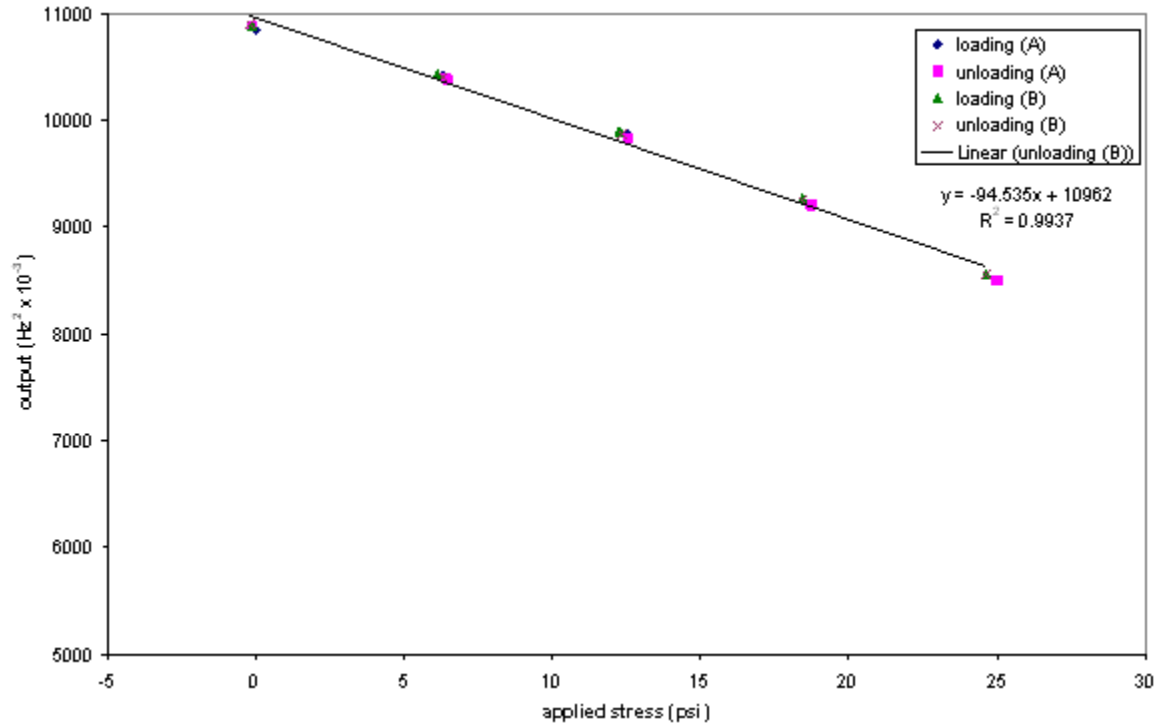

Figure B.10. Soil Calibration 2 for EPC 4209.

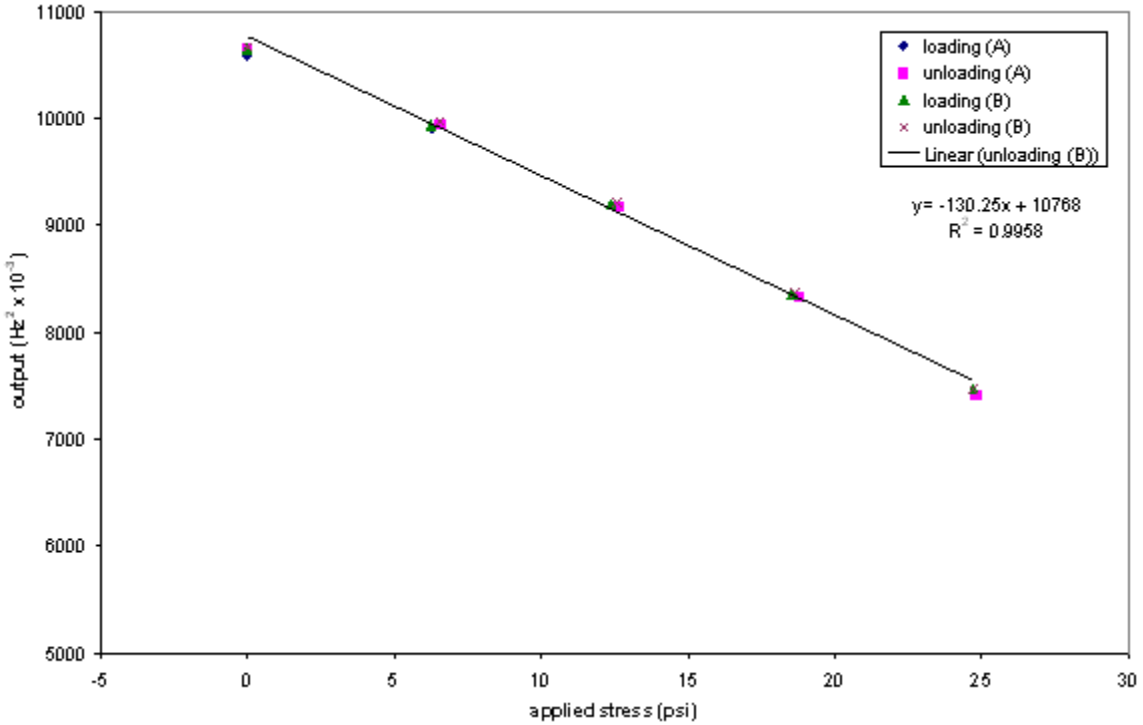

Figure B.11. Soil Calibration 1 for EPC 4210.

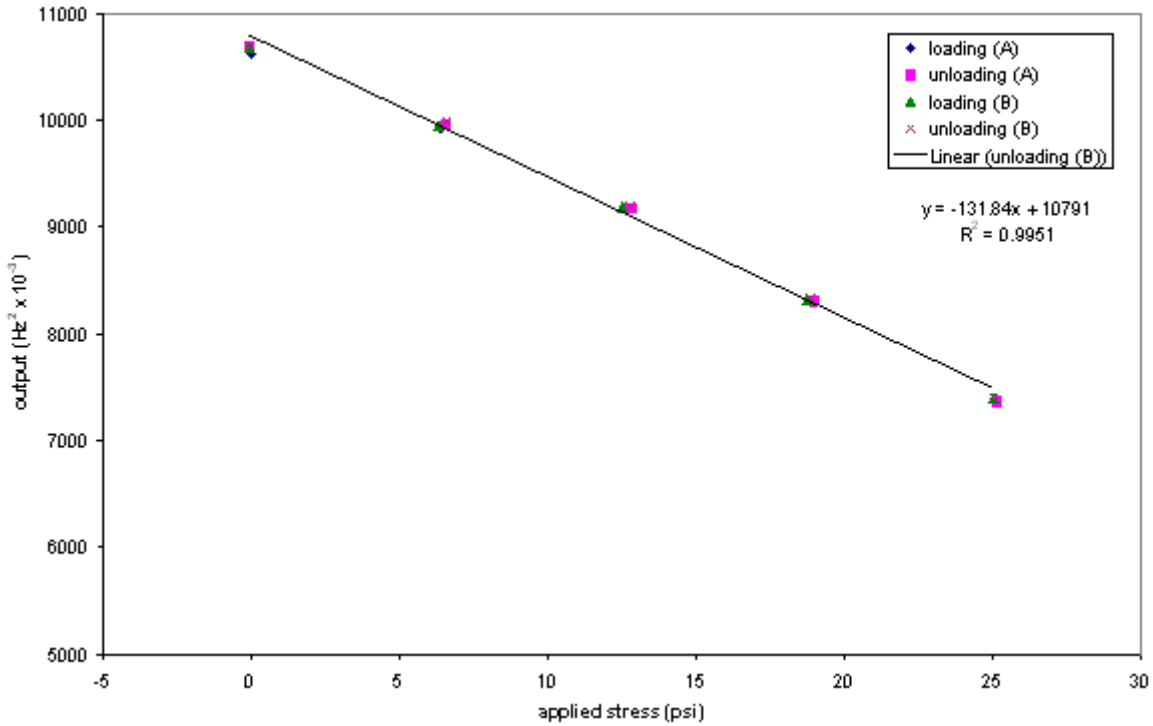

Figure B.12. Soil Calibration 2 for EPC 4210.

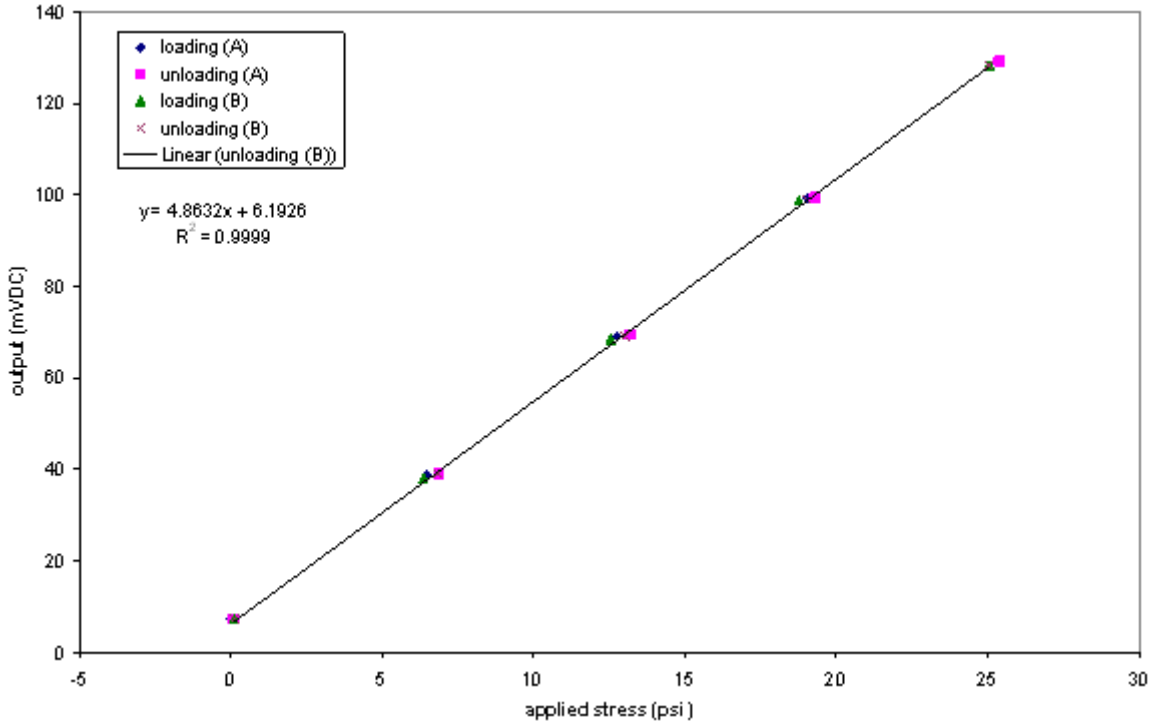

Figure B.13. Soil Calibration 1 for EPC 10052.

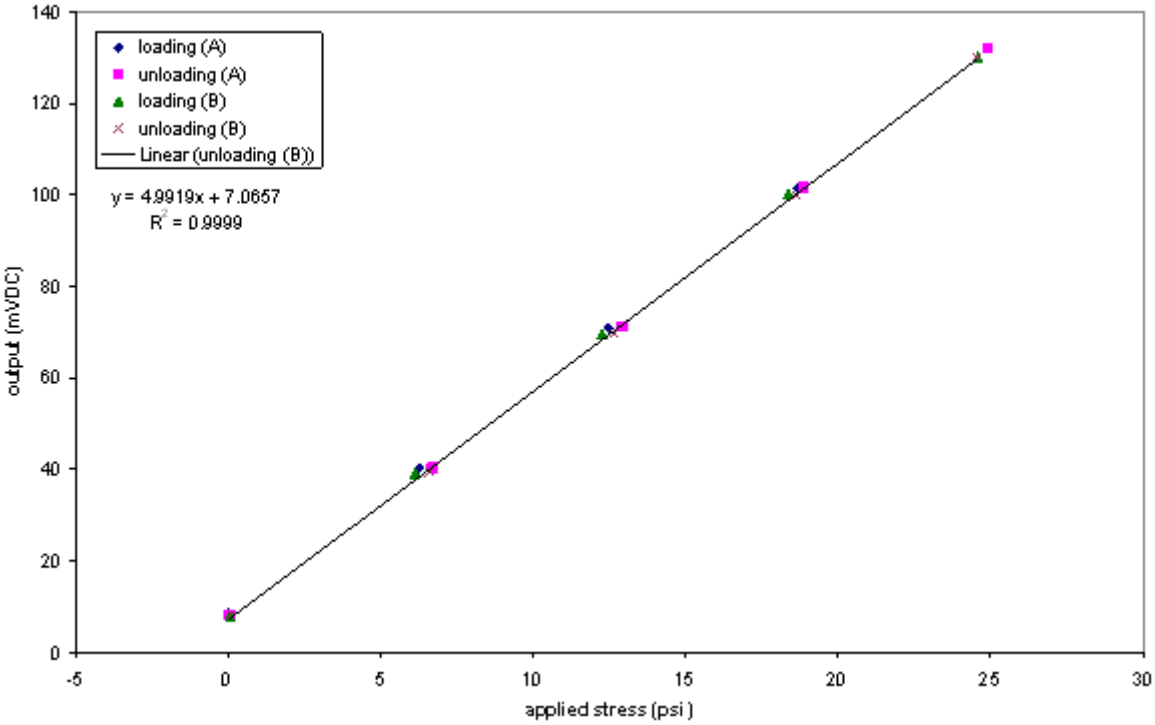

Figure B.14. Soil Calibration 2 for EPC 10052.

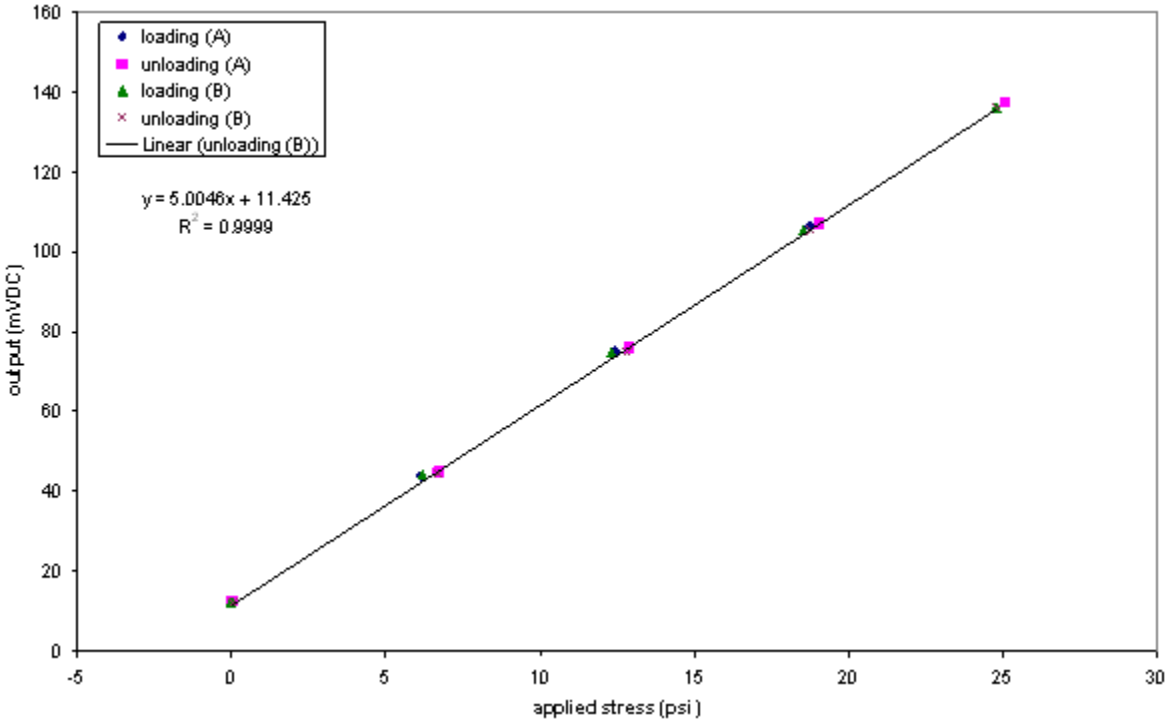

Figure B.15. Soil Calibration 1 for EPC 10053.

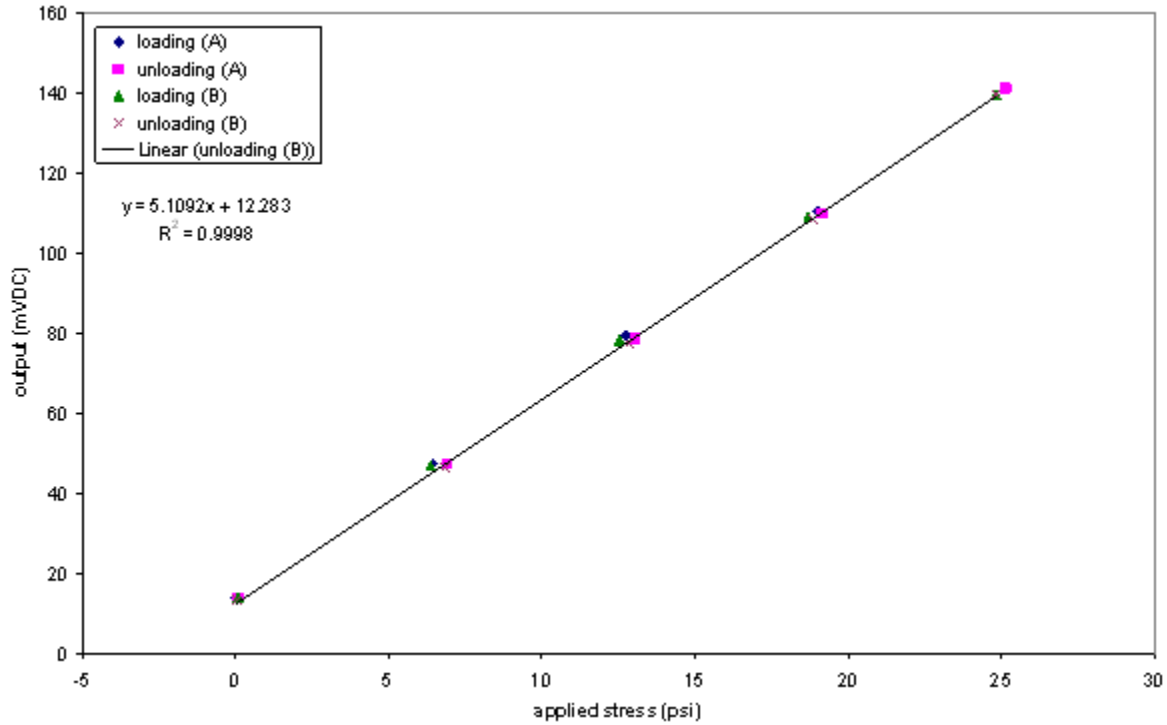

Figure B.16. Soil Calibration 2 for EPC 10053.

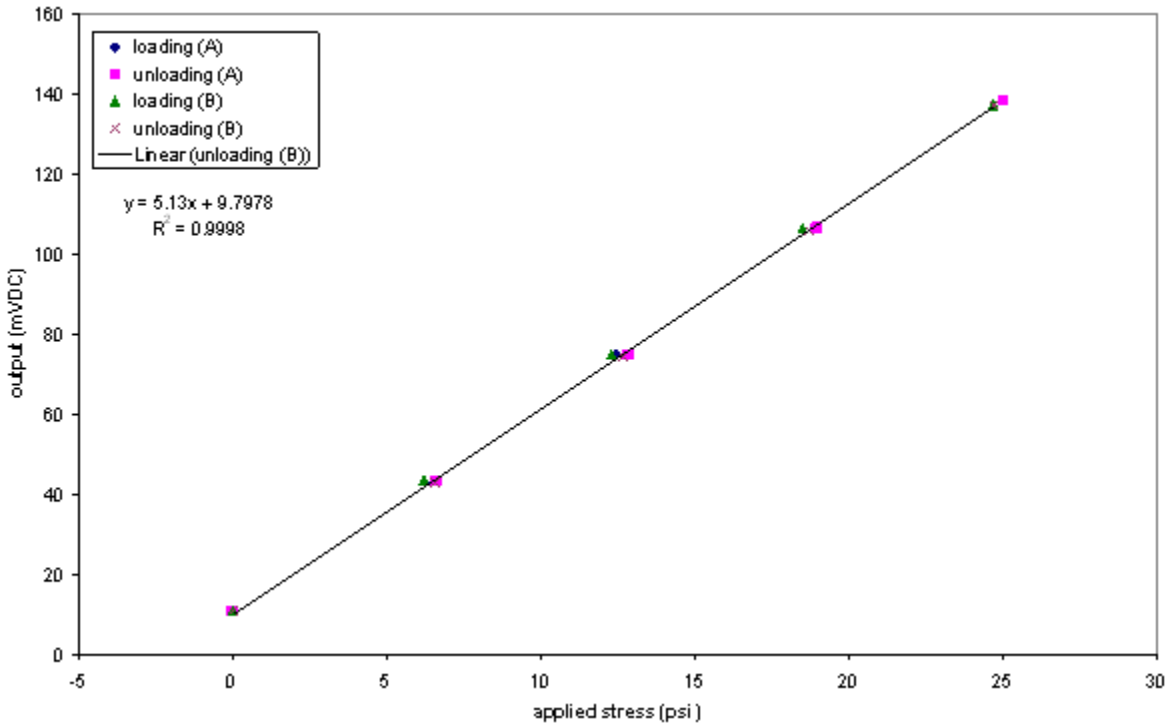

Figure B.17. Soil Calibration 1 for EPC 10054.

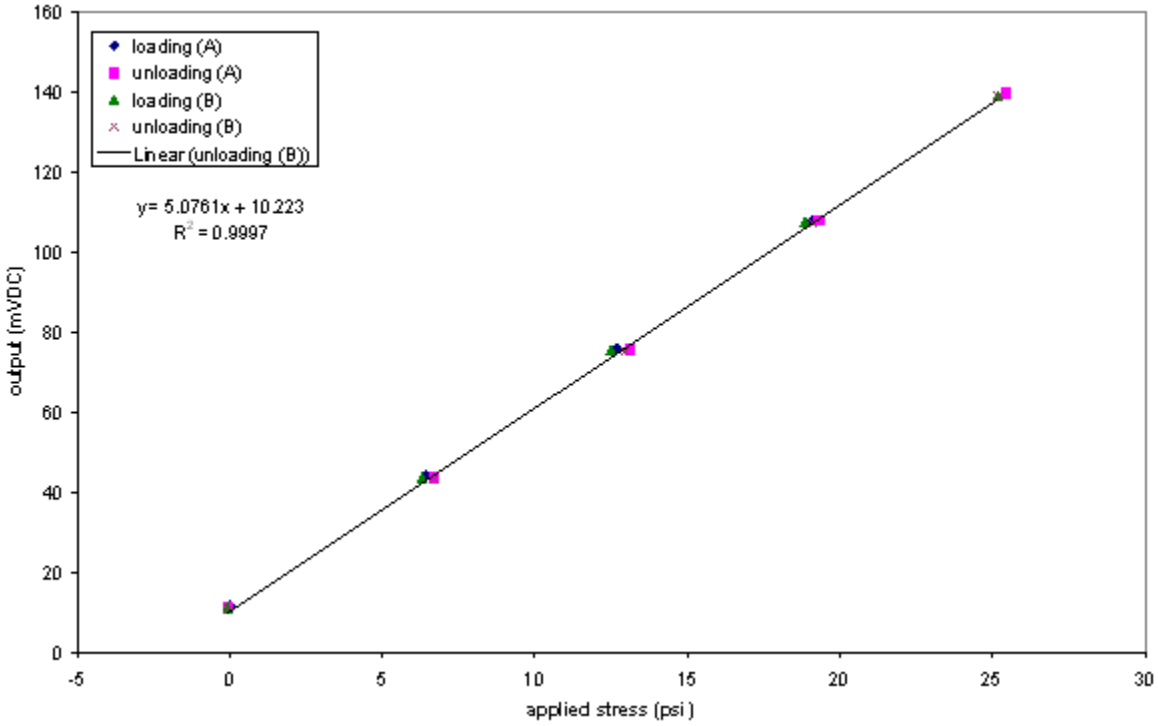

Figure B.18. Soil Calibration 2 for EPC 10054.

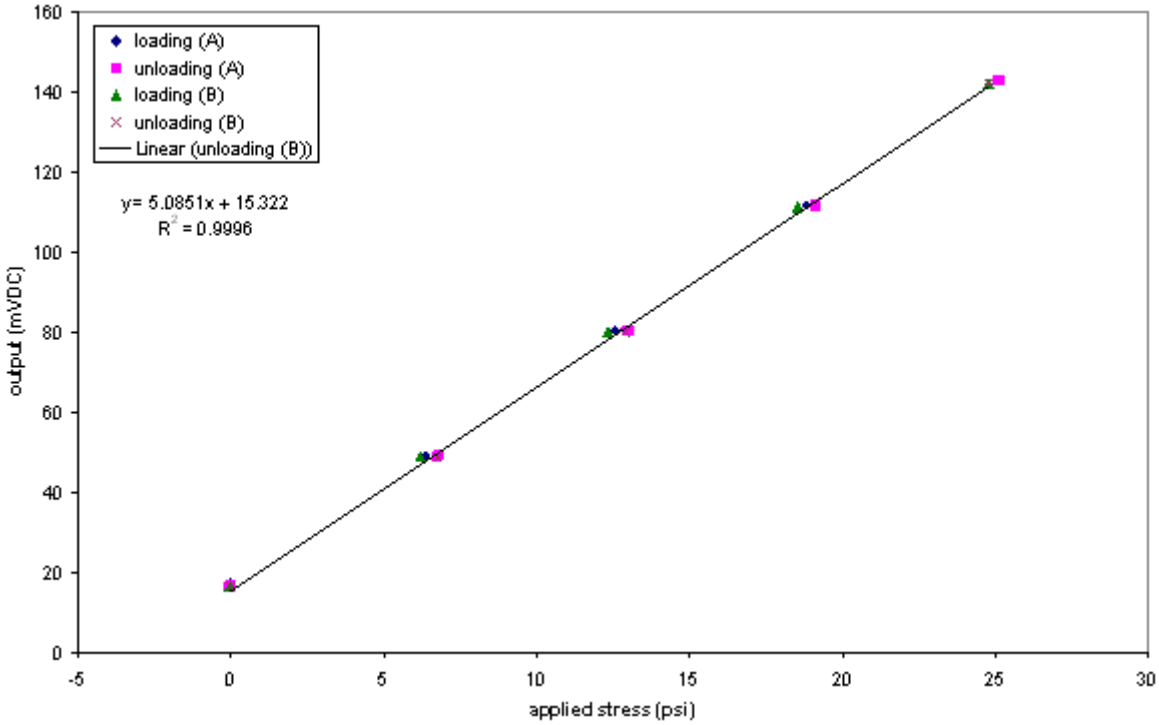

Figure B.19. Soil Calibration 1 for EPC 10055.

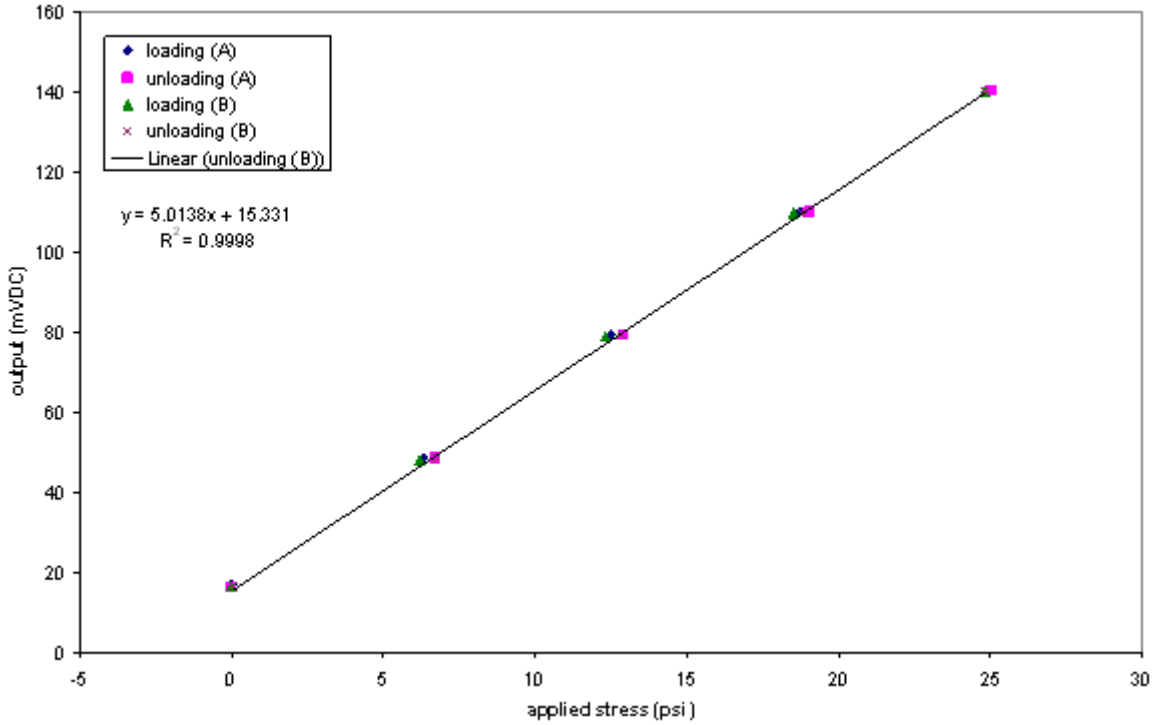

Figure B.20. Soil Calibration 2 for EPC 10055.

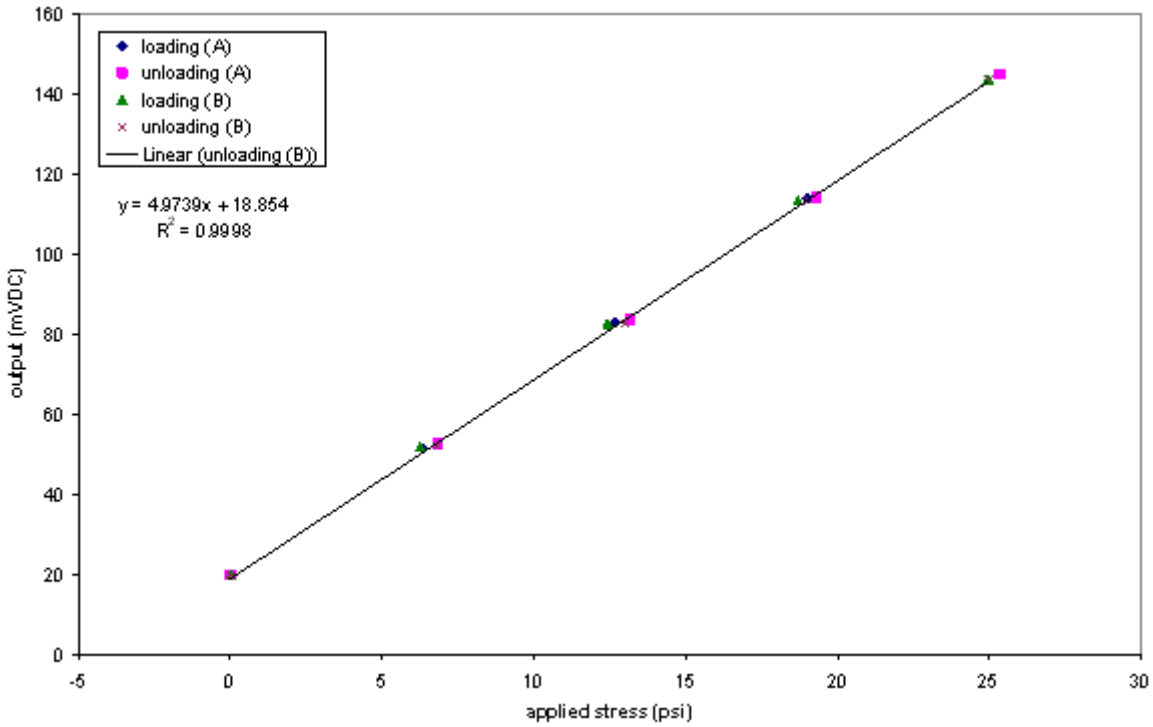

Figure B.21. Soil Calibration 1 for EPC 10056.

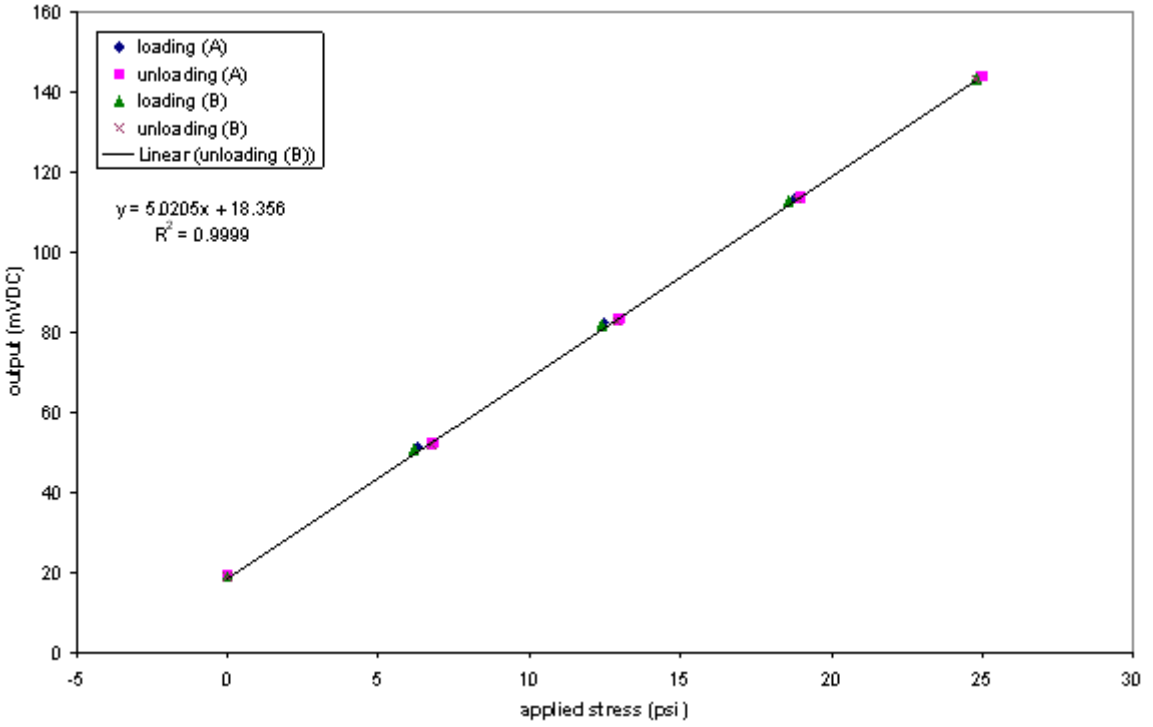

Figure B.22. Soil Calibration 2 for EPC 10056.

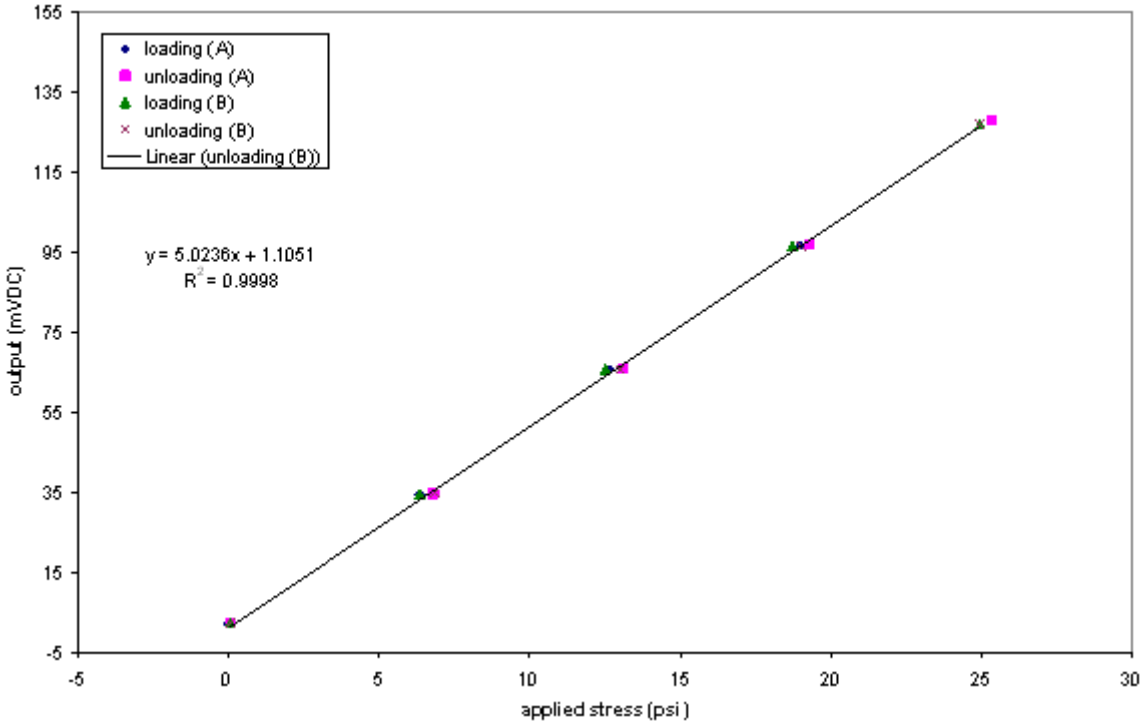

Figure B.23. Soil Calibration 1 for EPC 10057.

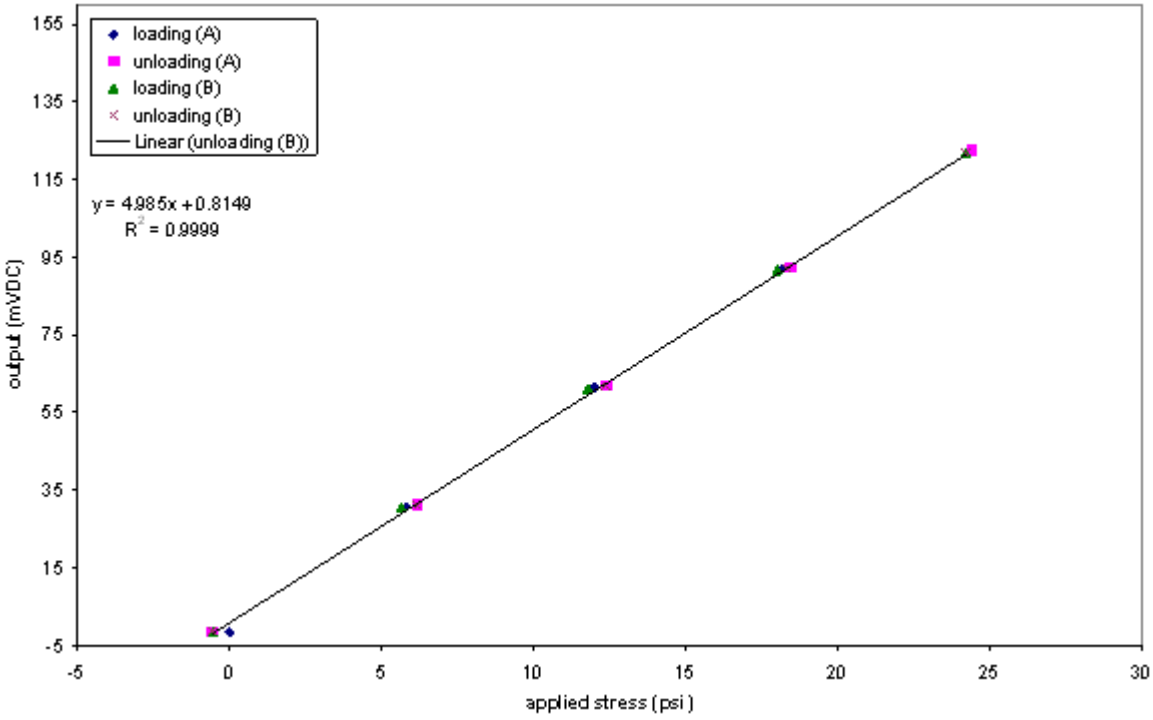

Figure B.24. Soil Calibration 2 for EPC 10057.

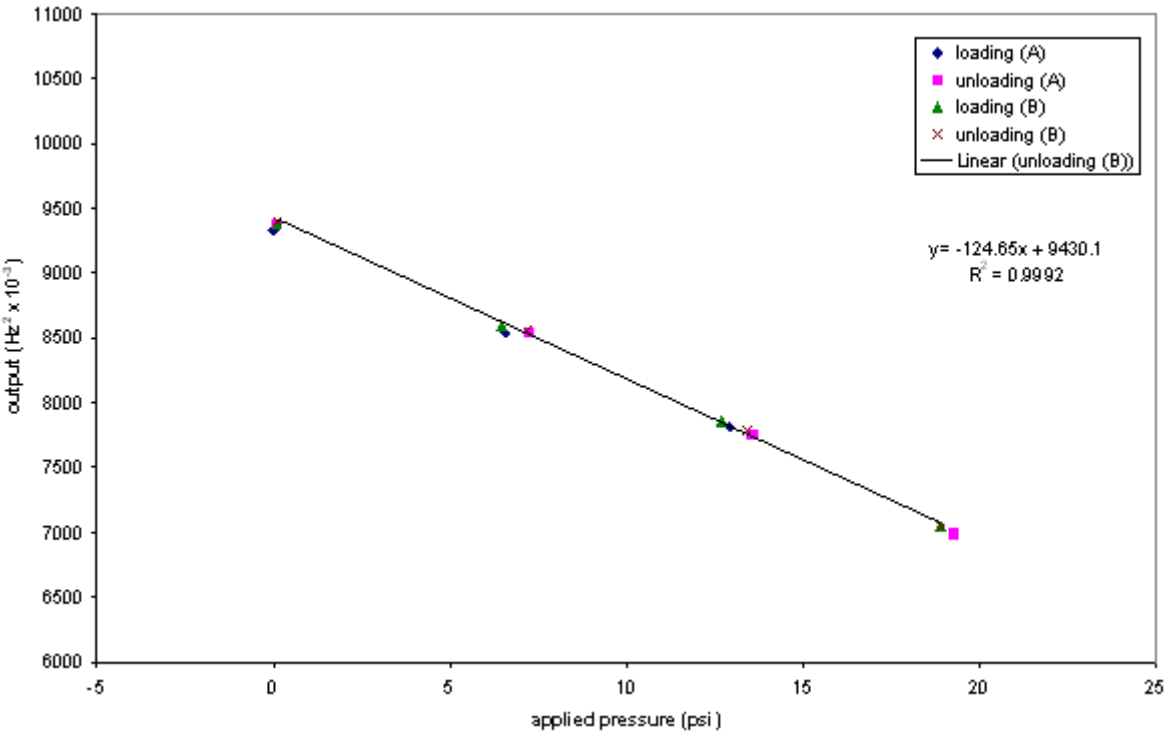

Figure B.25. Fluid Calibration for EPC 4203.

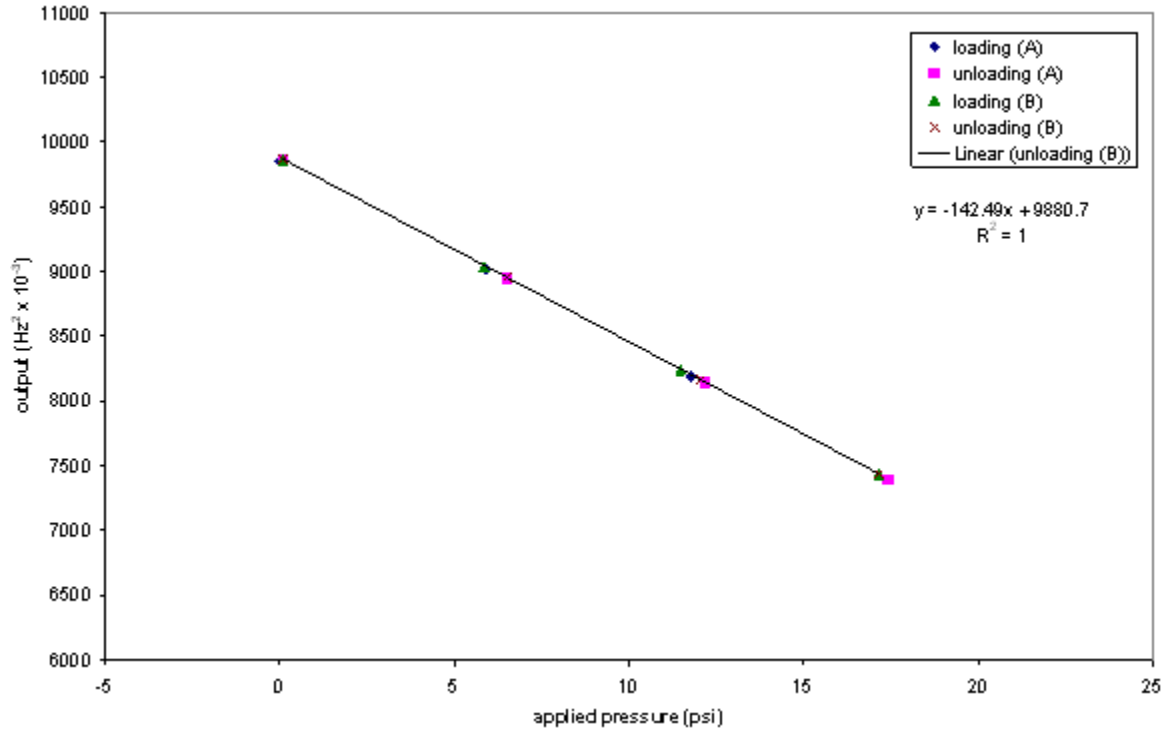

Figure B.26. Fluid Calibration for EPC 4204.

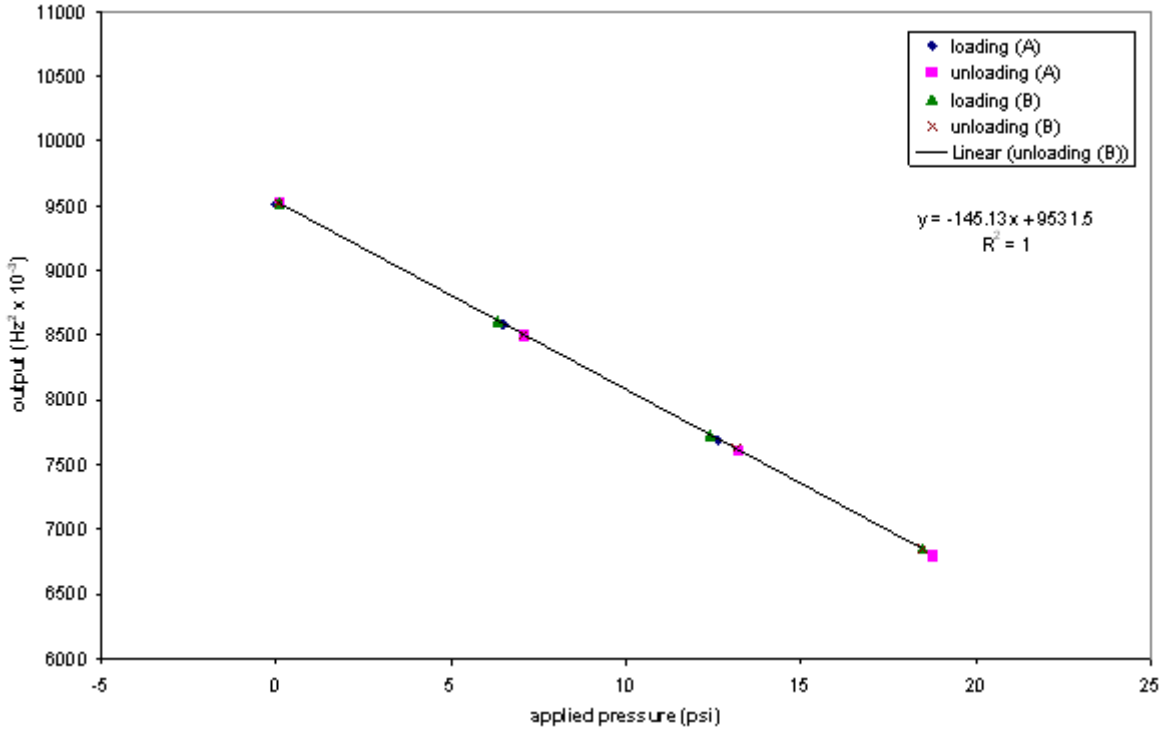

Figure B.27. Fluid Calibration for EPC 4206.

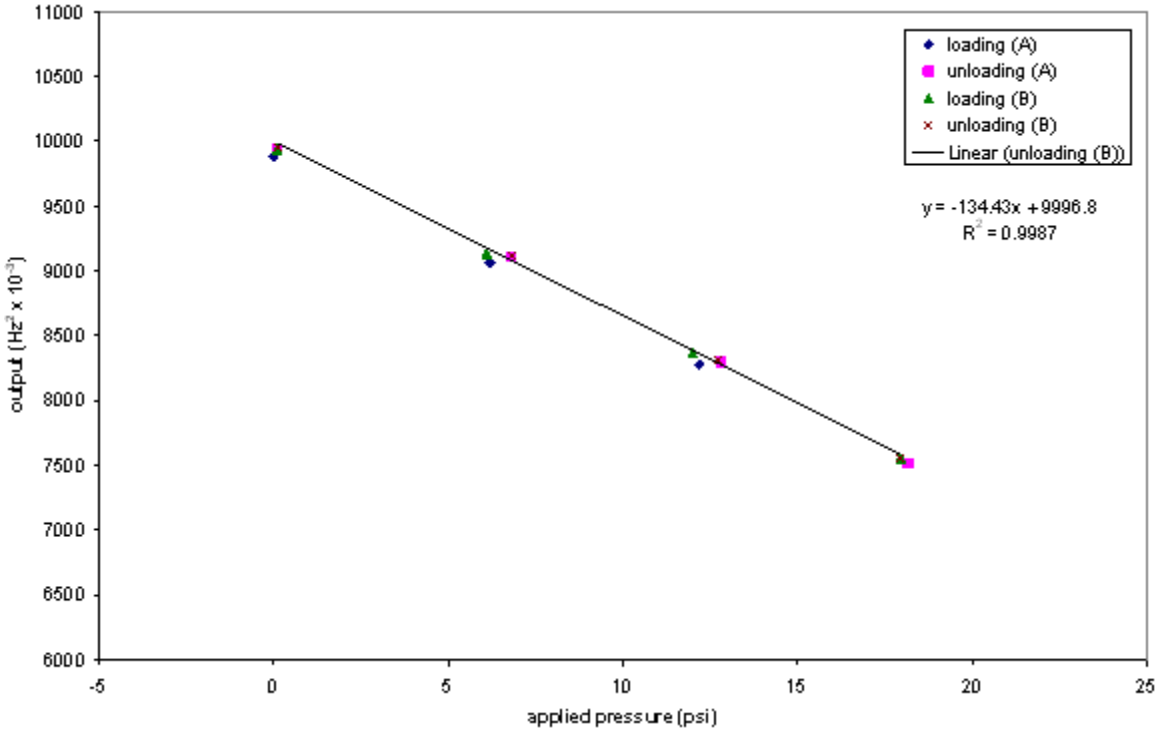

Figure B.28. Fluid Calibration for EPC 4208.

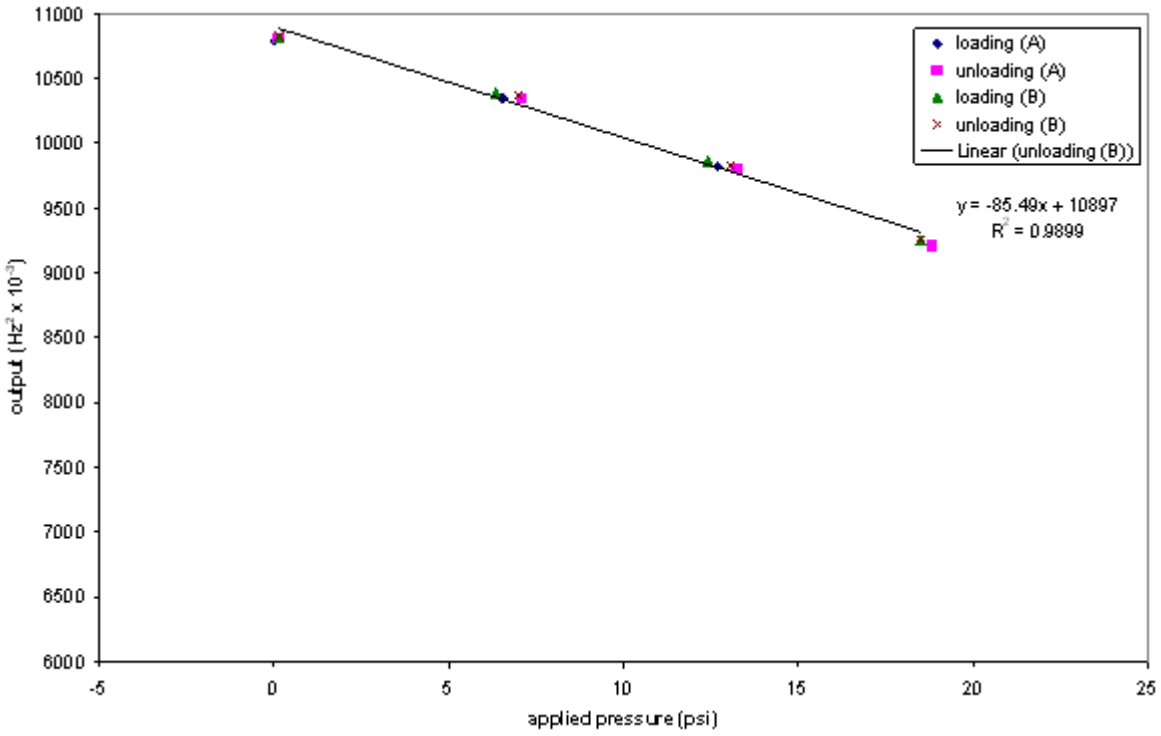

Figure B.29. Fluid Calibration for EPC 4209.

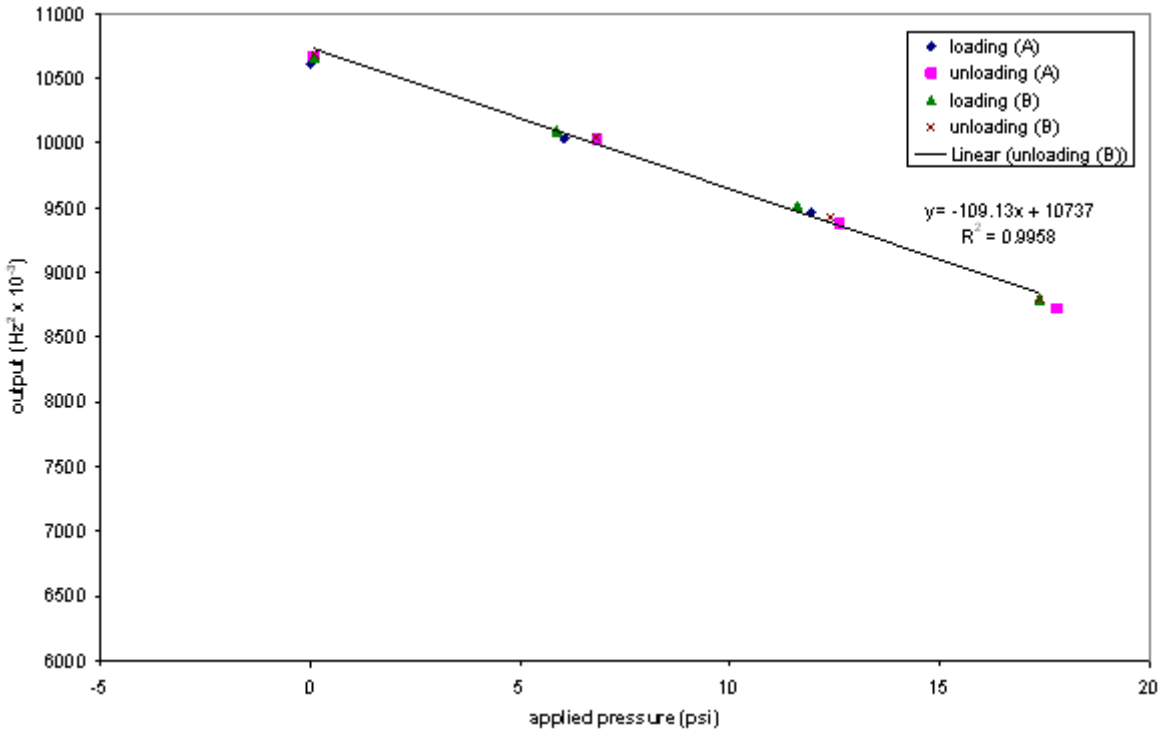

Figure B.30. Fluid Calibration for EPC 4210.

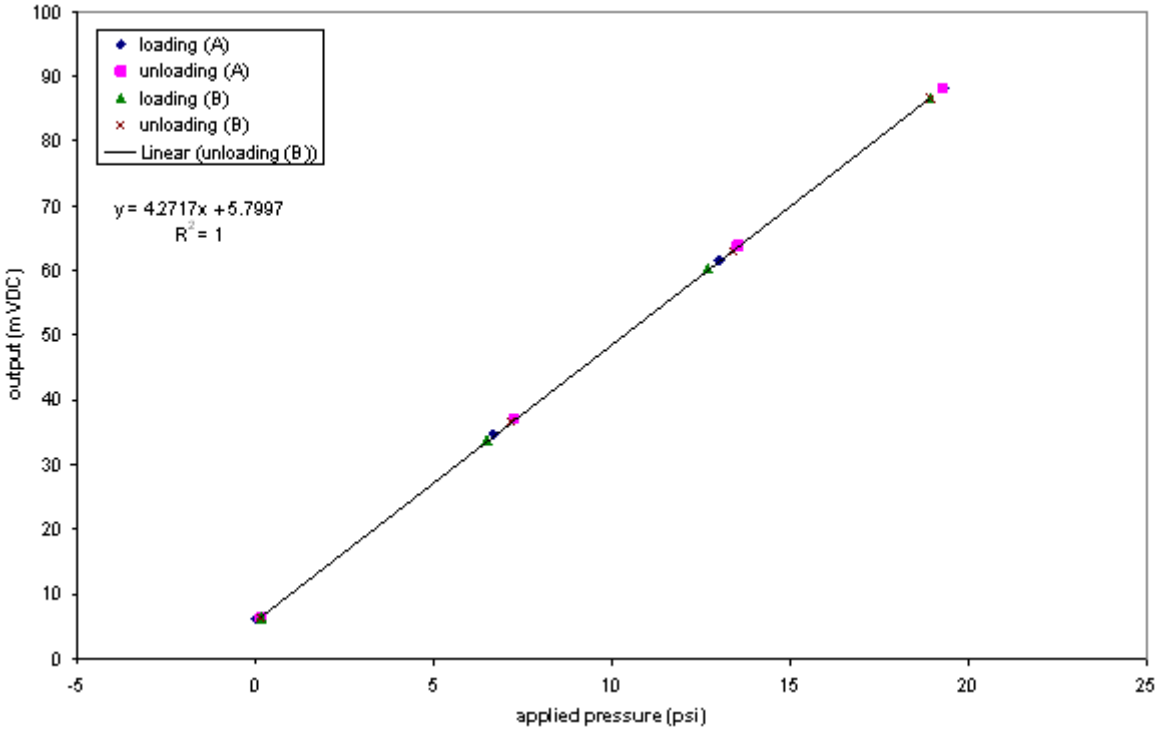

Figure B.31. Fluid Calibration for EPC 10052.

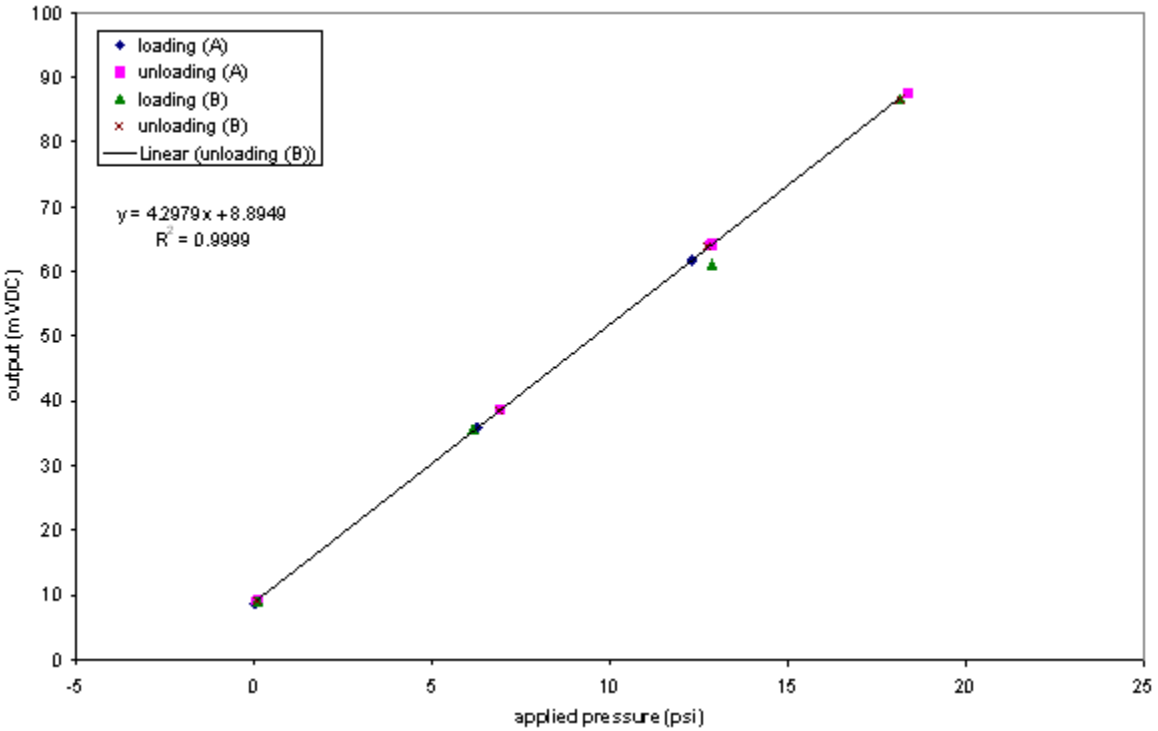

Figure B.32. Fluid Calibration for EPC 10053.

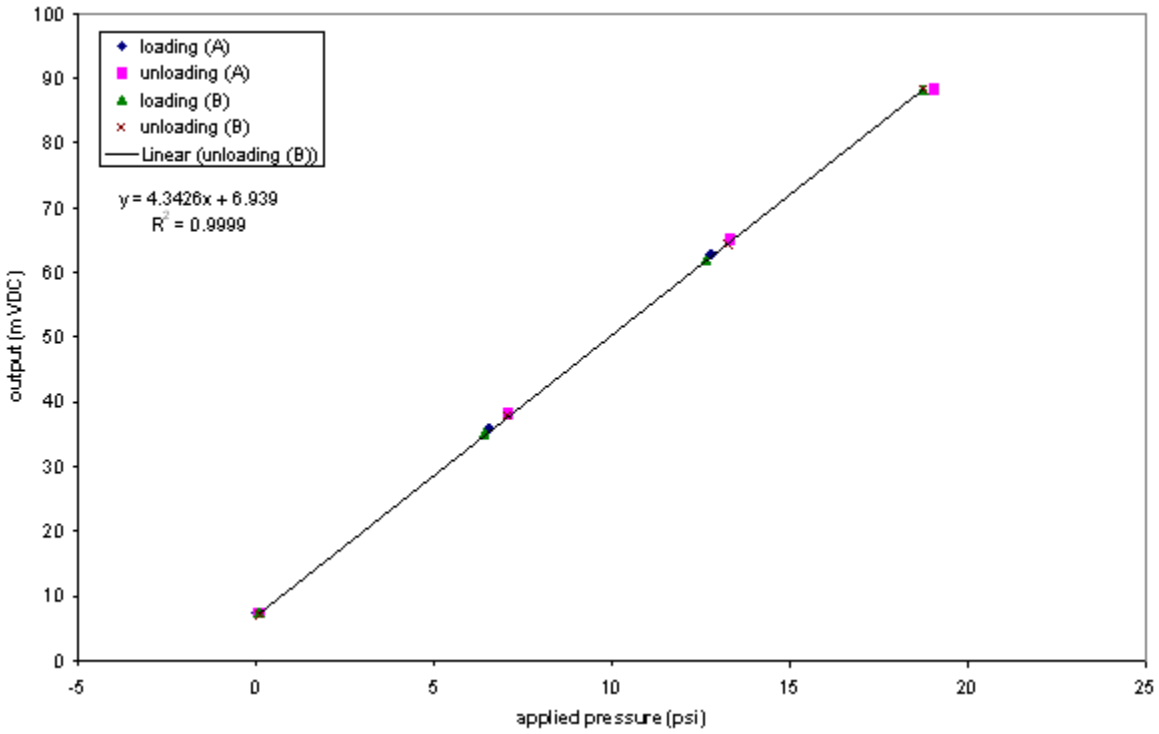

Figure B.33. Fluid Calibration for EPC 10054.

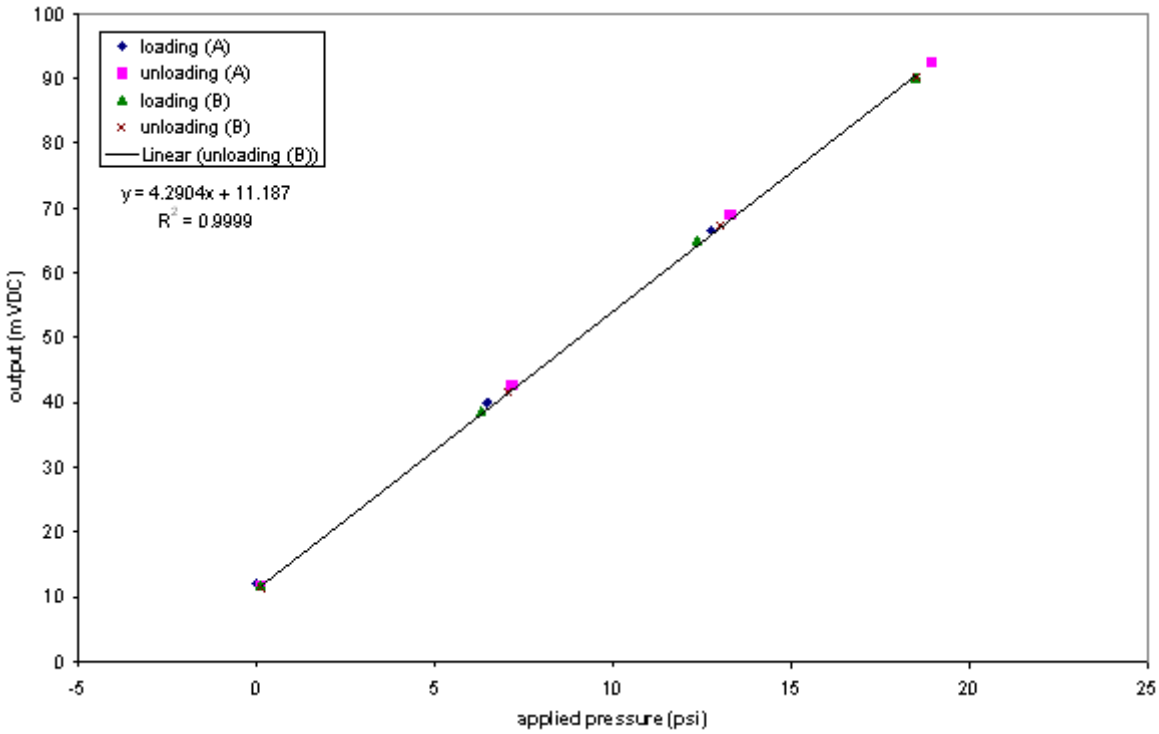

Figure B.34. Fluid Calibration for EPC 10055.

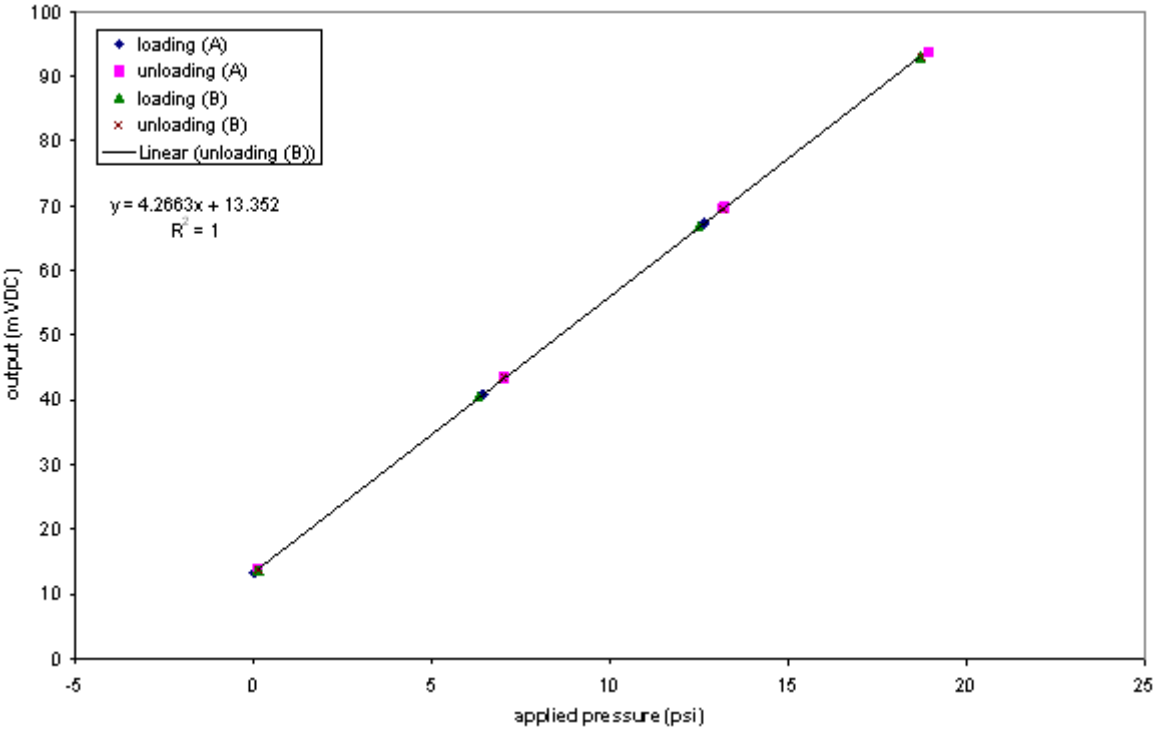

Figure B.35. Fluid Calibration for EPC 10056.

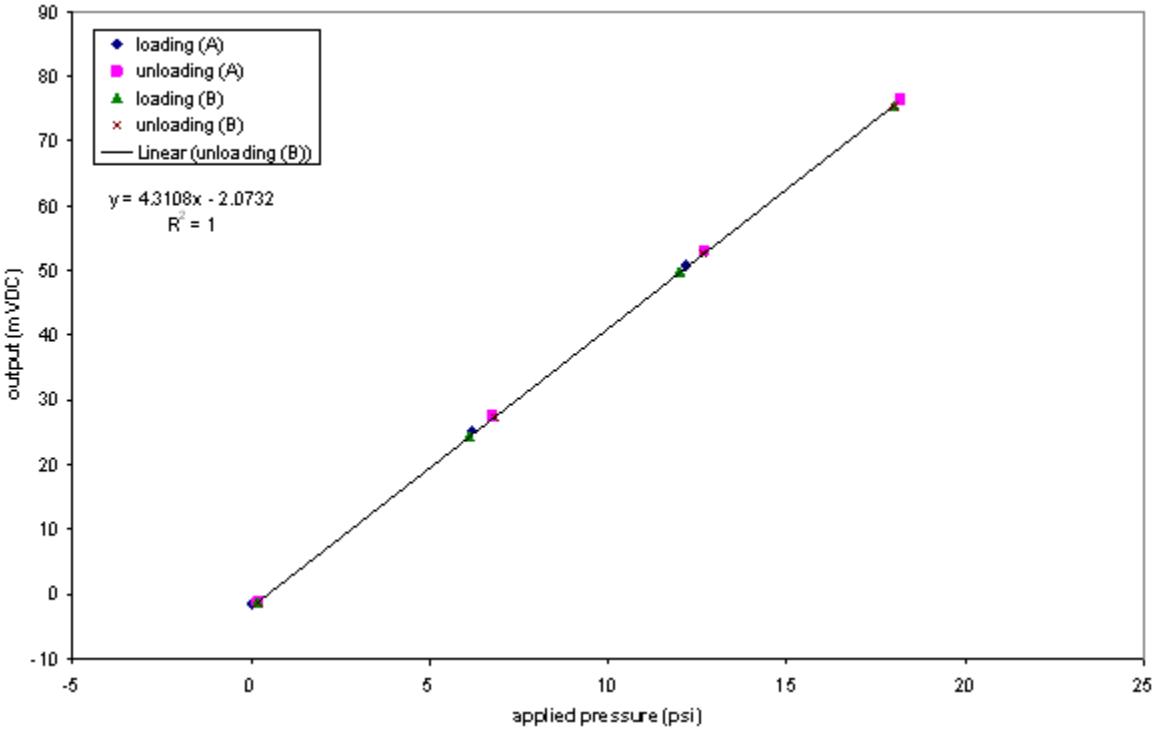

Figure B.36. Fluid Calibration for EPC 10057.

Appendix C

Temperature Corrections of EPC readings

Initial readings taken in the winter of 2006-07 indicated that the all EPC readings at the base of the platform were decreasing steadily, amounting to several psi over several months. This was surprising, as there had been no activity at the site since the end of construction in October. However, it was noted after retrieving data from the spring, that the readings reached a plateau and began to increase again. A plot superimposing the temperature of one sensor on the secondary y-axis suggested a strong correlation between the sensor temperature and the EPC readings. Temperature effects on the pressure transducers themselves were confined to the vibrating wire sensors only, and could be accounted for with correction factors provided by the manufacturer. Those effects, however, were calculated to be minimal, and did not account for the variation observed in the readings. Furthermore, the temperature effects were seen on all sensors, not just the vibrating wire EPCs. It was assumed that there was an additional temperature effect related to the EPC construction, possibly involving differential expansion/contraction of the materials involved (soil, steel, and hydraulic fluid).

In any case, an effort was made to minimize the influence of temperature by introducing a temperature correction factor to the earth pressure calculation. A factor was chosen by trial and error that would eliminate the dip in readings due to temperature effects the readings in the time period in which the temperature effect was most visible. Because temperatures were found to be fairly uniform among the sensors, a single temperature reading was used for determining all correction factors. The resulting plots are shown below. Figures C.1, C.3, C.5, and C.7 show the original readings with temperature from one sensor plotted on a secondary y-axis. Figures C.2, C.4, C.6, and C.8 show the measurements after the correction, and are the same plots used in Chapter 4.

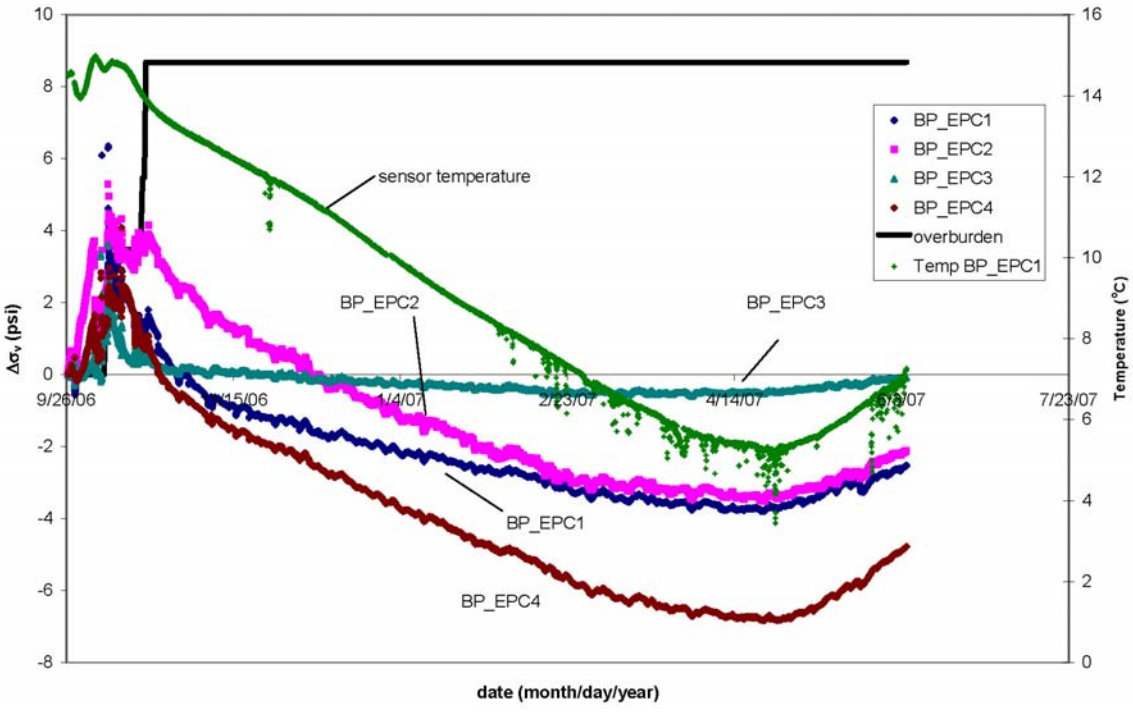

Figure C.1. Original data for BP_EPC1- BP_EPC4.

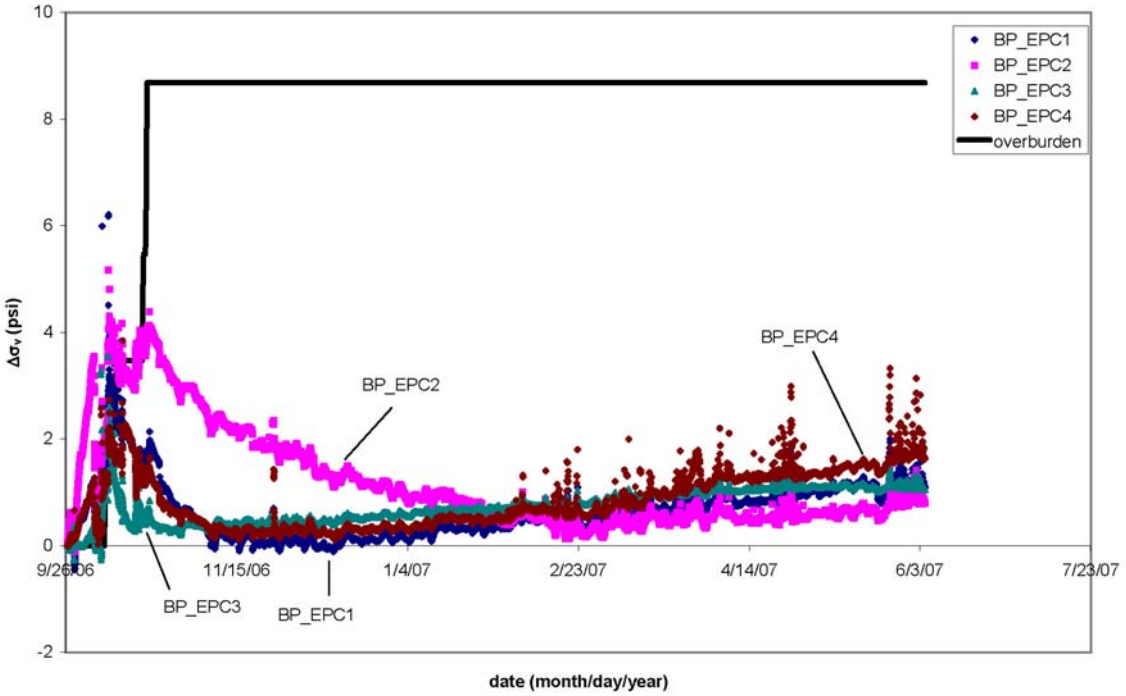

Figure C.2. Data for BP_EPC1- BP_EPC4 following the temperature correction.

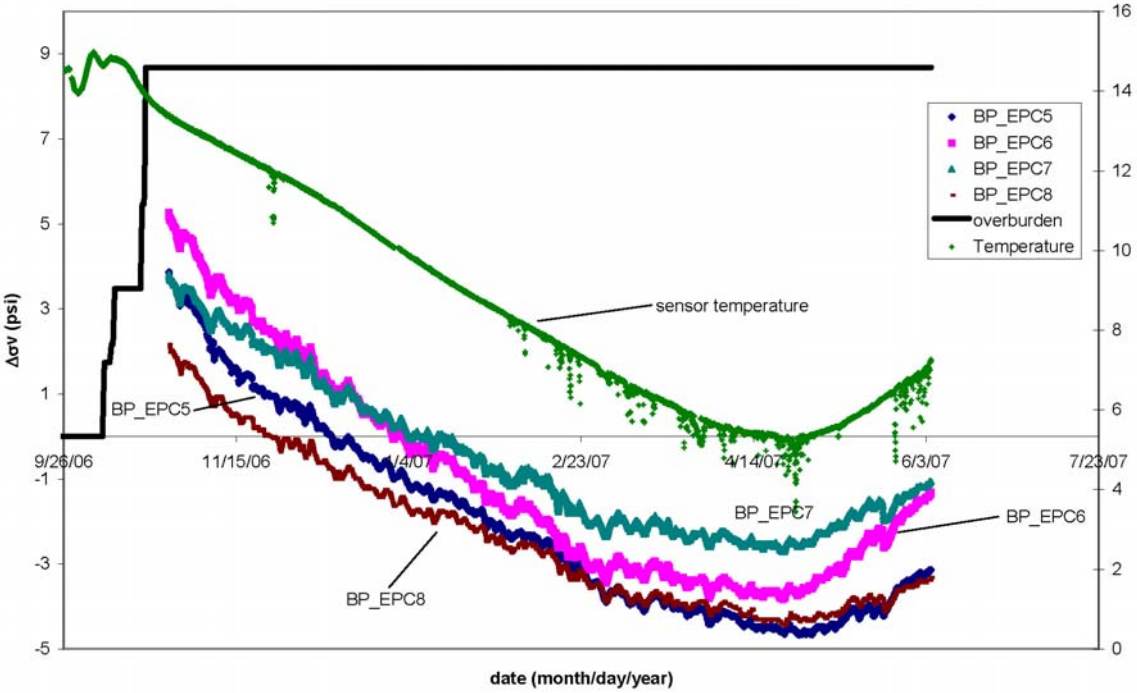

Figure C.3. Original data for BP_EPC5- BP_EPC8.

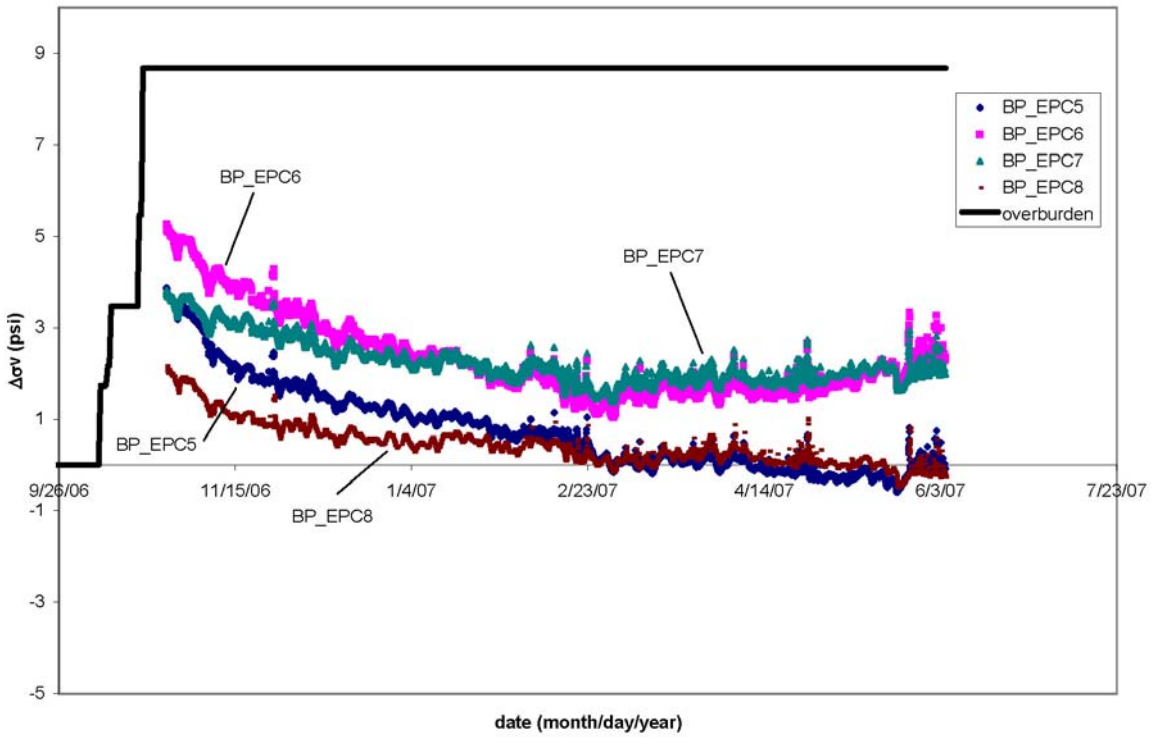

Figure C.4. Data for BP_EPC5- BP_EPC8 following the temperature correction.

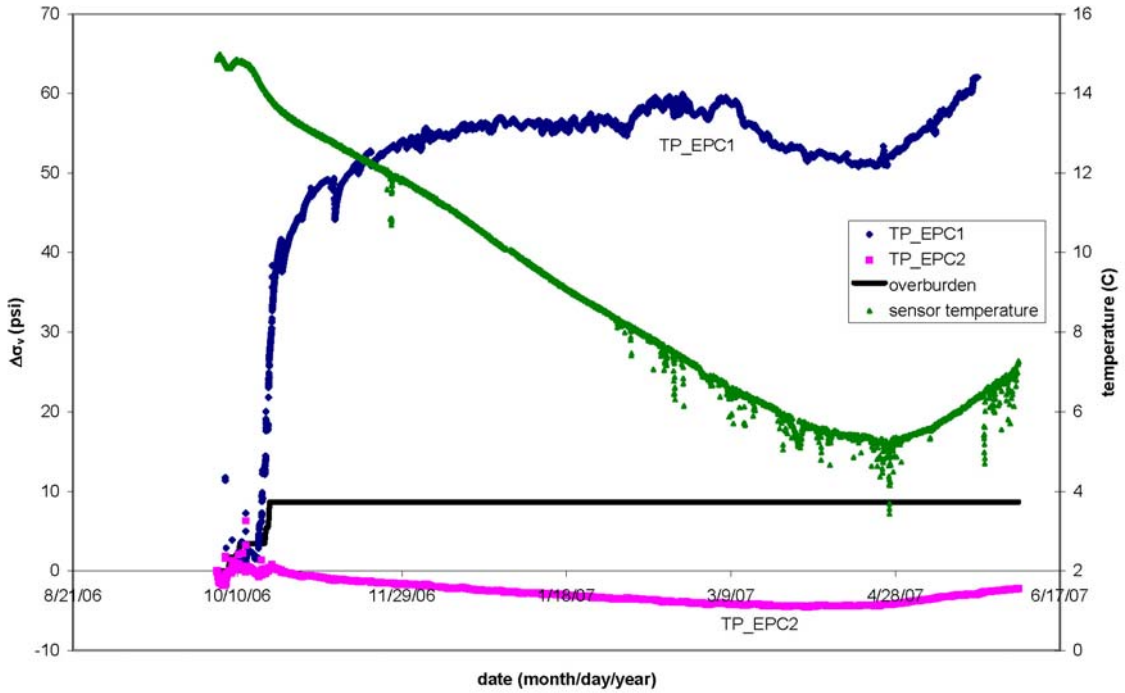

Figure C.5. Original data for TP_EPC1- TP_EPC2.

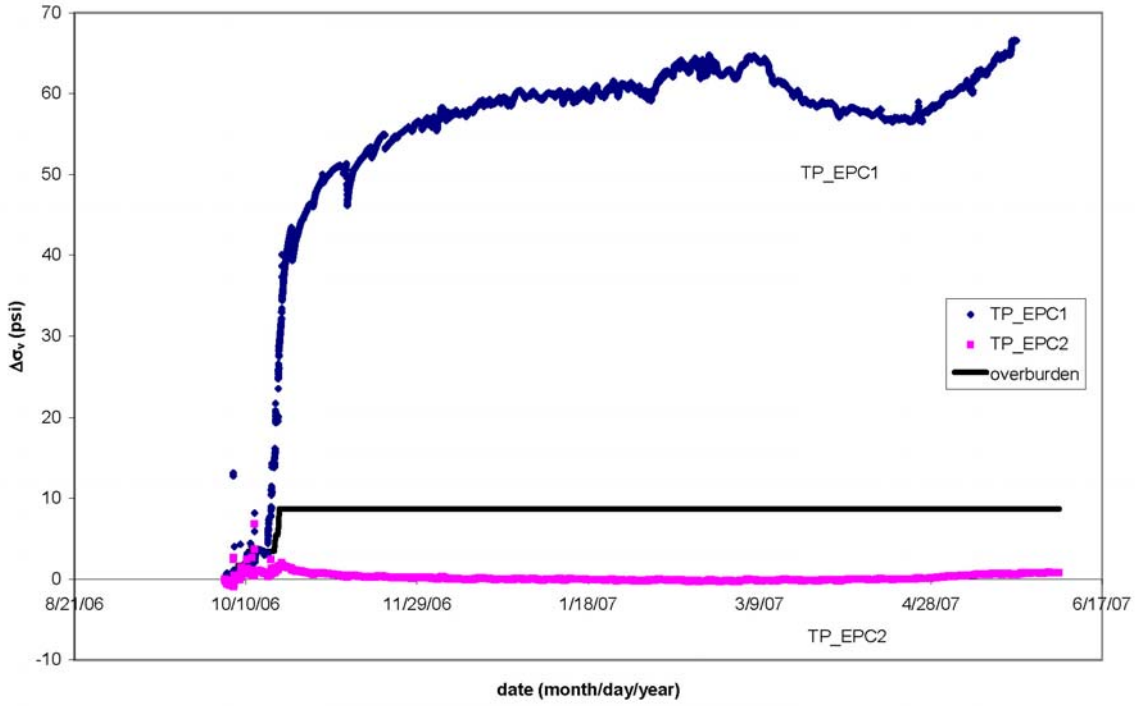

Figure C.6. Data for TP_EPC1- TP_EPC2 following the temperature correction.

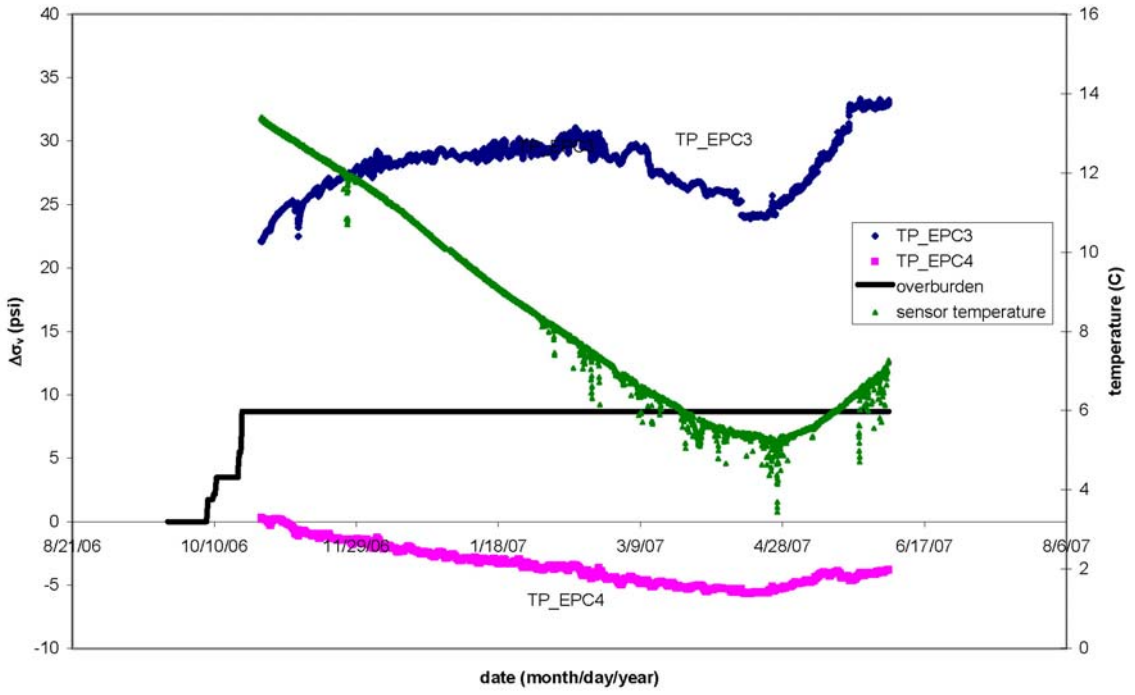

Figure C.7. Original data for TP_EPC3- TP_EPC4.

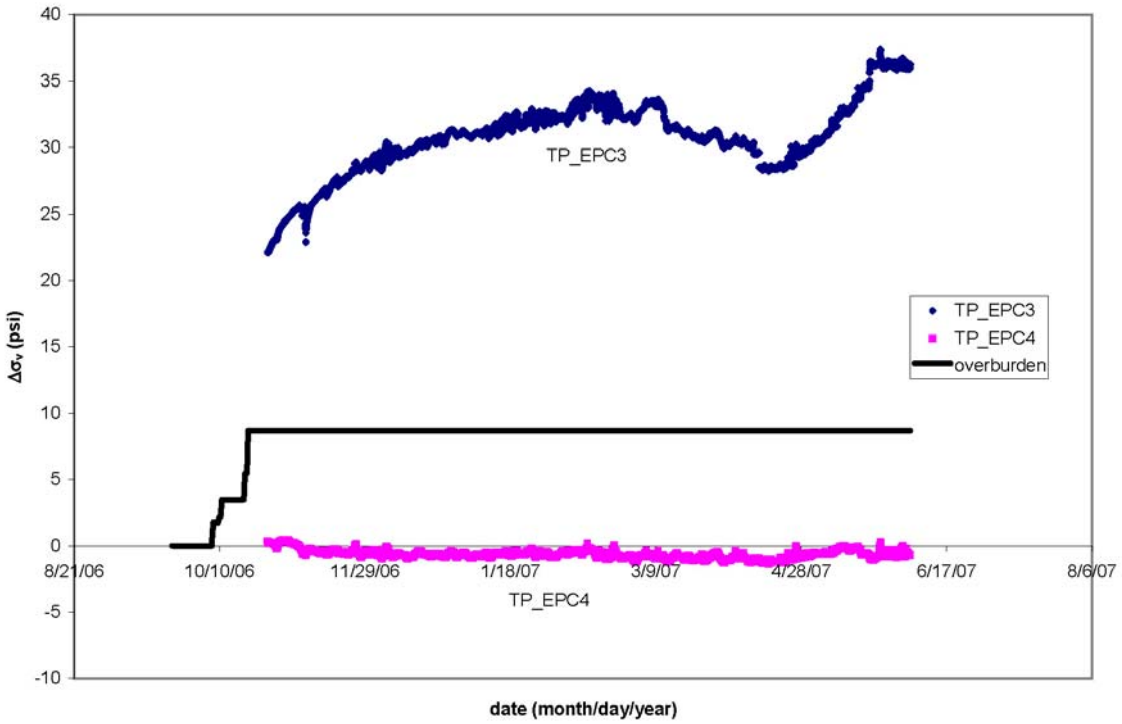

Figure C.8. Data for TP_EPC3- TP_EPC4 following the temperature correction.

Appendix D

Axial pile load calculation

The axial load on a steel pipe pile filled with concrete can be calculated given the necessary strain measurements. The system is simplified as follows. The embankment load is applied to the steel pile cap, which is considered a rigid plate. Displacement boundary conditions apply at the interface between the pile cap and the steel/concrete. Transverse stresses in the steel pipe and the concrete fill are represented as *p*.

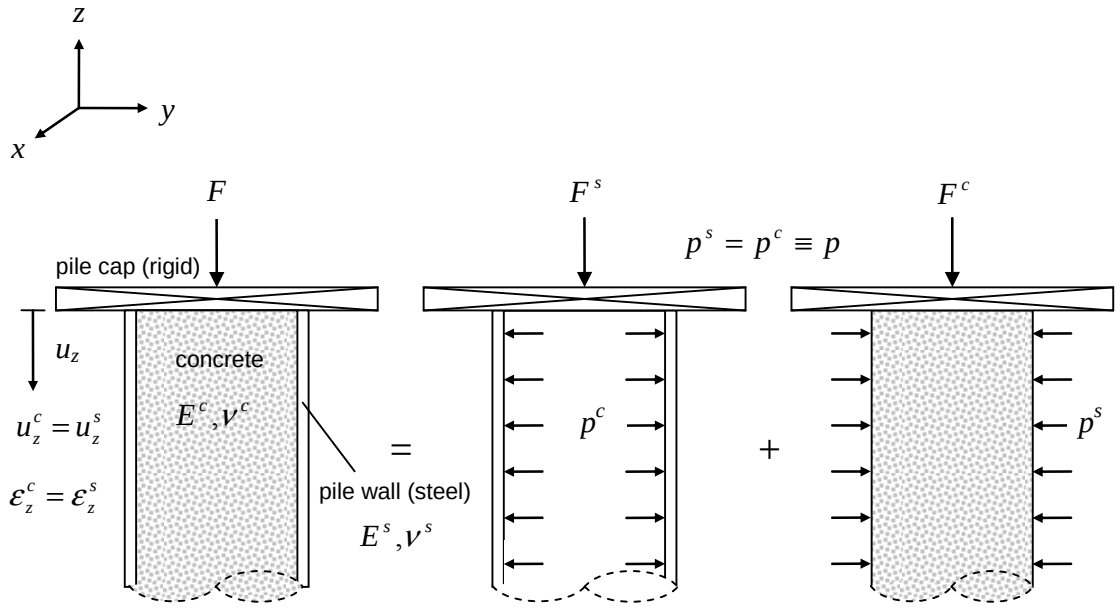

Figure D.1. Schematic showing assumptions used for calculation of axial force in the pile.

Generalized Hooke's Law in a Cartesian coordinate system can be expressed as follows:

$$\varepsilon_x = \frac{1}{E}\left[\sigma_x - \nu\left(\sigma_y + \sigma_z\right)\right] \tag{D.1}$$

$$\varepsilon_y = \frac{1}{E}\left[\sigma_y - \nu\left(\sigma_x + \sigma_z\right)\right] \tag{D.2}$$

$$\varepsilon_z = \frac{1}{E}\left[\sigma_z - \nu\left(\sigma_x + \sigma_y\right)\right] \tag{D.3}$$

For axial loading of the prismatic pipe pile, stresses in the transverse direction are independent of the orientation within the transverse plane, such that

$$\sigma_x = \sigma_y = p \tag{D.3}$$

$$\varepsilon_x = \varepsilon_y \equiv \varepsilon_t \tag{D.4}$$

reducing Eqs. D.1-D.3 to

$$\varepsilon_a = \varepsilon_z = \frac{1}{E}\left(\sigma_z - 2\nu p\right) \tag{D.5}$$

$$\varepsilon_t = \frac{1}{E}\left[(1-\nu)p - \nu\sigma_z\right] \tag{D.6}$$

Considering Eqs. D.5 and D.6 for both the steel and concrete components, this would yield four equations with four unknown stresses. However, as shown in Fig. D.1, transverse stresses in the steel and concrete are equal and the equation for ε_p^s is eliminated, resulting in three equations for three unknowns:

$$\varepsilon_a^s = \frac{1}{E^s}\left(\sigma_z^s - 2\nu^s p\right) \tag{D.7}$$

$$\varepsilon_a^c = \frac{1}{E^c}\left(\sigma_z^c - 2\nu^c p\right) \tag{D.8}$$

$$\varepsilon_t^c = \frac{1}{E^c}\left[\left(1-\nu^c\right)p - \nu^c \sigma_z^c\right] \tag{D.9}$$

Additionally, for the assumed displacement boundary conditions shown in Fig D.1, axial strains in the concrete and steel would be equal ($\varepsilon_z^c = \varepsilon_z^s$). Thus, only two measurements, ε_t^c and either ε_a^c or ε_a^s, are required to calculate unknown stresses σ_z^s, σ_z^c and p. If p is considered to be negligible ($2\nu p << \sigma_z$), only the axial strain in the steel or concrete must be measured in order to calculate σ_z^s and σ_z^c:

$$\varepsilon_z^s = \frac{\sigma_z^s}{E^s} \tag{D.10}$$

$$\varepsilon_z^c = \frac{\sigma_z^c}{E^c} \tag{D.11}$$

In either case, once σ_z^s and σ_z^c are calculated, values for axial stress is multiplied by the respective cross-sectional area and summed in order to obtain the total axial load:

$$\begin{aligned} F^{tot} &= F^s + F^c \\ &= \sigma_z^s A^s + \sigma_z^c A^c \end{aligned} \tag{D.12}$$

Unfortunately, measurements of the transverse strain ε_p^c were not obtained, so for the pile load calculations it was necessary to assume that *p* was negligible; loading was essentially uniaxial. Looking at Eqs. D.7 and D.8 noting *p* is compressive, this should result in an underestimate of the pile load.

Calculation of the pile load depends on how the axial strain measurements are used. On the one hand, in order to obey the displacement boundary conditions shown in Fig D.1, only one value for axial strain in both materials is needed. On the other hand, measurements and observed field conditions suggest that different boundary conditions may exist in the structure.

Four different scenarios for pile calculation are discussed in this section. Quantities such as dimensions, strain measurements and elastic constants used in the calculations are shown in Table D.1. Pile load calculations are shown in Table D.2, and were based on the most recent

strain measurements from the functional gages. For pile 1, the value of ε_z^s used in the calculation was an average of readings from both gages (P1W and P1E). Since measurements of σ_z^c were not available for pile 1, readings from pile 2 were used, with the assumption that the piles were subject to identical loading conditions.

Table D.1. Quantities used to calculate pile loads.

measurements		**English Units**	**Metric Units**
radius of steel	r^s	0.5 [ft]	1.52E-01 [m]
thickness of steel	t^s	0.0208 [ft]	6.35E-03 [m]
axial strain in concrete (P2C)	ε^c	242 [με]	
axial strain on steel (P1W)	$\varepsilon^{s,w}$	538 [με]	
axial strain on steel (P1E)	$\varepsilon^{s,e}$	330 [με]	
axial strain on steel (P2E)	$\varepsilon^{s,e}$	460 [με]	
ave. axial strain on steel (P1)	$\varepsilon^{s,ave}$	434 [με]	
assumed constants			
elastic modulus of steel	E^s	2.90E+07 [psi]	200 [Gpa]
elastic modulus of concrete	E^c	1.45E+06 [psi]	10 [Gpa]
calculations			
area of steel	A^s	0.0641 [ft^2]	5.95E-03 [m^2]
area of concrete	A^c	0.721 [ft^2]	6.70E-02 [m^2]

Table D.2. Pile loads for various strain "scenarios."

		Pile 1†		**Pile 2**	
scenario	**description**	**kips**	**kN**	**kips**	**kN**
1	assume $\varepsilon^s = \varepsilon^c$, use ε^s	185	823	192	854
2	assume $\varepsilon^s = \varepsilon^c$, use ε^c	101	449	101	449
3	use ε^s and ε^c "as measured"	153	681	160	712
4	assume $\varepsilon^c = 0$, use ε^s only	116	516	123	547

† Used ε^c from Pile 2, where applicable

Given the displacement boundary condition ($\varepsilon_z^c = \varepsilon_z^s$), the axial strain in both materials should be identical. Field measurements, however, do not support this condition, assuming ε_z^c from P2C is reliable. In order to calculate the load while obeying the boundary conditions, then, one of either ε_z^s and ε_z^c should be used. Of the two, ε_z^s is considered to be the more reliable, as multiple measurements were taken. The pile load calculation using this assumption is referred to as "scenario 1" in Table D.2. The same calculation can be made assuming that ε_z^c is the uniform axial strain, and is referred to as "scenario 2".

One possible explanation for the discrepancy between measurements of ε_z^s and ε_z^c is that there is either poor contact or no contact at all between the concrete and the pile cap, as illustrated in Fig. D.2. It was indeed observed in the field that pipes were not necessarily filled to the top with concrete, and even when they were completely filled, air bubbles rising from within the pipe tended to lower the concrete level after pouring. In this scenario, the entire load is transferred to the pipe at the top of the pile. Some of the load is gradually transferred to the concrete via shear resistance due to adhesion between the concrete and the pile wall. Though it is likely in this case that strain is non-uniform in the concrete near the top of the pile, an assumption could be made that the measurement of ε_z^c represents an average strain in the concrete. In this case, individual values of ε_z^s and ε_z^c could be used in Eq. D.12 as indicated by strain measurements. This is pile load calculation scenario 3.

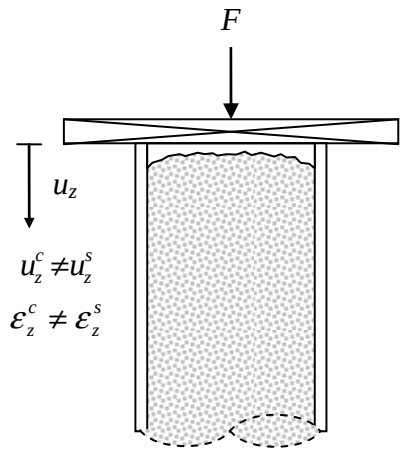

Figure D.2. Schematic showing how displacement boundary condition at the top of the pile as defined in Fig. D.1 may not apply if contact between the concrete and the pile cap is poor or nonexistent.

Finally, one could assume that close to the top of the pile the contribution of the concrete to the total load is negligible. This may be the case if shear resistance due to adhesion is insufficient to sustain shear stresses that develop along the pile wall–concrete interface. This is "scenario 4" in Table D.2, and this is used as the representative response of the system. Thus, the average load on the pile was 119.5 kips (531.5 kN).